
UNIVERSITY OF BIRMINGHAM

PhD Thesis

# Development and Characterisation of Novel Coatings and Thin Films for High-Efficiency Smart Thermoelectric Materials and Modules

By

**Mikdat GURTARAN**

Student ID: [redacted]

Supervisor: Professor Hanshan Dong

Co-Supervisor: Dr Xiaoying Li

School of Metallurgy and Materials

University of Birmingham

July 2024

# Synopsis

This PhD study was focused on improving the heat-to-energy conversion efficiency at high and low temperatures in thermoelectric materials and modules by developing advanced coatings and thin films. Firstly, the oxidation behaviour and mechanism of P-type (Zr,Ti)Co(Sn,Sb) and N-type (Zr,Ti)Ni(Sn,Sb) half-Heusler thermoelectric (TE) materials (used in this PhD project) at medium-to-high-temperatures were examined using scanning electron microscopy (SEM), energy dispersive spectrometry (EDX), and X-ray diffraction (XRD). It was observed that the surface morphology and composition of these TE materials completely changed after cyclic oxidation at 500°C. Multilayer structures of $SnO_2$+$Ni_3Sn_4$+$(Zr,Ti)O_2$ and CoSb+$SnO_2$+$Sb_2O_4$+$(Zr,Ti)O_2$ formed on the surface of the N-type and P-type TE materials, respectively. Additionally, thick double-layers formed on the surface of N-type and P-type TE materials ($SnO_2$+$Ni_3Sn_4$ and $SnO_2$+CoSb, respectively) when statically oxidised at 600°C for 50h. Based on the findings obtained, advanced oxidation-resistant CrSi coatings were developed and deposited on these TE materials using the magnetron sputtering physical vapour deposition (PVD) technique. The CrSi coatings can effectively reduce oxidation kinetics, protecting both N-type ((Zr,Ti)Ni(Sn,Sb)) and P-type ((Zr,Ti)Co(Sn,Sb)) TE materials against oxidation at 500°C and 600°C, regardless of the oxidation methods (static or cyclic).

To increase the efficiency of thermoelectric materials and modules, the interface of P-type half-Heusler TE materials ((Zr,Ti)Co(Sn,Sb)) was metallised by Ni/NiGO coatings with high electrical and thermal conductivities. These coatings were deposited using the electro-brush plating method, which is more flexible and cost-effective than other coatings methods. The findings showed that metallising Ni/NiGO coatings significantly reduced the interfacial and sheet resistances of P-type TE material although no significant effect of graphene oxide (GO) addition on increasing the electrical conductivity of the coating layer. Additionally, Ni coatings protected the material from oxidation at high temperatures.

To improve the TE performance of Bismuth Telluride (BiTe-based) TE materials, which are practically used in low-temperature applications, BiTe-based thin films were produced on different substrates using the magnetron sputtering PVD system. The outcome of the study has indicated that the power output of thin films deposited on different substrates (glass, Kapton, and silicon) is closely related to how the active layers are connected. However, the proportional increase in thermal conductivity along with electrical conductivity with increasing temperature limited the further improvement of the figure of merit (zT) value.

# Acknowledgements

I would like to express my greatest gratitude to my valuable supervisors, Prof Hanshan Dong and Dr Xiaoying Li, who supported, trained and guided me in every aspect throughout this PhD study. I am grateful for everything I learned from them. I am also thankful to Dr. Zhenxue Zhang, who assisted in both experimental studies and article preparation. I would like to send a huge thank to Dr. Behnam Dashtbozorg, who always helps me with my laboratory work. Additionally, I would like to send my love and respect to every member of the Surface Engineering group in which I enjoy being a part. I also would like to thank the staff at the University of Birmingham for their assistance with the experiments.

I would like to thank MATRES Scrl (Italy) for their efforts in providing thermoelectric materials.

I am grateful to my sponsor, the Ministry of National Education of the Republic of Turkey, for their financial support throughout my PhD study. Additionally, I would like to thank the European H2020 (Grant No: 862289) for financial support for this PhD project.

I would like to express my gratitude to my precious parents and brother, who have always supported me throughout my education life.

Finally, I would like to offer special thanks to my love, Fatma Merve Gurtaran, and my lovely daughter, Neslisah Sultan Gurtaran, for their unwavering support and belief in me.

# Scientific Contribution

**Journals:**

1- Zhang, Z., **Gurtaran, M.,** Li, X., Un, H. I., Qin, Y., Dong, H. (2023). Characterization of magnetron sputtered BiTe-based thermoelectric thin films. Nanomaterials, 13(1), 208.

2- **Gurtaran, M.,** Zhang, Z., Li, X., Dong, H. (2024). Cyclic oxidation behaviour of N-type (Zr, Ti) Ni (Sn, Sb) and P-type (Zr, Ti) Co (Sn, Sb) thermoelectric materials. Journal of Materials Research and Technology, 30, 7476-7484.

3- **Gurtaran, M.,** Zhang, Z., Li, X., Dong, H. (2024). Developing Advanced CrSi Coatings for Combatting Surface Degradation of N-type (Zr, Ti) Ni (Sn, Sb) and P-type (Zr, Ti) Co (Sn, Sb) half-Heusler thermoelectric materials. Journal of Materials Research and Technology.

**Related Publications:**

1- **Gurtaran, M.,** Zhang, Z., Li, X., Dong, H. (2023). High-Temperature Oxidation Behaviour of CrSi Coatings on 316 Austenitic Stainless Steel. Materials, 16(9), 3533.

2- Zhang, Z., **Gurtaran, M.,** Dong, H. (2024). Low-Cost Magnesium-Based Thermoelectric Materials: Progress, Challenges, and Enhancements. ACS Applied Energy Materials.

**Conferences:**

1- Zhang, Z., **Gurtaran, M.,** Li, X., Dong, H. (2022). Oxidation Behaviour of CrSi Coatings Deposited by Magnetron Sputtering Technique, European Oxide Scale Conference, IOM3, UK.

2- Zhang, Z., **Gurtaran, M.,** Li, X., Dong, H. (202). Evaluation of thermoelectric thin film deposited by magnetron sputtering technique, European Oxide Scale Conference, IOM3, UK.

3- Zhang, Z., **Gurtaran, M.,** Li, X., Dong, H. (2023). Degradation of Thermoelectric Materials and their Protection by Chromium Based Coatings, 7th International Conference of Engineering Against Failure, Greece.

4- **Gurtaran, M.,** Zhang, Z., Li, X., Dong, H. (2023). Oxidation Behaviour of CrSi Coatings for Combating Degradation of 316 Stainless Steel at High Temperatures, 7th International Conference of Engineering Against Failure, Greece.

5- **Gurtaran, M.,** Zhang, Z., Li, X., Dong, H. (2023). Advanced Surface Coatings for Oxidation Protection of Thermoelectric Materials, 6th International Conference on Emerging Technologies and Materials Engineering, Romania.

6- **Gurtaran, M.,** Zhang, Z., Li, X., Bianchin, A., Busatto, S., Dong, H. (2024). CrSi Protective Coatings for Thermoelectric Materials against High-Temperature Oxidation, TMS Annual Meeting & Exhibition, USA.

7- Zhang, Z., **Gurtaran, M.,** Li, X., Dong, H. (2024). P-Type $BiSb_2Te_3$ Thin Film Thermoelectric Module Fabricated on a Flexible Substrate Through Magnetron Sputtering, International Conference on Manufacturing Research, UK.

8- **Gurtaran, M.,** Zhang, Z., Li, X., Dong, H. (2024) Developing Advanced CrSi Coatings for Combatting Surface Degradation of n-type (Zr,Ti)Ni(Sn,Sb) and p-type (Zr,Ti)Co(Sn,Sb) Half Heusler Thermoelectric Materials, International Conference on Manufacturing Research, UK.

9- **Gurtaran, M.,** Zhang, Z., Li, X., Dong, H. (Future conference in September 2024). Application and Characterisation of Nickel-Graphene Oxide Nanocomposite Coatings

on Thermoelectric Materials, International Metallurgy and Materials Conference, Turkiye.

10- Zhang, Z., **Gurtaran, M.,** Li, X., Dong, H. (Future conference in September 2024). PVD CrSi Coatings to Protect Thermoelectric Materials from Degradation, International Metallurgy and Materials Conference, Turkiye.

# Contents

# Abbreviations

**A:** Amper

**ALD:** Atomic layer deposition.

**bcc:** Body-cantered cubic.

**BEI:** Backscattered electron image.

**CTE:** Coefficient of thermal expansion.

**CVD:** Chemical vapor deposition.

**DC:** Direct current.

**EDX:** Energy dispersive X-ray spectroscopy.

**FWHM:** Full width at half maximum.

**g:** gram.

**GDOES:** Glow discharge optical emission spectroscopy.

**GO:** Graphene oxide.

**h:** hour.

**HH:** Half-Heusler.

**HV:** Vickers hardness.

**ICR:** Interfacial contact resistance.

**K:** Kelvin.

**κ:** Thermal conductivity.

**kg:** kilogram.

**Kp:** Parabolic rate constant.

**kV:** Kilovolt.

**L:** Litre.

**mL:** Millilitre.

**MBE:** Molecular-beam epitaxy.

**min:** minutes.

**mN:** Millinewton.

**mm:** Millimetre.

**MOCVD:** Metalorganic chemical vapor deposition.

**nm:** Nanometer.

**NiGO:** Graphene oxide-added Nickel.

**Pa:** Pascal.

**PDF:** Powder diffraction file.

**PF:** Power factor.

**Pn:** Pnictogens.

**PVD:** Physical vapor deposition.

**Ra:** Average roughness.

**$R_{electric}$:** Electrical resistance.

**Rq:** Root mean square roughness.

**$R_{thermal}$:** Thermal resistance.

**RF:** Radio frequency.

**s:** Second

**S:** Seebeck.

**SAD:** Selected area diffraction

**SEM:** Scanning electron microscope.

**SiC:** Silicon carbide.

**t:** Time.

**T:** Temperature.

**TE:** Thermoelectric.

**TEM:** Transition electron microscope.

**TED:** Thermoelectric device.

**TPF:** Thermoelectric power factor.

**UK:** United Kingdom.

**V:** Voltage.

**XRD:** X-ray diffraction.

**zT:** Figure of merit.

# List of Figures

# List of Tables

# Chapter 1 Introduction

## 1.1 Research background and driver

The ever-increasing need for energy and the significant decrease in currently used energy sources have raised the demand for renewable energy sources [1, 2]. In addition, the negative effects of fossil-based energy sources on the environment and human health have reached critical levels [3]. For this reason, technologies that are both environmentally friendly and use renewable and sustainable energy sources have been recently developed [4-6]. One of these technologies is thermoelectric (TE) systems that can convert waste heat into useful electrical energy [7]. In TE technology, TE materials, which are generally semiconductors, are used to convert the temperature difference into electrical potential and use it as electrical energy. Nowadays, different TE materials such as MgSi [8, 9], PbTe [10, 11], BiTe-based [12, 13], half-Heusler[1] [14, 15] and skutterudites[2] [16, 17] have been developed and started to find practical application in different industries such as automobile and marine etc [18].

The design of TE modules with sufficient efficiency at high temperatures is highly dependent on the TE material used [19]. Oxidation and sublimation, which occur at high temperatures and change the material microstructure and therefore TE performance, especially for TE materials with complex chemical composition and/or microstructures, limit the wider use of these TE materials. Accordingly, the high-temperature behaviour of the materials (oxidation and sublimation) must be fully investigated in order to design highly efficient and long-life TE modules and devices. To improve the thermal stability of TE materials and devices, oxidation-protective coatings have been developed [20-22].

[1] Half-Heusler TE materials have MNiSn and MCoSb structures, where M is Hf, Zr or Ti.
[2] Skutterudites are a kind of CoSb-based TE materials. The most studied skutterudite is $CoSb_3$ TE material.

In addition, achieving highly efficient TE modules is not only related the TE materials used but also closely related to the module design. Especially at the connection parts of TE materials and components, there must be an interfacial contact layer with high electrical and thermal conductivity to facilitate electron conductivity and heat transmission [23]. Another factor that should be taken into consideration is that the thermal expansion coefficients of the conductive interface layers are at similar values to that of the TE material. Otherwise, it may undergo mechanical degradation at high temperatures and during thermal cycles, thus reducing the performance and life of the TE modules.

Furthermore, electrical and thermal conductivity have a significant impact on the efficiency of TE materials. The figure of merit (zT) of a TE material is proportional to its electrical conductivity, while inversely proportional to its thermal conductivity. Therefore, ideal TE materials should have high electrical conductivity and low thermal conductivity. Unfortunately, it is well-known that it is difficult, if not impossible to decouple electrical conductivity from thermal conductivity in bulk materials. However, the electrical and thermal conductivity of TE materials could be optimised by nanostructured thin film technology and band engineering [24].

This PhD project was directed at developing technologies and advancing scientific understanding for efficient and long-life TE devices and systems. To this end, a series of research work has been conducted in the following four interconnected themes: (1) Investigation into the oxidation behaviour of N-type (Zr,Ti)Ni(Sn,Sb) and P-type (Zr,Ti)Co(Sn,Sb) TE materials under static and cyclic oxidation conditions; (II) Development and evaluation of CrSi coatings deposited by magnetron sputtering PVD for oxidation protection of the N-type and P-type TE materials; (III) Design and development of highly conductive Ni & NiGO metallising coatings as a contact layer deposited by low-cost and highly flexible electro-brush technique; and (IV) Development and characterization of magnetron sputtered BiTe-based thermoelectric thin films with high zT at low temperatures.

## 1.2 Thesis outline

In Chapter 2, the relevant literature on TE materials, the challenges of designing a TE module, and the solutions addressing these challenges were reviewed.

Chapter 3 provides the general experimental techniques including substrate materials, coating and thin film production, thermal stability tests, and general characterisation, which are used for the following research themes as reported in Chapter 4 to Chapter 7. Detailed descriptions of these experimental techniques are provided within respective chapters.

In Chapter 4, the cyclic oxidation behaviour of the N-type (Zr,Ti)Ni(Sn,Sb) and P-type (Zr,Ti)Co(Sn,Sb) TE materials tested at 500°C for 10, 30, and 50 cycles were systematically investigated by evaluating mass gain to study the oxidation kinetics and by analysing surface morphology, phase constitution and elemental distribution to investigate the oxidation mechanism.

In Chapter5, the deposition of oxidation-protective CrSi coatings on the N-type (Zr,Ti)Ni(Sn,Sb) and P-type (Zr,Ti)Co(Sn,Sb) TE materials was investigated. The static and cyclic oxidation behaviour of the CrSi-coated and uncoated materials were examined.

In Chapter6, the development of highly conductive Ni and NiGO coating layers was studied. The produced Ni and NiGO coatings on the stainless steel substrate were characterised and the optimised Ni coating was then deposited on P-type (Zr,Ti)Co(Sn,Sb) TE material as an interfacial contact layer.

In Chapter7, the production of BiTe-based thermoelectric thin films by using a closed-field unbalanced magnetron sputtering PVD system was studied. The output of electrical power of the thin film was tested at different temperature gradients.

In Chapter8, the outcomes from Chapters 4, 5, 6 and 7 were discussed to show their interconnection and provide an overall view of the PhD research; the major conclusions are summarised; and potential future work is proposed.

# Chapter 2 Literature review

## 2.1 Thermoelectric materials and modules

One of the most important facts of recent years is the increasing need for energy day by day. It is estimated that total energy consumption in 2005 will almost double in 2040 (Figure 2.1a) [25]. Most of such need is met by fossil-based fuels, and it is predicted that the use of fossil-based fuels will continue to be high in the future. As can be seen in Figure 2.1b, almost 84% of primary energy in 2022 was produced using fossil fuels [26].

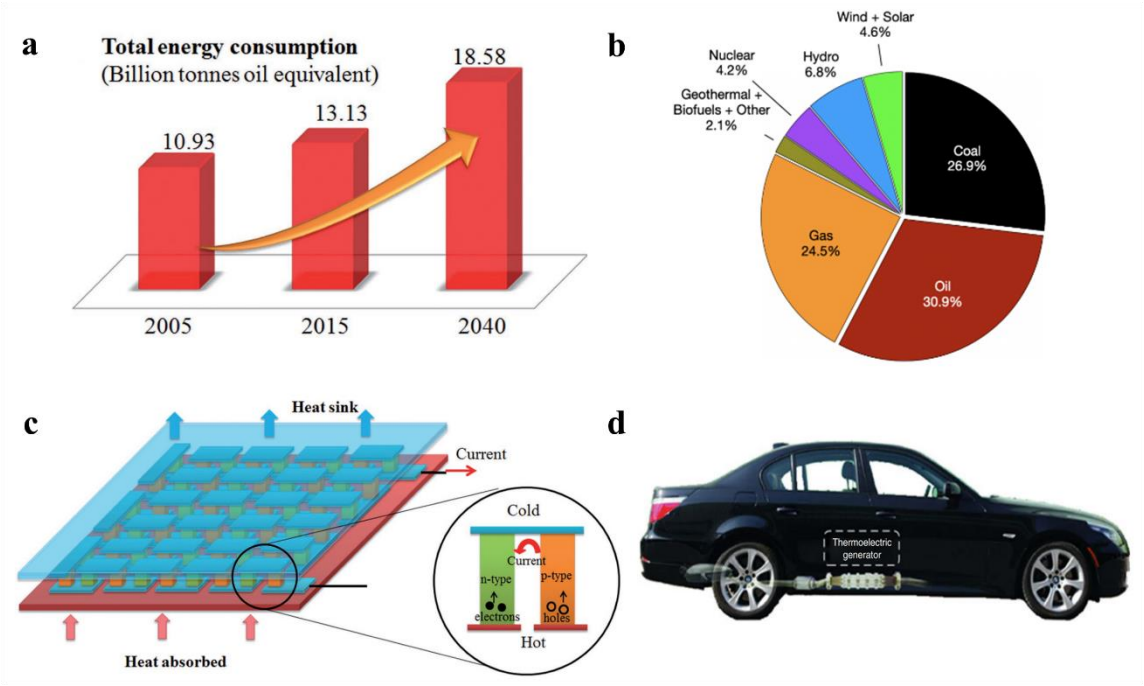


Figure 2.1. a) The energy consumption over the past years and an estimation for the future, b) the resources for the energy production in 2022, c) a thermoelectric power generator, d) a practical application of the thermoelectric power generator [25, 26].

On the other hand, alongside the high-capacity utilisation of traditional fossil-based (oil and natural gas) energy sources, the trend toward clean and renewable energy sources has also gained momentum. The most important factor in driving renewable energy sources instead of

fossil-based ones is to save the environment, and thus protect all living things. Recent technologies, like thermoelectricity, have also focused on eliminating the hazardous impact of waste heat, which is a kind of source of global warming, by producing clean electricity. A significant portion of the energy used in heavy industry is released into nature as waste heat, which can be directly converted into electrical energy thanks to thermoelectric power generators (Figure 2.1c) [25].

Thermoelectricity creates an electrical potential difference (voltage) when a temperature gradient between the junction of two different materials is applied, or conversely, creates thermal energy depending on the electric current applied [27]. Thermoelectric power generators are widely preferred in various industries, particularly in automotive, aerospace, solar systems, and individual applications [28-30]. Particularly in the automotive industry, studies on harvesting waste heat released from the exhaust and converting it into clean electrical energy have become attractive (Figure 2.1d) [31]. In addition, thermoelectric devices are independent of dynamic parts, environmentally friendly, and, with the latest advancements, a highly effective method of electricity production.

Thermoelectric power generators can convert body heat [32], heat from fossil-based energy sources [33], solar energy [34] and waste heat released from heavy industries into electrical energy. In addition to converting heat released within the scope of the transportation sector (automobile, motorcycle and ship), heat released from homes can also be converted into electrical energy by TE power generators [35]. In addition, radioisotope thermoelectric generators, which have become attractive in the last thirty years, have been used for space exploration [29]. The USA, in particular, has conducted special studies in this field and launched radioisotope thermoelectric generators into space for exploration on different planets (Jupiter, Saturn and Pluto) [36].

### *2.1.1 Seebeck and peltier effects*

The Seebeck effect explains the mobility of the electrons moving from the hot side to the cold side in conductive or semi-conductive materials when there is a heat difference between the two sides of the conductive or semi-conductive materials, resulting in an electrical voltage [37]. It describes the magnitude of a thermoelectric voltage built up when a temperature difference is applied across that material. Once the electrons move from the hot side to the cold side, the cold side is charged with negative metal ions while the hot side is charged with positive metal ions (Figure 2.2a). This theory was illustrated by Thomas Johann Seebeck for the first time in 1821, and it has been called as Seebeck effect [38]. Thermoelectric power generators are based on the Seebeck effect.

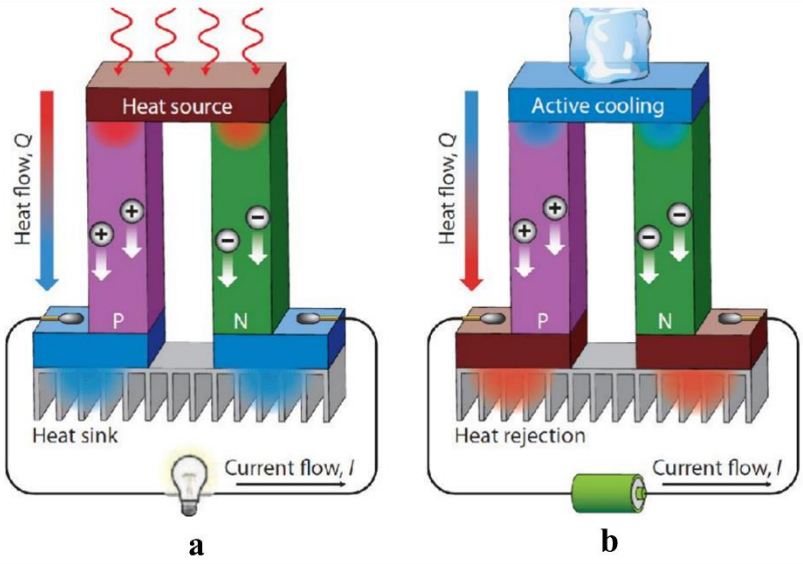


Figure 2.2. Schematic representation of a) Seebeck effect, b) Peltier effect [39].

Approximately 13 years after the discovery of the Seebeck effect, the Peltier effect, which is also considered the opposite of the Seebeck effect, was discovered by Jean-Charles-Athanase Peltier [40]. According to this effect, the current applied to the thermoelectric material pair heats the material on one side and cools the other side (Figure 2.2b) [39]. The direction of the

applied current determines which of the sides heats up and which cools down. In short, a thermal gradient can be created by applying an electric current. This effect is especially used in thermoelectric coolers.

### *2.1.2 Figure of merit (zT)*

Once the power generation by TE modules has become attractive since the released heat can be reused again and again as a power source in the same way, such studies have focused on improving the power factor of TE modules for an effective heat conversion even at low temperatures and applications in which the temperature difference is too low. The heat conversion efficiency of a module is closely related to the TE materials being used in the module. The power generation performance of a TE material can be assessed via the dimensionless figure of merit, zT, which is a combined function of Seebeck coefficient (S), electrical (σ) and thermal (k) conductivity, as seen in Equation 1 below:

$$zT = S^2\sigma T/k \qquad \text{(Equation 1)}$$

Table 2.1. Recent achievements in zT of different thermoelectric materials.

| Materials Bases | Temperature (K) | Power Factor ($\mu W\ cm^{-1}K^{-2}$) | zT | Ref. |
|---|---|---|---|---|
| SnSe | 300-773 | ~54 | >1.7 | [41] |
| GeTe | 670 | ~45 | 2.14 | [42] |
| BiSbTe | 375 | ~37 | 1.4 | [43] |
| $Bi_2S_3$ | 773 | ~5.5 | 0.7 | [44] |
| $Cu_2GeSe_3$ | 723 | ~8.7 | 0.75 | [45] |
| TaFeSb (HH) | 1025 | ~36 | 1.2 | [46] |
| $CoSb_3$ | 873 | ~72 | 1.7 | [47] |
| $Mg_2SiSn$ | 823 | ~40 | 1.61 | [48] |
| PbTe | 475 | ~56.8 | 2.36 | [49] |
| PbSe | 300-773 | ~24.18 | 1.01 | [50] |
| NbCoSb (HH) | 973 | ~28.9 | 0.78 | [51] |
| SnSe | 873 | ~9.8 | 2.1 | [52] |

Various TE materials like $Bi_2Te_3$, $Sb_2Te_3$, $CoSb_3$, SnSe, PbTe, GeTe, $Mg_2Si$, Half Heusler (HH) and oxide-based have been widely studied to enhance the zT value based on their temperature range. In general, the zT value of TE materials can be improved by micro and nano-structuring

[53-55], doping [25, 56, 57] and band engineering [58-61], considering the selection of environmentally friendly elements with high electrical conductivity as well as low thermal conductivity, and cost-effective production techniques. Recent achievements in developing TE materials with high zT values are summarised in Table 2.1.

## 2.2 Thermoelectric materials

### *2.2.1 BiTe-based materials*

BiTe-based TE materials are highly preferred in thermoelectric generators and coolers owing to their high zT (between 0.5 - 1.5) at low temperatures (up to 300°C) [55]. With the development of advanced material production techniques (doping, nanostructuring, etc.) and the improvement in thermal and electrical properties thanks to band engineering, the attractiveness of these materials in the thermoelectric sector has increased. As it is known, electrical conductivity is generally low at low temperatures, reducing the modules' heat-to-electricity conversion efficiency. From this perspective, BiTe-based materials and their alloys like n-type $Bi_2Se_3$ and p-type $Sb_2Te_3$ are promising materials targeting electricity generation even at small temperature differences in low-temperature applications while limiting the use of traditional coolers containing greenhouse gases by their use in the thermo-cooler sector.

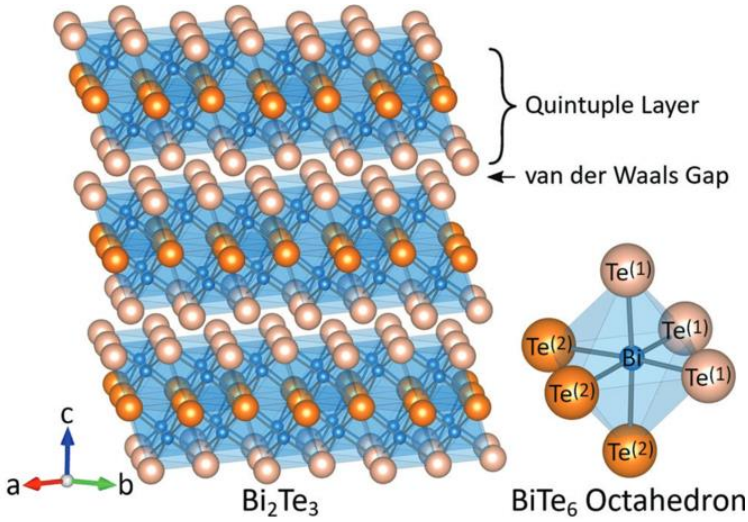


Figure 2.3. Atomic structure of $Bi_2Te_3$ material [62].

In $Bi_2Te_3$, the well-known BiTe-based materials, Bi and Te form an octahedral crystal structure ($Bi^{+3} + Te^{-2} = Bi_2Te_3$). The octahedral BiTe structures form a close-packed layered structure with which strong covalent bonds bond Bi and Te, while weak van der Walls bonds are formed between Te atoms [62]. Polarizable weakly bonded large atoms have a significant effect on the lattice thermal conductivity, which directly affects the TE performance of the material.

Researchers have currently developed high-zT BiTe-based TE materials used even at room temperatures over the past years (Figure 2.4). The figure shows that the researchers achieved a zT value greater than 1, which is a critical threshold for high-efficiency thermoelectric materials. Yeo *et al*. [63] produced multiwall carbon nanotubes (0.12 wt.%) dispersed $(Bi_{0.2}Sb_{0.8})_2Te_3$ nanocomposites with a high zT value of 1.41 at room temperature. One of the highest zT values of 0.97 at almost 150℃ for the n-type $Bi_2Te_3$ material was reported by Wang *et al*. [64], through fabricating the n-type porous nanostructured $Bi_2Te_3$ via a facile solvothermal method[3].

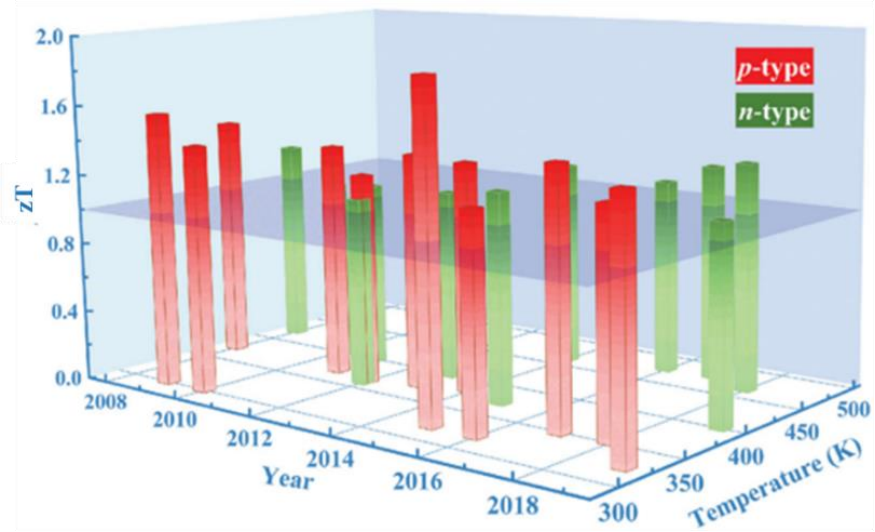


Figure 2.4. Temperature dependence peak zT values for the n-type and p-type $Bi_2Te_3$-based TE materials [65].

[3] Solvothermal synthesis is a reaction between reagents in a solvent (aqueous or non-aqueous) in a closed system at a temperature higher than the solvent's boiling temperature.

### *2.2.2 Half-Heusler compounds*

The half-Heusler (HH) structure was first discovered in 1903 by Heusler. HH materials recently attracted great interest because of their use in spintronics and thermoelectrics. There are more than 250 HH compounds that are semiconductors, enabling the potential application of these materials in TE modules. The majority of HH materials are complex structured and have been used for heat-to-electric conversion at moderate-to-high temperatures, which is critical for the TE industry. The TE efficiency of these materials is closely related to their chemical composition, which can tune the bang gaps, affecting the electrical conductivity.

HH materials have ABX and AB2X crystal structures consisting of a triple combination of transition metals (A and B) and main group elements (X), as shown schematically in Figure 2.5. These crystal structures typically have the MgAgAs structure type [66]. The ABX structure consists of three filled and one empty fcc sublattice, while the empty fcc sublattice is filled with B atoms in the $AB_2X$ structure. The thermoelectric properties of Half Heusler materials are evaluated according to the number of valence electrons. The different physical and chemical properties of the elements in the HH material make it difficult to obtain a single-phase compound. Thanks to band engineering developed in recent years, this difficulty has been addressed [59, 67]. As is known, most of the studies on HH compounds have been focused on MNiSn and MCoSb groups (M is Zr, Ti or Hf), exhibiting high thermoelectric properties, particularly at high temperatures. On the other hand, studies are currently being carried out to study the oxidation behaviour and mechanism of these materials at high temperatures [68, 69].

The thermoelectric performance of HH materials is improved by doping with rare elements such as Hf, which significantly affect thermal and electrical conductivity. On the other hand, high-cost rare elements limit the use of TE materials/modules in practical applications. For this reason, studies on the production of Hf-free HH compounds with high TE performance have gained momentum in the last decade. For example, Chauhan *et al.* [70] developed Hf-free Ni-

doped n-type ZrNiSn-based HH compounds with a zT value of almost 1.1 at 600℃. They also presented a similar achievement in zT (~1) of V-doped ZrNiSn-based material [71]. Joo *et al.* synthesised Hf-free n-type $Zr_{0.75}Ti_{0.25}NiSn_{0.98}Sb_{0.02}$ by serial processing of induction melting, annealing, ball milling and spark plasma sintering, with a zT of 0.92 at 600℃.

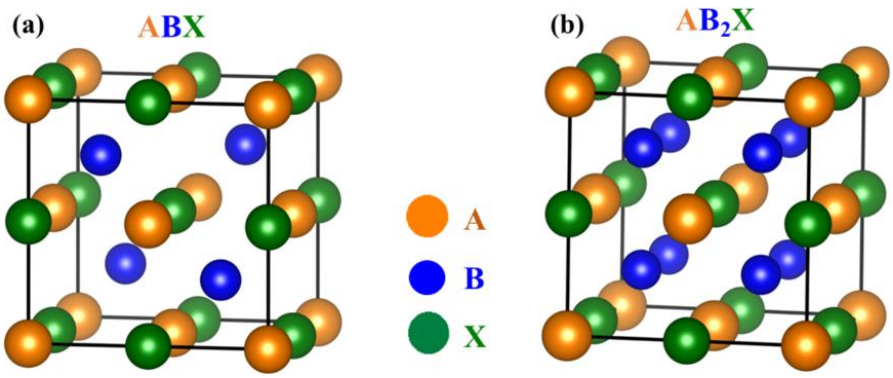


Figure 2.5. a) ABX and b) AB2X crystal structures of the Half Heusler materials [66].

When the studies on the development of novel N-type and P-type HH Materials with desired TE performance in the last decade are examined, it is seen that the peak zT value is obtained at high temperatures of 700℃ and above (Figure 2.6) [72]. However, despite the high zT value at high temperatures, it is necessary to prevent oxidation and sublimation, which affect the mechanical and thermal stability of the material.

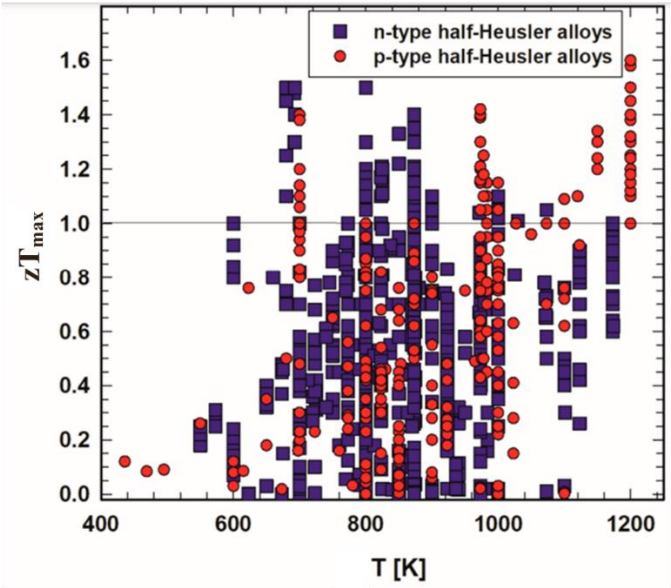


Figure 2.6. The maximum zT values achieved in the n-type and p-type HH compounds in the last two decades [72].

### *2.2.3 Skutterudites*

Skutterudites are materials with space group Im3 and contain 32 atoms in their cubic crystal structure. Its general formula is TPn3, determined by the transition metal (T, red spheres) and pnictogenes (Pn, yellow spheres), as schematically illustrated in Figure 2.7a [17]. The compound consists mainly of covalent bonds since the distance between the transition metals is quite large. The unit cells contain two voids in the structure, associated with rectangular distortions (Figure 2.7b) [73].

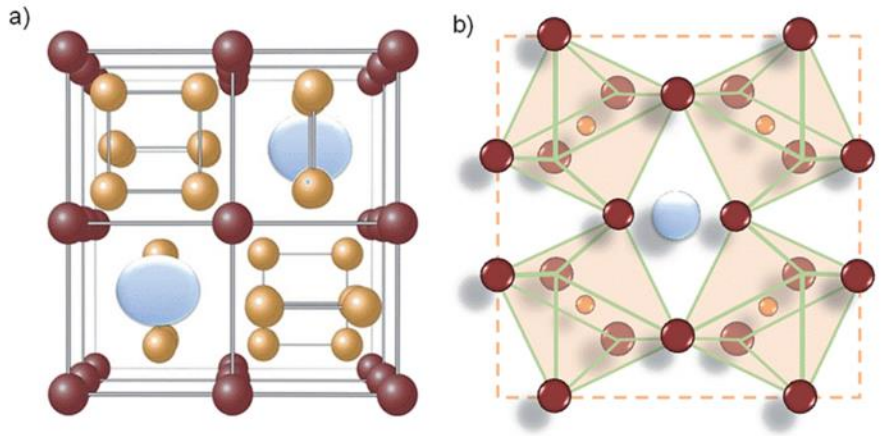


Figure 2.7. a) Unit cell and b) crystal structure of skutterudite TE materials [17].

These materials are used in the thermoelectric industry thanks to their superior properties such as cost-effectiveness, applicability at a wide range of temperatures (between 25℃ - 600 ℃), relatively high mechanical properties and thermal stability.

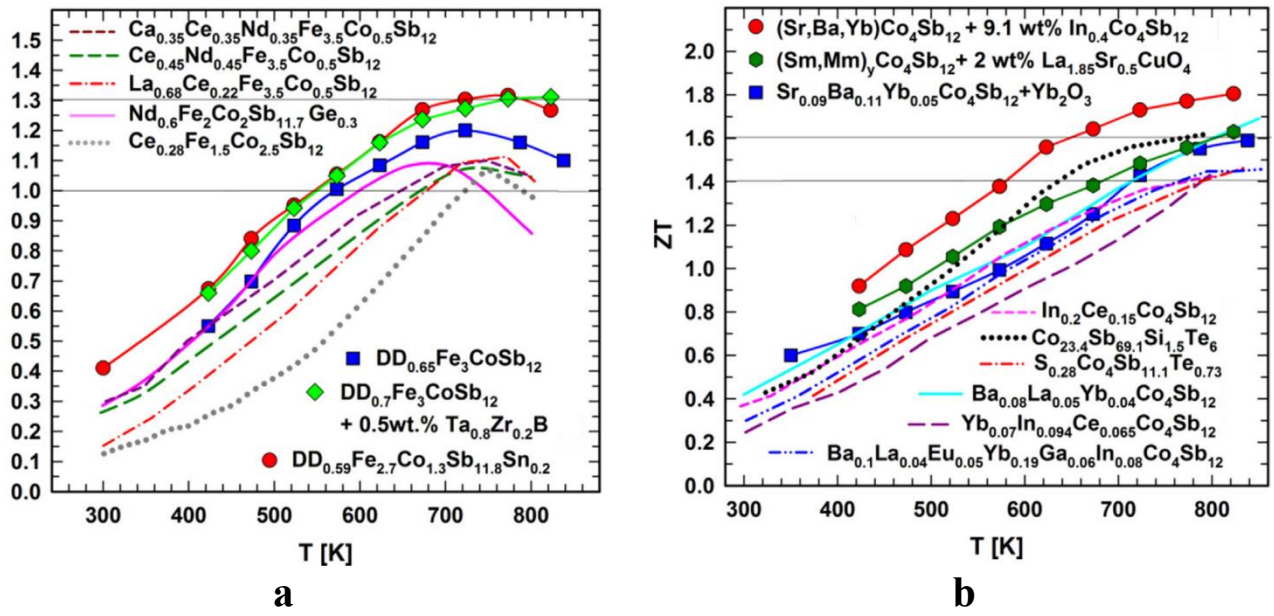


Figure 2.8. Recent achievements in zT of the bulk n-type and p-type skutterudites [16].

Critically, with recent advances, values of zT>1 have been reached, as shown in Figure 2.8. Rogl *et al.* [69] obtained a zT value of 1.45 at almost 575℃ for the produced bulk p-type DD0.7Fe2.7Co1.3Sb11.8Sn0.2. They also produced n-type (Sr, Ba, Yb)yCo4Sb12 + In0.4Co4Sb12 skutterudite with a zT of almost 1.8 at 550℃.

### *2.2.4 Mg-based materials*

MgSi-based TE materials are preferred for energy conversion in medium-temperature applications. $Mg_2Si$ is the most promising TE material among the Mg-based TE materials. In the $Mg_2Si$ structure, Si atoms occur in fcc form, while Mg atoms are located in all tetrahedral holes (Figure 2.9a) [74], which determines the carrier charge concentration of the structure [74]. The $Mg_2Si$ system has a low entropy, causing high thermal conductivity, which limits obtaining high zT values. For this reason, studies focused on reducing the lattice thermal conductivity to

improve the TE performance of the material. Current high zT values achieved for different Mg-based TE materials are summarised in Figure 2.9b & c [75].

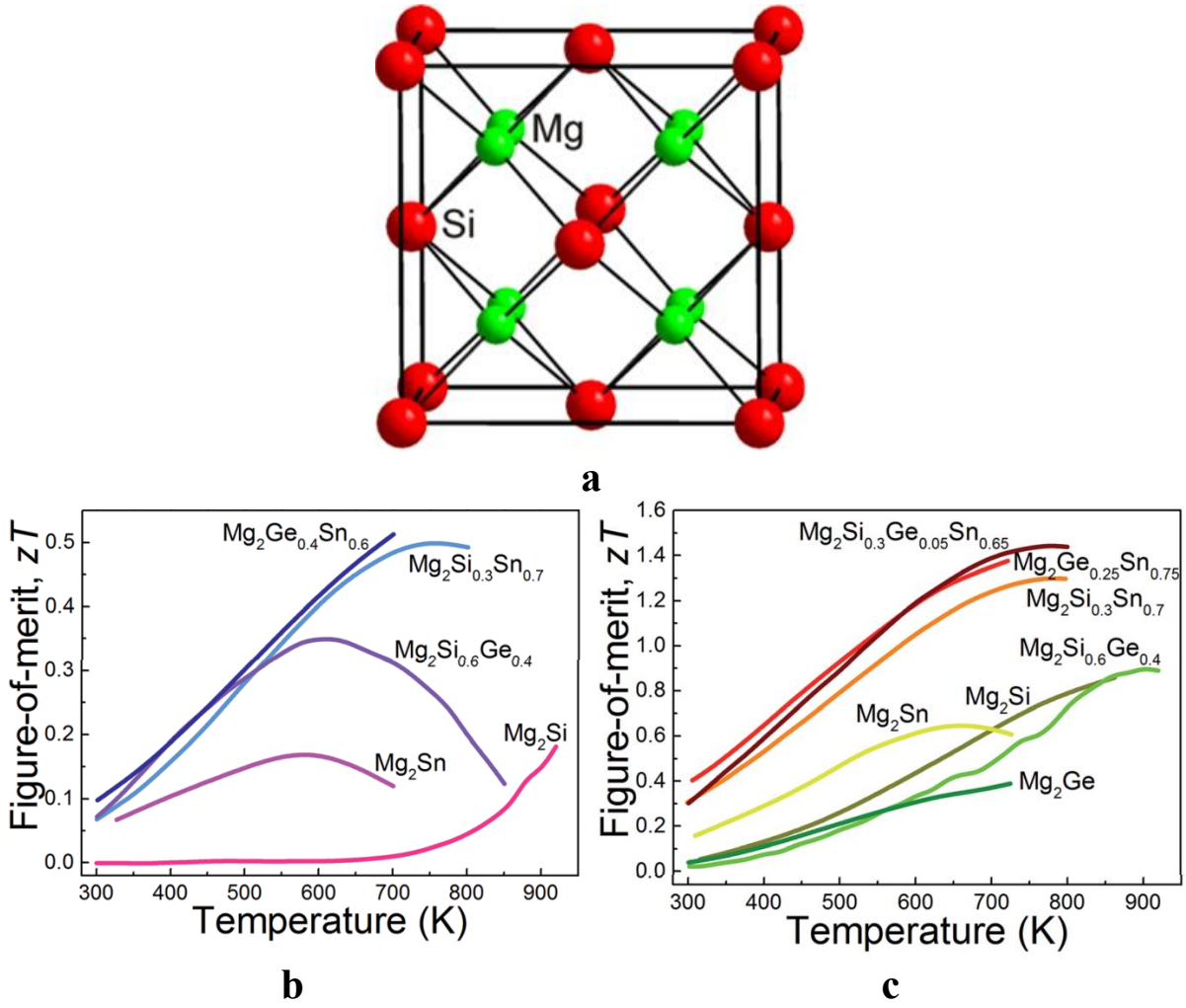


Figure 2.9. a) Crystal structure of $Mg_2Si$ material [74], and recent achievements in zT values of Mg-based TE materials; b) p-type and c) n-type [75].

## 2.3 Challenges in TE materials and devices

### *2.3.1 Insufficient zT*

To produce a TE power generator with high efficiency, a zT value of more than two is essential [76, 77]. Increasing TE efficiency via electron-crystal and phonon-glass properties can be created with high electrical conductivity and low thermal conductivity. It is possible to reduce

the thermal conductivity while preserving the electronic properties of the crystal by creating a large mass contrast and disrupting the photon path [78]. At the same time, a high Seebeck coefficient and electrical conductivity can be achieved by doping and alloying [79]. In this regard, many parameters need to be optimised in the design of high-efficiency thermoelectric materials. One of the most crucial parameters is the adjustment of the chemical composition of the TE materials. TE materials must consist of two or more elements with large atomic numbers to obtain distorted lattices that reduce thermal conductivity [80]. Doping or alloying can contribute to achieving specific mechanical and microstructural properties. On the other hand, nanostructuring is preferred to increase grain boundary density, enhance photon scattering, and reduce thermal conductivity [81]. The nanostructuring of the material contributes specific properties to the material, which positively affects TE performance. After the determination of the chemical composition and micro/nano-structures, the production technique of the material is also very critical. High TE performances are achieved thanks to modern production techniques ensuring that TE materials with a stable composition are compatible with nominal values and relatively reduced production costs [82]. Nowadays, melting, mechanical alloying and deposition methods are widely used to produce TE materials. In addition to the synthesis of the materials, the sintering process is of great importance for the final performance of TE materials synthesised by the high-tech powder metallurgy method [78]. Temperature, pressure and time parameters are optimized to create stable structures with high density in the desired composition. In recent years, spark plasma sintering process with high sintering efficiency has been widely used [83-85].

As discussed above, the production of thermoelectric materials with high energy conversion efficiency is a complex process in which many parameters are considered and is still a major challenge for many TE material groups. Even though many studies have focused on developing high-performance TE Materials, the low-cost production of clathrates, GeTe-based, half-

Heusler, BiTe-based and SnTe-based materials is still a concern in the last decade, as can be seen in Figure 2.10, which limits their use in practical applications.

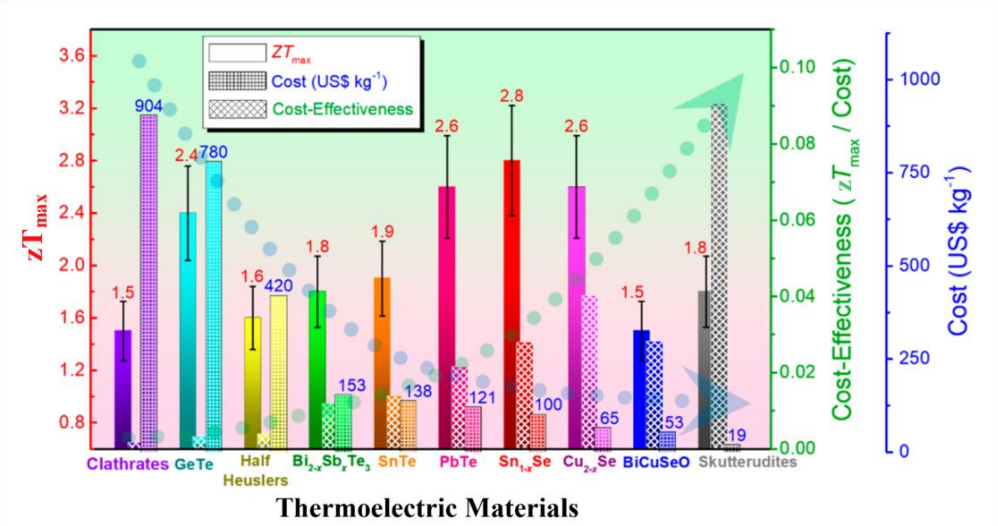


Figure 2.10. Maximum zT values for state-of-the-art thermoelectric materials with the calculated cost and cost-effectiveness [86].

### *2.3.2 Low chemical stability*

Most TE materials are involved in high entropy alloy groups and contain several different elements. They may oxidise in air at high temperatures, and some elements with low melting temperatures may sublimate [87]. In both cases, the microstructure and mechanical properties of the material change, which affects the thermoelectric performance.

#### *2.3.2.1 Oxidation*

Oxidation of materials occurs when the material reacts with oxygen or by the diffusion of oxygen into the material, which affects their chemical stability. Although the oxidation behaviour of some of the thermoelectric materials has been studied in the literature, the oxidation mechanisms have not been fully established. The main reason for this is the availability of TE materials with very different compositions and microstructures. Nevertheless,

studies involving the effects of oxidation on TE materials shed light on the oxidation behaviour of state-of-the-art TE materials. Zhao *et al.* [88] studied the oxidation behaviour of $CoSb_3$ TE material at 500℃ and 650℃. They observed a parabolic mass gain between 500℃ and 600℃ and tremendous weight loss at 650℃ because of the sublimation of $Sb_2O_3$. It was also reported that the TE performance was considerably worsened after the oxidation at 650℃ for 48 hours. High-temperature oxidation behaviour of ZrNiSn-based Half-Heusler TE materials was investigated by Wang *et al.* [89]. They reported the formation of alternated layers including oxidation products of $ZrO_2$, $HfO_2$, $SnO_2$ and $Ni_3Sn_2$ compound at 450℃ & 500℃. Li *et al.* [90] performed a study on the oxidation behaviour of SnSe materials at 600℃ & 700℃. It was reported that SnSe oxidised at 600℃ formed oxidation products of $SnO_2$ and $Sn(SeO_3)_2$ and $SnSe_2$ compound, which are different from the initial microstructure. Another research on the oxidation mechanism of ZrCoSb-based half-Heusler thermoelectric compounds was carried out by Jinyu *et al.* [69]. Three typical layers named the dense oxide layer (DOL), the alternate oxide layer (AOL) and the CoSb layer were characterised on the surface of the material after oxidation in air in the service temperature range from 600℃ to 800℃. The dense oxide layer consists of $(ZrHf)O_2$ and CoSb, while the alternate oxide layer is composed of repeated (Zr, Hf)$O_2$ and $CoSb_2O_6/Co_3O_4$. A study on the oxidation behaviour of MgSi-based TE materials, which have high chemical activity, was carried out by Inoue *et al.* [91], describing that $Mg_2Si$ reacted with the elements in air (O, H) and formed $Mg(OH)_2$, which decomposited at the operational temperature of the MgSi-based TE materials (400℃).

As can be seen from the Figure 2.11, the oxidation not only resulted in a chemical composition change but also causes mechanical degradation, leading to a decrease in the service life of the TE modules. From the abovementioned studies regarding the effect of oxidation on the chemical stability of various TE materials, it is critical to prevent oxidation of the TE materials at medium-to-high temperatures.

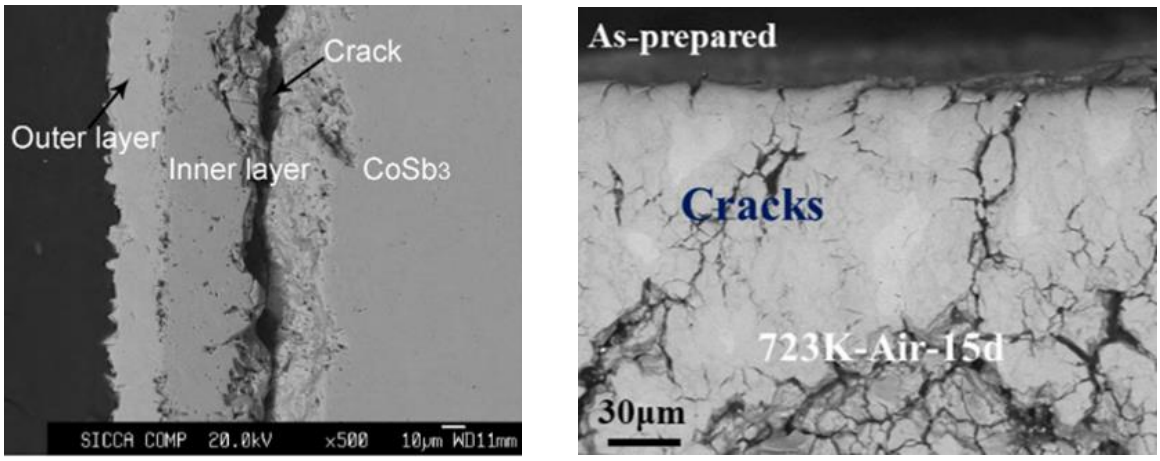


**a** **b**

Figure 2.11. Crack formation as a result of the oxidation; a) $CoSb_3$ material oxidised in air at 650°C for 72 hours [88], b) ZrNiSn-based material oxidised in air at 450°C for 15 days [89].

*2.3.2.2 Sublimation*

One of the important factors that may degrade thermoelectric materials is the sublimation of their volatile elements. For example, telluride (Te) in PbTe, GeTe and BiTe-based materials [92, 93], antimony (Sb) and its oxides in skutterudites [94], and similarly Sb and tin (Sn) in half-Heusler Materials [95] sublimate at medium and high temperatures, changing the composition and microstructure of the material as well as contributing to the degradation of the material. In addition, the sublimated volatile element may react with other elements in the microstructure during sublimation and cause the formation of new phases, affecting the thermoelectric performance of the material. This problem is especially evident if the quantity of Te, Sn and Sb is high in the chemical composition of the materials. For example, when the Te composition is greater than the stoichiometric composition of $Bi_2Te_3$, the use of these materials is limited to 450°C or below due to Te sublimation [96]. In skutterudites, both Sb and its oxide ($Sb_2O_3$) sublimate, causing not only microstructural changes but also structural defects [88, 97]. Another well-known example is Half Heusler TE materials with high Sn and Sb composition. Sn, which has a low melting temperature (~232°C), tends to sublimate even at low temperatures.

Zhao *et al.* [94] studied the high-temperature sublimation behaviour of Sb in $CoSb_3$ by the thermal duration test at 600℃ & 750℃. They reported that the sublimation of Sb followed a parabolic law and caused cracks at the grain boundaries, leading to micro-cracks after the thermal duration test. The sublimation rate of the p-type $Yb_{14}MnSb_{11}$ thermoelectric material at 1000℃ was tested by Nesbitt *et al.* [98]. The findings of the study indicated that the rate of sublimation decreased with time, resulting in the formation of $Yb_2O_3$ on the material surface, which also contributed to reducing the rate of sublimation. The sublimation behaviour of Te in Te-including TE Materials was studied by Ohsugi *et al.* [99], presenting that Te is dissociated and moves to the surface to form a liquid or amorphous state at temperatures between 200℃ - 400°C in PbTe-based materials, while it may sublimate in BiTe-based materials at lower temperatures below 400℃. Silicon-germanium-based TE materials including silicon (Si) are primarily sublimated in the forms of silicon monoxide ($2Si + O_2 = 2SiO$) at high temperatures, which can then create an electrically conductive layer by decomposing to $Si_2$ and $O_2$, affecting TE performance of the SiGe-based materials [87].

### *2.3.3 Poor mechanical properties*

The mechanical properties of materials stem from their atomic structures. Whether the atomic bonding occurs through strong ionic and covalent bonds or weaker Van der Waals forces determines the mechanical properties of the material. In addition, the physical properties of the elements in the composition also play a role in determining the final mechanical properties. In this regard, thermoelectric materials are expected to possess sufficient mechanical strength to withstand various service conditions [100]. As known, TE materials are covalent semiconductors and are unable to show plastic deformation. These polycrystalline materials contain some defects that reduce mechanical strength as they are generally prepared by melting and powder metallurgy. Demonstrating effective mechanical resistance under static and cyclic thermal operating conditions ensures stable thermoelectric performance [101].

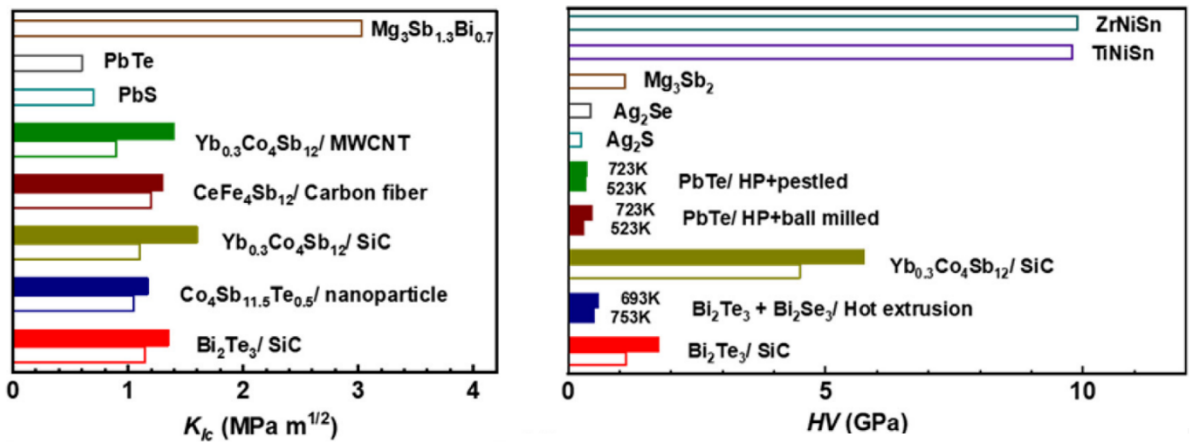


Figure 2.12. a) Fracture toughness and b) Vickers hardness of the thermoelectric materials and their optimisation [100].

TE materials that cannot endure internal stress caused by wide temperature gradients degrade over time, making the TE module dysfunctional. TE materials must exhibit the desired mechanical properties suitable for the temperature range in which they are utilised. Accurate measurement and characterization of the mechanical properties of TE materials contribute to saving critical aspects such as money, time, and efficiency in practical applications. When characterizing the mechanical properties of thermoelectric materials, factors such as elastic modulus [102], strength and hardness [103], fracture toughness [104] and fatigue resistance (fatigue limit) [105] are generally considered. The fracture toughness and hardness of some of the TE materials are summarised in Figure 2.12.

### *2.3.4 Module assembly issues*

It is very difficult to achieve high thermoelectric efficiency using similar module designs for different thermoelectric materials. As is known, thermoelectric materials with different microstructure and mechanical properties exhibit different behaviours depending on the application temperature [78, 106]. This situation requires the optimisation of other aspects of TE generator assembly. Even if a thermoelectric generator consists of TE materials with high

zT values, a poor assembly results in very poor thermoelectric performance [107]. During TE module assembly, interface and contact resistance and thermal bridge should be considered [108].

*2.3.4.1 Interfacial issues and contact resistance*

Thermoelectric generator design requires systematic and advanced engineering approaches. High energy conversion efficiency is expected from the generator involving multicomponent such as TE materials, contact layers, electrode layer and the ceramic layer, which are integrated [109]. This integration directly affects the efficiency of the thermoelectric generator.

High efficiency is not only related to thermoelectric materials with high zT values, but also related effective transferring of charged particles through material interfaces (Figure 2.13) [110]. When designing the material interface, many factors such as high electrical and thermal conductivity, high zT value, low electrical and thermal contact resistance, cost-effective interface applicability, effective oxidation resistance and thermal stability and coefficient of thermal expansion (CTE) compatibility are taken into account [111-114].

Another important issue affecting efficiency is the electrode interfaces [115]. As electrical and thermal resistance decreases, electron transport occurs more desirably. In addition, its stability at the interface depending on the application process prolongs the usage period of the thermoelectric generator with high efficiency [115, 116].

In high-temperature applications, thermoelectric materials suffer from oxidation and elemental sublimation, as explained in detail under the heading of "degradation". As a result of oxidation and sublimation, the thermoelectric performance of the material is negatively affected. To overcome this problem, surface coatings that are resistant to oxidation are applied [117, 118]. These protective layers preserve the mechanical and microstructural properties of the material at high temperatures. The critical requirements are that the deposited coating should not react

with the TE material at high temperatures, should not cause any diffusion, and should be cost-effective and easy to apply [119, 120].

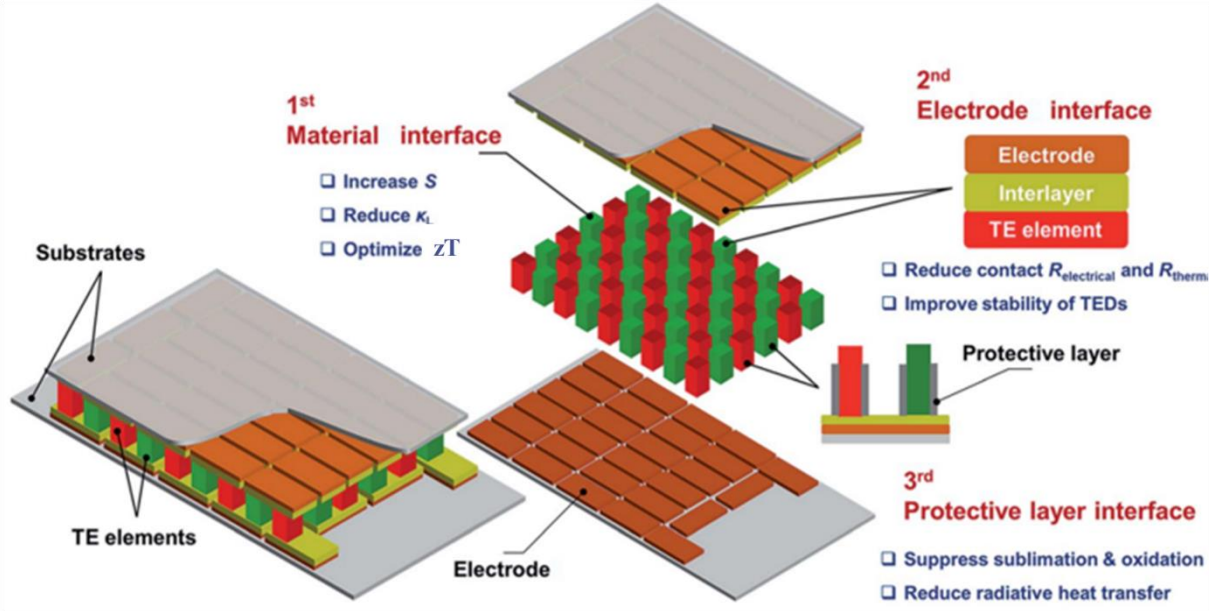


Figure 2.13. Schematic representation of the contact issues [110].

*2.3.4.2 Thermal bridges*

In TE generators, thermal bridge formation is taken into account when additional assembly designs are applied under a homogeneous pressure to ensure high thermal conductivity at the connection points [121]. A thermal bridge, by definition, is a phenomenon that reduces thermoelectric performance by passing the heat flow through the path of additional areas or objects that have lower heat resistance and thus higher thermal conductivity than the thermoelectric material [108, 122]. The main components that cause the thermal bridge in thermoelectric generators are the metallic screws used at the connection points. Another thermal bridge is seen in thin thermoelectric generators, where some of the heat is released rather than passing through the thermoelectric module. Insulating interface materials are generally used to prevent thermal bridge formation [108].

## 2.4 Enhancement in TE materials and devices

### *2.4.1 Improving thermoelectric efficiency of materials*

#### *2.4.1.1 Doping*

Thermoelectric performance of TE materials can be improved by doping, which affects the Seebeck coefficient, and electrical and thermal conductivity. Depending on the TE material type, improving the carrier density by stimulating it with different dopants has been recommended for high-efficiency applications [123]. At the same time, the band structure can be adjusted as desired by the doping effect. The fact that carrier density is a temperature-dependent parameter requires its optimisation for TE materials operating in a certain temperature range. As it is known, the Seebeck coefficient decreases with increasing carrier concentration. However, by manipulating the electron bands through doping, the Seebeck coefficient can be kept constant while increasing the electrical conductivity, which significantly improves TE performance [124]. Another important effect of doping is seen in the thermal conductivity of TE materials [125]. Phonon contribution is a factor affecting thermal conductivity, and many studies have focused on reducing thermal conductivity by reducing the phonon contribution. Active dopants cause lattice mismatch by creating nanoscale defects in the material microstructure that delay phonon scattering. Delayed phonon scattering reduces the phonon effect on thermal conductivity [126]. The main parameter affecting this process is temperature. Because the scattering of long wavelength phonons increases with increasing temperature. In recent years, many studies have been conducted on improving the performance of TE materials through doping, as summarised in Table 2.2.

Table 2.2. Recent enhancements in TE properties of different TE materials by effective dopants.

| TE Material Group | Material | Type | Dopant | T (K) | S (mV/K) | κ (W/mK) | zT | Ref. |
|---|---|---|---|---|---|---|---|---|
| BiTe-based | $Bi_{0.52}Sb_{1.48}Te_3$ | p | Pb | 350 | ~ 235 | ~1.5 | ~1.12 | [127] |
| | $Bi_{0.7}Sb_{0.3}Te$ | n | Sb | 400 | ~ -90 | ~1.4 | ~0.35 | [12] |
| | $Bi_2Te_{2.5}Se_{0\ 5}$ | n | $WCl_6$ | 425 | ~ -190 | ~1.2 | ~1.10 | [128] |
| | $Bi_2Te_{2.9}Se_{0\ 1}$ | n | Se | 390 | ~ -73 | ~0.5 | ~0.60 | [129] |
| | $(Cu_2Te)_{0.09}(Bi_2Te_3)_{0.91}$ | n | Cu | 400 | ~ -180 | ~1.9 | ~1.00 | [130] |
| | $Bi_{1.95}Ge_{0.05}Te_3$ | p | Ge | 300 | - | ~0.4 | ~0.95 | [131] |
| | $Bi_2Te_3Se$ | n | Cl | 450 | ~ -170 | ~0.6 | ~1.00 | [132] |
| | $Bi_2Te_2S$ | n | Cr | 400 | ~ -125 | ~1.7 | ~0.37 | [133] |
| Half Heusler | $FeNb_{0.84}Hf_{0.1}Ti0.06Sb$ | p | Hf-Ti | 1200 | ~ 190 | ~4.1 | ~1.30 | [134] |
| | $Ti_{0.6}Zr_{0.4}Co_{0.93}Ni_{0.07}Sb$ | n | Ni | 900 | ~ -185 | ~3.7 | ~0.52 | [135] |
| | $NbCoSb_{0.8}Sn_{0.2}$ | n | Sn | 973 | ~ -190 | ~0.9 | ~0.56 | [136] |
| | $NbFe_{0.94}Ir_{0.06}Sb$ | n | Ir | 1000 | ~ -220 | ~4.1 | ~0.50 | [137] |
| | $Zr_{0.9}V_{0.1}NiSn$ | n | V | 873 | ~ -200 | ~3.0 | ~1.00 | [71] |
| | $TiFe_{0\ 15}Co_{0.85}Sb$ | p | Fe | 850 | ~ 300 | ~4.5 | ~0.45 | [138] |
| Skutterudites | $Yb_{0.3}Co_4Sb_{12}Si_{0.1}$ | n | Si | 823 | ~ -190 | ~3.4 | ~1.37 | [139] |
| | $CoSb_{2.85}Te_{0.15}$ | n | Te | 820 | ~ -190 | ~3.5 | ~0.98 | [140] |
| | $Ce_{0.9}Fe_{3.75}Ni_{0.25}Sb_{12}$ | p | Ni | 773 | ~ 170 | ~2.7 | ~0.90 | [141] |
| | $Co_4Sb_{11.3}Te_{0.6}S_{0.1}$ | n | S | 800 | ~ -180 | ~3.2 | ~1.08 | [142] |
| MgSi-based | $Mg_2Si_{0.97}Bi_{0.03}$ | n | Bi | 810 | ~ -89 | ~6.6 | ~0.68 | [143] |
| | $Mg_2Si_{0.296}Sn_{0.666}Bi_{0.037}$ | n | Bi | 700 | ~ -265 | - | ~1.75 | [144] |
| | $Mg_2Si_{0.9}Sn_{0.1}Al_{0.02}$ | n | Al | 864 | ~ -250 | ~2.8 | ~0.68 | [145] |
| | $Mg_{0.64}Si_{0\ 11}Sn_{0.18}Ge_{0.7}$ | p | Ge | 473 | ~ 225 | ~0.8 | ~0.22 | [146] |
| | $Mg_2(Si_{0.3}Sn_{0.7})_{0.975}Sb_{0.025}$ | n | Sb | 640 | ~ -240 | ~2.3 | ~1.00 | [147] |

* T, S and κ are temperature, Seebeck coefficient and thermal conductivity, respectively.

*2.4.1.2 Nanostructuring*

Obtaining high TE performance from bulk TE Materials (Figure 2.14a) is limited due to the difficulty of providing both high electrical conductivity and low thermal conductivity. Although thermal conductivity has been tried to be limited by doping, a bulk TE material with a zT value of higher than three has not yet been produced for practical applications. Furthermore, lattice thermal conductivity can be minimised by using the ability of nanostructured materials to scatter medium and long-wavelength phonons [148].

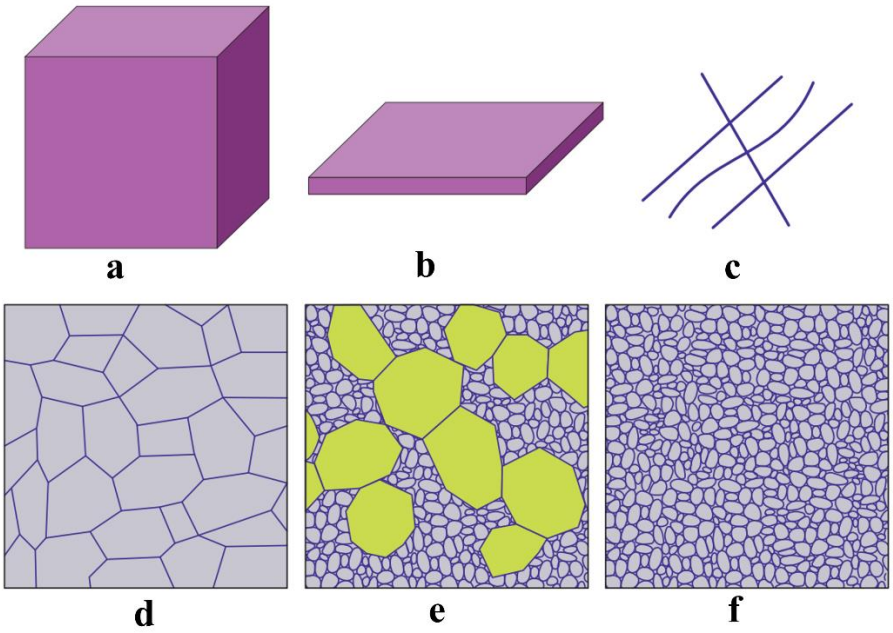


Figure 2.14. Macro, micro and nanostructures of thermoelectric materials; a) bulk, b) thin film, c) nanowires, d) coarse micro-grains, e) coarse and fine grains, f) fine nano-grains [149].

As is known, nanostructuring includes thin films (2-D, Figure 2.14b), nanowires (1-D, Figure 2.14c) and quantum dots (0-D). As shown in Figure 2.14 d-f, structuring the grain size at the nanoscale, on the one hand, increases the grain boundary, which reduces the thermal conductivity and, on the other hand, causes its electron mobility to worsen. To balance this effect of the grain boundary, micro-scale coarse and nano-scale fine grains are created in the microstructure (Figure 2.14e) [149]. In a nanocomposite TE material structure, nanoparticles trigger phonon scattering, while microparticles create a path for electron transport.

### *2.4.2 Improvement in interface design*

#### *2.4.2.1 Matching of coefficient of thermal expansion*

High electrical and thermal conductivity in the contact layers of thermoelectric materials can be achieved by introducing suitable conductive interfaces. However, the coefficient of thermal expansion (CTE) of the contact layer and the thermoelectric material must be compatible [150]. This feature is of great importance for TE materials used in high-temperature applications [151].

If there is a noticeable CTE mismatch in a thermoelectric generator, this will lead to increased interfacial stress over time and degradation of the TE generator [87]. It is also important to prevent such degradation, especially for TE generators that will be preferred in critical applications such as the automotive and space industries. Therefore, the CTE matching between TE materials and contact materials should be highly compatible with each other. CTE incompatibility can be addressed by selecting and/or designing advanced materials.

Petrova *et al.* suggested a chromium contact layer instead of nickel as it has a close matching CTE (~$10\times10^{-6}$ $K^{-1}$) [152], showing an enhanced durability of the coating layer when it suffers from high-temperature oxidation. Daylon *et al.* designed a metal-ceramic composite to manage the thermal stress occurring because of CTE mismatching. They matched the CTE of the designed contact layers including alumina and copper with the nanostructured half-Heusler TE materials ($10-12\times10^{-6}K^{-1}$), reduced interfacial shear stress by 40% and achieved ultrahigh power density of 8.6 $W/cm^2$ [153], which can improve the TE power generation capability of the TE modules. Lin *et al.* produced doubled-layer electrodes of $W/TiB_2$ and $W/MoSi_2$ using a glass encapsulation hot-isostatic-pressing process and added $Si_3N_4$ ceramic particles to reduce the mismatch of the CTE. The produced electrodes were applied to the n-type and p-type SiGe TE materials and the outcome of the study suggested that the residual stress can be reduced by the addition of 40 vol% $Si_3N_4$ into the $TiB_2$ layer and 55 vol% $Si_3N_4$ into the $MoSi_2$ layer.

*2.4.2.2 Reducing contact resistance*

An increase in the actual thermoelectric efficiency can also be achieved by reducing contact resistance. In a TE generator, optimisation of the contact interface between the TE material and the electrode is performed by microstructural evaluations, determination of surface properties (roughness, etc.), measurement of electrical and thermal conductivity, and testing of mechanical properties [23, 154].

In the literature, several studies have focused on reducing contact resistance for high thermoelectric performance. Ngan *et al.* [155] used a fast hot-pressing method to join n-type and p-type half-Heusler materials to a silver (Ag) electrode. The research outcome suggests using the fast-hot-pressing technique to directly bond the studied TE materials to the Ag electrode, resulting in lower contact resistance and improved energy conversion efficiency. Tan *et al.* [156] developed a titanium (Ti) contact layer to achieve ultralow contact resistance of ~4.8 Ω in an as-assembled BiTe-based thin-film TE device. The study indicated that the Ti contact layer between the $Bi_2Te_3$ TE material and copper (Cu) electrode strengthened the p&n junctions and reduced the contact resistance more than ten times compared to the system without the Ti layer. A nickel (Ni) layer was also suggested to minimise the contact resistance of BiTe-based TE modules [157]. It was said that the application of the Ni barrier layer can reduce 32% of contact resistance in p-type and n-type joints. Camut *et al.* [158] investigated the contacting of $Mg_2Si$(Sn, Sb) material to an aluminium (Al) electrode. This resulted in oxidation at the joints and obtaining asymmetric electrical contact resistivities on both sides of a leg (e.g., 10 $\mu\Omega\cdot cm^2$ and 200 $\mu\Omega\cdot cm^2$). As a solution, they suggested zinc (Zn) sputtering on the Al electrode to ensure consistent and lower contact resistance at the joints. The contact resistance can also be reduced by adjusting the geometry of the TE legs and devices [159, 160].

### *2.4.1 Protection against oxidation*

#### *2.4.1.1 Coatings*

Protective coatings are the most preferred method to prevent or delay oxidation of thermoelectric materials. For this purpose, specific requirements are needed in the coatings applied to TE materials. One of these is oxidation barrier coatings, which must have low electrical conductivity to prevent short circuits in the TE module. Another feature is that the thermal conductivity must be as low as possible to prevent heat loss. Moreover, the coatings must have sufficient thermomechanical properties at mid-to-high temperatures. All these

parameters should be taken into consideration when applying advanced surface technologies to TE materials and elements.

In the literature, different kinds of coatings like enamel, glass, titanium (Ti), oxide and hybrid have been employed on various TE materials. For example, silica-based enamel coating was deposited on the n-type $Ba_{0.05}Yb_{0.025}CoSb_3$ and the p-type $Ce_{0.9}Co_{0.5}Fe_{3.5}Sb_{12}$ skutterudites for oxidation suppression [21]. It was reported that the enamel coating with desired mechanical properties can protect the n & p-type skutterudite materials against static and cyclic oxidation up to 600℃ for 8 days in the air. The thermal stability of a silica-based glass coating on the $Mg_2Si_{0.487}Sn_{0.5}Sb_{0.013}$ TE material was studied by Fabiana *et al.* [161]. The produced coating provided effective protection against oxidation at 500℃ for 120 hours in the air. Ning *et al.* [162] deposited silica-based glass-ceramic coatings onto the higher manganese silicide to prevent oxidation. They reported that the deposited coating had good densification behaviour as well as chemical compatibility with the substrate. It is worth pointing out that the TE performance of the glass-ceramic coated material also showed the desired stability. A borosilicate glass coating with a high content of titania was deposited on $CoSb_3$ TE material and its oxidation behaviour was investigated. The findings of the study showed that the coating had a good adherence and effectively protected the materials when tested at 600℃ for 20 hours [163]. Zhao *et al.* [164] deposited titanium (Ti) on $CoSb_3$ material using a magnetron sputtering PVD system. The oxidation of the substrate was significantly delayed by the Ti coating at 650℃ for 24 hours when compared to the uncoated sample. An interesting study was carried out by Park *et al.* [165] to investigate the oxidation suppression by four different oxide coatings of alumina ($Al_2O_3$), yttria ($Y_2O_3$), 8 mol% yttria-stabilized zirconia ($(Y_2O_3)_{0.08}(ZrO_2)_{0.92}$), and 20 mol% samaria-doped ceria ($Sm_{0.2}Ce_{0.8}O_{1.9}$) on $Mg_2Si$ TE materials. Their investigation indicated that $Al_2O_3$, $Y_2O_3$ and $Sm_{0.2}Ce_{0.8}O_{1.9}$ failed to prevent the substrate from oxidation at 700℃, while $Y_2O_3)_{0.08}(ZrO_2)_{0.92}$ coating showed a good oxidant resistance. Al-Ni double-

layered coating was employed onto the $Yb_{0.3}Co_4Sb_{12}$ TE material using electrochemical deposition, and the oxidation behaviour of the coating was tested at 500℃ for 30 days [166]. The effectiveness of the coating was evaluated by the change in the TE performance of the coated material after the oxidation testing when compared to the uncoated sample, showing that almost no alteration in the TE performance was observed in the Al-Ni coated sample. A commercial hybrid solvent-based coating was deposited on $Mg_2Si$ TE legs and the reduced oxidation rate was achieved at 500℃ for 120 h [167].

As can be seen in the above-summarised studies, it is evident that thermal reliability can be obtained by the oxidation barrier coatings. However, the majority of the researchers have generally focused on developing glass or glass-based composite coatings for the oxidation protection of TE materials using conventional methods. It would be noteworthy that the applicability of the produced coatings on different kinds of TE material is greatly important in practical applications. Furthermore, very limited or almost no reference scientific study on the protection of some other TE materials like complex-structured Half Heusler by the advanced coating techniques can be found in the literature.

*2.4.1.2 Pre-oxidation*

Pre-oxidation is based on the principle of delaying oxygen diffusion and obtaining relatively high mechanical properties, due to an oxide layer deliberately created on the material surface. As it is known, the diffusion of oxygen into the oxide is approximately 108 times more difficult than its diffusion into the bulk, which means that oxidation is significantly prevented [168]. As a new and simple approach, pre-oxidation is proposed by the researchers for effective oxidation protection by preventing oxygen diffusion into the bulk TE materials. For example, Wang *et al.* [89], suggested pre-oxidation at 500℃ for three days for $Zr_{0.5}Hf_{0.5}NiSn_{0.985}Sb_{0.015}$ HH material for excellent thermal stability between room temperature and 500℃ for 15 days. Gu *et al.* [69] also studied the effect of pre-oxidation on the thermal stability of ZrCoSb-based

($Zr_{0.5}Hf_{0.5}CoSb_{0.8}Sn_{0.2}$) HH compounds. They created oxidation-protective (Zr,Hf)$O_2$ and CoSb layers by pre-oxidizing at 500°C for three days in low oxygen pressure, and achieved considerably effective thermal stability in the air. Although significant progress has been made in the protection of some TE materials by pre-oxidation, investigation of the TE performance of the materials in practical applications after pre-oxidation is still needed.

# Chapter 3 Experimental Procedure

This chapter provides the general experimental techniques including substrate materials, coating and thin film production, thermal stability tests, and general characterisation, which are used for the four following research topics as reported in Chapter 4 to Chapter 7. Detailed descriptions of these experimental techniques are provided within respective papers/chapters to reduce or avoid unnecessary repetition.

## 3.1 Substrate materials

Several types of substrate materials were used in this PhD study in order to achieve the research objectives.

### *3.1.1 Stainless steel*

Commercially available 316 stainless steel was selected the substrate for the development and optimisation of Ni&NiGO coating. The stainless steel road was cut to approximately 4 mm thick coupons with Struers Accutom-50 or Buehler Isomet cutting devices, depending on machine availability. The obtained circular samples were ground up to 1200 grit using SiC papers. The samples were then cleaned ultrasonically in deionized water and acetone for 10 minutes. Depending on the requirements, some of the samples were mounted in a conductive bakelite using an OPAL mounting device. Some samples for SEM cross-sectional examinations were ground with SiC paper up to 4000 grits, then polished using 3 μm of diamond paste and finally cleaned as described above.

### *3.1.2 Thermoelectric materials*

N-type (Zr,Ti)Ni(Sn,Sb), P-type (Zr,Ti)Co(Sn,Sb) half-Heusler TE materials and Si wafers were used as substrates for CrSi coatings. Industrial metal powders of Zr, Ti, Ni, Co, Sn and Sb were used in the right proportion to produce the N & P-type samples with the targeted nominal composition. The samples with dimensions of 4×0.5×0.5 $cm^3$ were obtained by mechanical

alloying in an argon (Ar) inert environment. A specific mechanical alloying equipment, which oscillates high energy ball mill in the grinding, meaning that the process is accelerated to affect the surfaces at high velocities. This method considerably reduces the abrasion and shear effects, which lead to a decrease in contamination from the milling means to the milling materials, by transferring the kinetic energy directly from grinding to the powders. The samples were then plasma sintered at 800°C for 4 minutes under a pressure of 500 kg/cm² using a uniaxial press (DSP 475, Dr. Fritsch).

Due to the limited availability of n-type TE materials, electro-brush plating of Ni & NiGO was performed only on the p-type (Zr,Ti)Co(Sn,Sb) HH compound. The same sample preparation procedure as the stainless steel was followed for the p-type material before Ni & NiGO deposition and their characterisation.

#### *3.1.3 Substrates for thin film deposition*

Glass, silicon wafers, special chips (ZT $Al_2O_3$ (ALD) Au contact chips for Linseis TFA supplied by SemiMetrics Limited), and Kapton polymer substrates were used as the substrate for the deposition of BiTe-based TE thin films. As known, polyimide-based Kapton HN has an excellent balance of properties at temperatures between -269 and 400°C, making it an ideal substrate for TE film deposition. Since the surface of these substrates is already suitable for the deposition of thin film, only the cleaning process was carried out before deposition as described above.

## 3.2 Coating and thin film production

### *3.2.1 Brush plating*

#### *3.2.1.1 Preparation of plating solutions*

Commercial Ni ductile solution, (the name of nickel plating solution) was supplied by SPA Plating (UK) for Ni plating. The NiGO plating solution was prepared in two stages. Firstly, 4

g/L GO suspension was prepared using 0.2 g GO powders activated in 50 mL deionised water by ultrasonication for 2 hours. In the second stage, 1.25 mL, 2.5 mL and 3.75 mL of the prepared GO suspension were mixed with 50 mL of Ni ductile and subjected to ultrasonication for one hour to obtain final compositions of 0.1 g/L, 0.2 g/L and 0.3 g/L NiGO suspensions, separately.

*3.2.1.2 Ni & NiGO deposition*

Ni and NiGO coatings were deposited using the electro-brush plating kit developed by SPA Plating, which enables the precise output of DC voltage (Figure 3.1). The anode cell of the device was integrated with a carbon electrode, while the cathode cell was in contact with the sample. The carbon electrode was covered by cotton to prevent short-circuit and surface damage during direct contact. During the ongoing cleaning and coating processes, the electrode was immersed in the solutions every ten seconds to avoid drying cotton, which may cause a degradation of the coating. The final parameters of the Ni and NiGO electro-brush plating were obtained as a result of the optimisation study given in Chapter 6 detailed in Table 3.1.

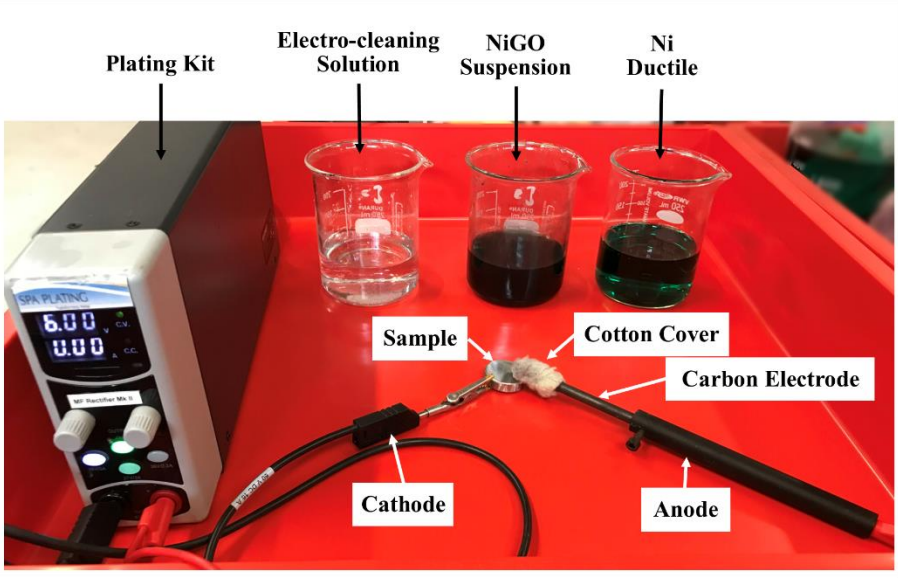


Figure 3.1. Electro-brush plating process.

Table 3.1. Plating procedures for electro-brush plating of Ni and NiGO.

| Operation | Substrate | Voltage (V) | Time (min.) |
|---|---|---|---|
| Electro-cleaning | Stainless steel | 10 | 1 |
| | TE material | | |
| Electro-plating | Stainless steel | 6 | 30 |
| | TE material | | 10 |

### *3.2.2 Magnetron sputtering*

CrSi coatings and BiTe-based thin films were produced using a closed-field unbalanced magnetron sputtering PVD system (Teer Coatings Ltd., Droitwich, UK). This system allows using separate targets to achieve the desired nominal composition. For CrSi coatings, Cr and Si targets were placed opposite each other in the PVD equipment and a constant current of 2 A was applied to the Cr target, while a 0.3 A to the Si target. These are the optimum parameters obtained from our previous optimisation study on producing high-quality CrSi coatings on stainless steel substrate [169]. The coating process was performed in 3 different steps. In the first step, ion cleaning, the constant currents of 0.2A and 0.05A were applied to Cr and Si targets, respectively, under high bias (almost 200V) to remove possible contaminations. In the second step, changeover, the current applied to the Cr and Si targets gradually increased to 2A and 0.3A, respectively, while the bias was reduced from 200V to approximately 40V. The last step, the coating process, was carried out for 70 minutes with the specified parameters detailed in Chapter 5. The sample holder was rotated at 5 rpm to obtain a homogeneous coating.

BiTe-based thin films were deposited on glass, silicon wafers, special chips (ZT $Al_2O_3$ (ALD) Au contact chips for Linseis TFA supplied by SemiMetrics Limited), and Kapton polymer substrates using the highly pure (99.99%) n-type $Bi_2Te_3Se$ and p-type $BiSb_2Te_3$ targets. Thin films were deposited using currents of 0.3 A, 0.4 A, 0.45 A, 0.5 A, and 0.6 A over different periods. The thin-film production procedure is the same for the CrSi coating with the ion cleaning, changeover and deposition stages.

## 3.3 Thermal stability tests

The produced Ni & NiGO coatings were separately annealed at temperatures of 100℃, 200℃, 300℃… up to 800℃ for half an hour in the muffle furnace (Pyrotherm) in air. Additionally, the Nickel coatings were also oxidised at 500℃ for 10 hours to determine the thermal stability.

CrSi-coated samples were cyclically oxidised in the muffle furnace. Before starting the oxidation test, a control test was carried out on the oxidation and weight gain of the ceramic sample holder at the working temperatures and durations. Once the reliable test conditions were achieved in terms of the ceramic sample holders, each test sample was put into a tested ceramic sample holder to measure the mass gain more accurately. Following the oxidation of the samples at 500℃ for one hour, they were taken out of the furnace, cooled to room temperature for 15 minutes, and weighed using an Ohaus precision scale with a sensitivity of $10^{-4}$ g. The weighed samples were placed back in the oven. This process was repeated 50 times for each sample and the mass gain was calculated specifically for each sample according to the dimensions.

## 3.4 General characterisation

### *3.4.1 Scanning electron microscope (SEM)*

Surface morphology and cross-sectional layer structure examinations were conducted using the Jeol SEM7000 (Jeol UK Ltd.) and Apreo2 (Thermofisher Scientific) scanning electron microscopes. In most cases, the acceleration voltage was kept at 20 kV and the working distance was 10 mm. Samples were attached to a sample holder using a conductive carbon sticker. Before the SEM examination, the sample preparation procedure described before was followed to get high-quality images. For the majority of the cross-section analyses, back-scattered electron detectors were preferred to get a clear contrast for the elemental characterisation.

### *3.4.2 Energy dispersive X-ray spectroscopy (EDX)*

The in-situ elemental analyses were performed by the EDX instrument (Oxford Instrument) fitted to the Jeol SEM7000 and Apreo2. The SEM image quality based on the working distance, accelerating voltage and electron beam spot size was obtained as high as possible for accurate EDX analyses. Spot, line and mapping requisition modes were used for the elemental characterisation for each sample.

### *3.4.3 Transmission electron microscope (TEM)*

50 square mesh, 3.05 mm diameter copper TEM grids (Agar, Scientific Ltd) were used for TEM samples of BiTe-based thin films. A few grids were put onto a sample hold plate of the PVD equipment before the deposition process. A short-time deposition procedure was designed for the TEM samples but kept the other parameters the same as the real thin films produced.

The deposited thin films were stuck along the grid sides, where the TEM observations were carried out. The Joel 2100 electron microscope (LaB6, 200 kV, Japan) was employed for taking the TEM microstructures and selected area diffraction (SAD) patterns.

### *3.4.4 X-ray diffraction (XRD)*

The phase constitution of the produced bulk TE materials, coatings and thin films was characterised by a ProtoA X-ray diffractometer with a Cu-Kα source ($\lambda$ = 1.540598 Å). With the coupled scan mode and fixed resolution of 0.01493 ($\Delta 2\theta$ degree), the $2\theta$ range of 20º–90º was adopted with a step size of 0.5º ($2\theta$) and dwell time of 2 (seconds) for the analyses. The acquired XRD patterns were analysed through the Highscore Plus software.

### *3.4.5 Surface roughness*

The 2-D surface roughness measurement was performed using an Ambious XP-200 profilometer (Cntech, UK). The sample holder plate was flatted before the measurement, and the sample surface was scanned by a diamond tip probe with a scanning speed of 0.05 mm/s

over 8 mm in length. The measurements were repeated five times on the same sample surface at different regions, and the average was taken.

### *3.4.6 Glow discharge optical emission spectroscopy (GDOES)*

Compositional data were gathered employing a GDOES instrument (GDA650HR Spectruma Analytik) within an inert gas (Argon) at a pressure of 335 Pa. The analysis was carried out for depth profiling of the Ni & NiGO coatings on the stainless steel, focusing on a diameter of 2.5 mm. The thickness of the coatings was also quickly determined by GDOES, which was confirmed by the surface profilometer scanning the crater depth after GDOES analyses.

### *3.4.7 Sheet resistance*

The sheet resistance of TE materials among different components in a TE module is critical as it determines the heat and electron exchange when a temperature difference occurs upon the TE legs. In this project, an Ossila four-probe instrument, wherein two probes applied a current while the remaining probes measured the voltages (Figure 3.2) was used to measure the sheet resistance of Ni/NiGO layers.

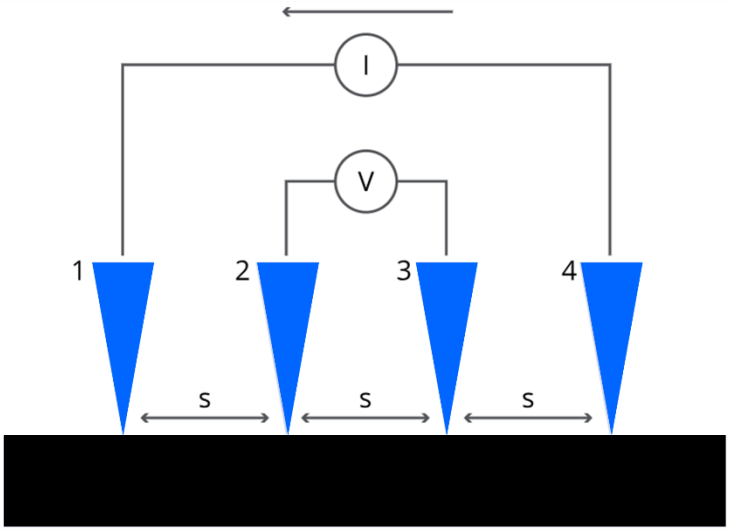


Figure 3.2. Schematic of four probe sheet resistance measurement equipment

Specific details such as sample thickness and shape were input into the device, and the measurements were acquired as close to the centre of the samples as feasible, ensuring proper contact of the probes with the sample surface. The measurements were repeated at least five times, and the resulting average was calculated and reported.

## 3.5 Mechanical property assessment

It is essential to produce a coating layer with a robust mechanical hardness to deal with a large thermal stress, as well as make the material surface tolerable to degradation when designing a multicomponent-TE module. To this end, Vickers micro-indentation measurement studies were conducted using Zwick-Roell hardness equipment. Following the application of a light initial load to the sample surface for 10 seconds, the load of 10 g, based on the material and coating thickness to be examined. Hardness measurements were repeated at least five times for each sample, and the resulting average was calculated.

Nanoindentation measurements were also conducted using a NanoTest Vantage instrument (Micro Materials Ltd.). The initial contact load of 0.02 mN was applied and increased to a maximum load of 20 mN. Loading and unloading durations were both set to 30 seconds, with a dwell time of 5 seconds at the maximum load. Each sample was subjected to nanoindentation testing at least 5 times from different regions. Analysis of raw data was performed using the integrated software and the nano-hardness was determined from loading-unloading curves.

# Chapter 4 Cyclic oxidation behaviour of n-type (Zr,Ti)Ni(Sn,Sb) and p-type (Zr,Ti)Co(Sn,Sb) thermoelectric materials

* This chapter has been published in the Journal of Materials Research and Technology.

**[1]Gurtaran, M.,** [1]Zhang, Z., [1]Li, X., & [1]Dong, H. (2024). Cyclic oxidation behaviour of N-type (Zr, Ti) Ni (Sn, Sb) and P-type (Zr, Ti) Co (Sn, Sb) thermoelectric materials. Journal of Materials Research and Technology, 30, 7476-7484. https://doi.org/10.1016/j.jmrt.2024.05.136

1- School of Metallurgy and Materials, University of Birmingham, Birmingham, UK

**Acknowledge of Collaborative Work:**

**Mikdat Gurtaran:** Writing-Original draft, Methodology, Validation, Investigation; Zhenxue Zhang: Investigation; Xiaoying Li: Writing – Review & Editing, Validation, Conceptualization; Hanshan Dong: Supervision, Funding acquisition.

## 4.1 Abstract

In this study, the fabricated Hf-free N-type (Zr,Ti)Ni(Sn,Sb) and P-type (Zr,Ti)Co(Sn,Sb) thermoelectric materials were subjected to cyclic oxidation testing at 500°C for 10, 30, and 50 cycles. The oxidation behaviour of the materials was systematically investigated by evaluating mass gain to study the oxidation kinetics and by analysing surface morphology, phase constitution and elemental distribution to investigate the oxidation mechanism. The results indicated that both of the materials were severely oxidised during the cyclic oxidation testing, and the mass gain followed the parabolic kinetics and the parabolic rate constant ($k_p$) being 0.006165 $mg^2cm^{-4}s^{-1}$ and 0.000109 $mg^2cm^{-4}s^{-1}$ for the N-type and the P-type TE materials, respectively. Alternated multilayers of $Ni_3Sn_4$+$SnO_2$+$(Zr,Ti)O_2$ and CoSb+$SnO_2$+$Sb_2O_4$+$(Zr,Ti)O_2$ were identified on the surface of the N-type and P-type materials, respectively, after the cyclic testing, which would deteriorate the thermoelectric performance of the materials. The outcome of this study strongly suggests that it is essential to improve the oxidation resistance and the thermal stability of the N-type (Zr,Ti)Ni(Sn,Sb) and P-type (Zr,Ti)Co(Sn,Sb) thermoelectric materials for high-temperature applications.

## 4.2 Introduction

Thermoelectric materials (TE) are crucial for efficiently converting waste heat into electrical energy to meet the ever-growing energy demands [37, 170] and the net-zero target, which has attracted extensive research interests in developing new TE materials with a high figure of merit, zT value ($zT=S^2\sigma\kappa^{-1}T$) for high thermoelectric performance, combining the Seebeck coefficient (S), electrical conductivity (σ), thermal conductivity (κ), and absolute temperature (T) [79, 171]. Many thermoelectric materials are being explored for power generation applications, such as GeTe [172], $Bi_2Te_3$ [173], PbTe [56, 174], and half-Heusler compounds [175]. Researchers have been also working on improving the zT value of such commercially available thermoelectric materials as Bi-Te [62, 176, 177] and Pb-Te [11, 178, 179] compounds.

However, these TE materials contain critical raw element Bi and toxic heavy metal Pb. Therefore, the state-of-the-art half-Heusler [67, 180, 181], SnTe [182-184], and MgSi-based [74, 185, 186] TE materials, with comparable or superior thermoelectric performance and lower ecological impact, are being rapidly developed.

As most half-Heusler materials contain Hafnium (Hf), a costly critical raw element, researchers have recently developed more cost-effective and sustainable Hf-free and Hf-substituted half-Heusler materials [187, 188]. It is known that the oxidation behaviour of TE materials is highly composition dependent. Removal of chemically active element Hf from Hf-containing half-Heusler alloys would change their oxidation behaviour. Notably, Hf-free half-Heusler thermoelectric materials have gained recognition for their remarkable thermoelectric performance because of the high zT values between 0.7 and 1.5 as a function of the working temperature, indicating efficient heat-to-electricity conversion [70, 189]. Chauhan *et al.* [180] increased the zT value of Hf-free half-Heusler materials to approximately 0.8 at 500°C. Zhang *et al.*[190] produced Hf-free N-type ZrNiSn with a zT value of 0.78 at 500°C. Min *et al.* [191] achieved a significantly improved zT value of 0.89 for Nb-doped ZrNiSn half-Heusler compounds. Further progress was made by Nguyen *et al.* [181], producing Hf-free N-type $(Ti_{0.5}Zr_{0.5})_{1-x}Nb_xNiSn$ half-Heusler material via a fast production technique, which is a combination of arc-melting, melt spinning and spark plasma sintering. They obtained a zT value of 1.19 at 600℃ with the optimised composition with x= 0.0125.

However, thermal stability and oxidation behaviour at high service temperatures are concerns for thermoelectric generators. In particular, most TE generators and devices work in frequent heating and cooling thermal cycles, which present an even more challenging environment [192]. Kang *et al.* reported that the power output of thermoelectric generators involving MCoSb (P-type) materials was reduced by 50% after 120h at 823K in air [193]. To ensure sufficient thermal stability, thermoelectric materials must have high oxidation resistance [194, 195] to

prevent surface damage, segregation and sublimation [196, 197]. This is because such oxidation-related surface damages can act as barriers to the movement of charged particles and heat carriers, thus reducing electrical conductivity and hence the performance of TE materials. For example, it is reported by Kikuchi *et al.* that the electrical resistivity of polycrystalline $Ba_8Ga_xAl_ySi_{46-x-y}$ type-I clathrates was increased with increasing temperature, leading to a significant decrease in the zT value [198]. Additionally, sublimation of elements such as Sn and Sb at high temperatures alters the composition and critical properties of TE materials, possibly negatively impacting electrical and thermal conductivity. Therefore, understanding the oxidation and sublimation behaviour and the mechanisms involved is vital to designing and developing high-performance and long-life thermoelectric materials as well as providing essential information for developing advanced surface coatings to protect TE materials from oxidation and sublimation.

The present study is focused on investigating the oxidation behaviour of a new generation of Hf-free and cost-effective N-type (Zr,Ti)Ni(Sn,Sb) and P-type (Zr,Ti)Co(Sn,Sb) thermoelectric materials produced by mechanical alloying followed by spark plasma sintering. The fabricated TE blocks were subjected to cyclic oxidation testing between 500°C and room temperature for 10, 30 and 50 cycles in air since the majority of TE materials experience continuous heating and cooling cycles in practical applications. The oxidation behaviour and mechanisms of the N and P-type samples were investigated by mass gain measurements, surface morphology evolution, cross-section layer characterisation and phase transition analyses. Future research directions for developing thermoelectric materials with improved thermal stability and advanced oxidation protection surface coatings are proposed based on the new insights into the oxidation behaviours and mechanism of the Hf-free half-Heusler TE materials.

## 4.3 Experimental

### *4.3.1 Fabrication of TE materials*

The test samples (with dimensions of approximately 4×0.5×0.5 $cm^3$) were produced by MATRES Scrl (Italy) and the chemical composition is shown in Table 4.1. To achieve the desired concentration of materials, industrial metal powders (Zr, Ti, Ni, Co, Sn, and Sb) were obtained, and the mechanical alloying was conducted in an inert environment using the high-energy ball mill technique, which allowed for controlled impact velocities as well as minimising defects observed in traditional alloying methods. The green compact of the metal powders was plasma sintered for 4 minutes at 800°C and under a pressure of 500 kg/cm² using a uniaxial press (DSP 475, Dr. Fritsch).

Table 4.1. Chemical composition (at. %) of the fabricated thermoelectric materials.

| Materials | Code | Elements | | | | | |
|---|---|---|---|---|---|---|---|
| | | Ti | Ni | Co | Zr | Sn | Sb |
| (Zr,Ti)Ni(Sn,Sb) | N | 17.1 | 33.5 | 0 | 16.3 | 32.3 | <1.0 |
| (Zr,Ti)Co(Sn,Sb) | P | 16.4 | 0 | 29.1 | 18.1 | 10.7 | 25.7 |

### *4.3.2 Cyclic oxidation testing*

The testing samples were cut to dimensions of 0.5x0.5x0.5 $cm^3$ and ground up to 1200 grit using SiC abrasive papers. The samples were then ultrasonically cleaned in acetone for 5 minutes. Cyclic oxidation testing was conducted in a muffle furnace, and each test sample was individually placed in a ceramic container. When the temperature reached 500°C, the samples with ceramic containers were swiftly loaded into the furnace to avoid a sharp temperature drop. It only took about two minutes to reach the set temperature of 500°C, and the samples remained at 500°C for 1 hour before they were removed from the furnace and cooled in air to room temperature. This designed thermal cycle (Figure 4.1) was repeated 10, 30, and 50 times for all

N and P-type samples. Before and after each test cycle, the weight of the samples within the ceramic container was measured using a high-precision scale (Ohaus, Switzerland) with an accuracy of $10^{-4}$ g. Three repeated measurements were made, and the average was reported. Detailed sample codes and their corresponding conditions are summarised in Table 4.2.

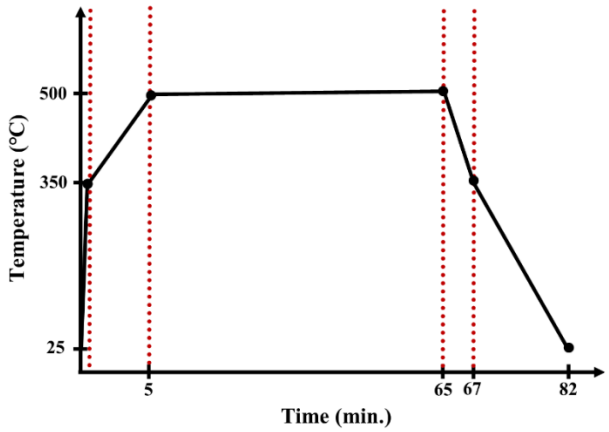


Figure 4.1. Schematic representation of one thermal cycle of the oxidation testing.

Table 4.2. Sample codes and corresponding processing details.

| Sample Code | | Oxidation cycles at 500°C |
|---|---|---|
| N | P | 0 cycle (As-produced N-type and P-type pellets) |
| N-10 | P-10 | 10 cycles |
| N-30 | P-30 | 30 cycles |
| N-50 | P-50 | 50 cycles |

### *4.3.3 Microstructural characterisation*

Comprehensive microstructure analysis was carried out on N and P samples before and after cyclic oxidation tests. Surface and cross-sectional microstructures of the TE materials were investigated by scanning electron microscopy using Jeol 7000 and Apreo2 SEM (Jeol-UK Ltd., UK and Thermofisher Scientific, UK, respectively) with an EDX device for analysing chemical concentration and distribution. Samples were XRD scanned by a ProtoA XRD diffractometer

employing a Cu-Kα source (λ = 1.540598 Å), and phase identification was carried out using High Score Plus software.

## 4.4 Results

### *4.4.1 Mass gain of cyclic-oxidation tested N & P-type TE samples*

The mass gains of the tested samples were measured and calculated after each cycle, and the obtained data are presented in Figure 4.2a. For as-produced N and P-type samples, the mass gain shows a parabolic trend. This is confirmed by the straight lines shown in Figure 4.2b when plotting the square of the mass gain $(\Delta m/A)^2$ against the number of cycles (N), which is proportional to the time (t). The mass gain of the N-type samples increased much faster than that of the P-type samples throughout the cyclic oxidation testing process. At the end of 50 cycles, the final mass gain for the N-type sample was 5.8 mg/cm$^2$, while it was only 2.1 mg/cm$^2$ for the P-type sample.

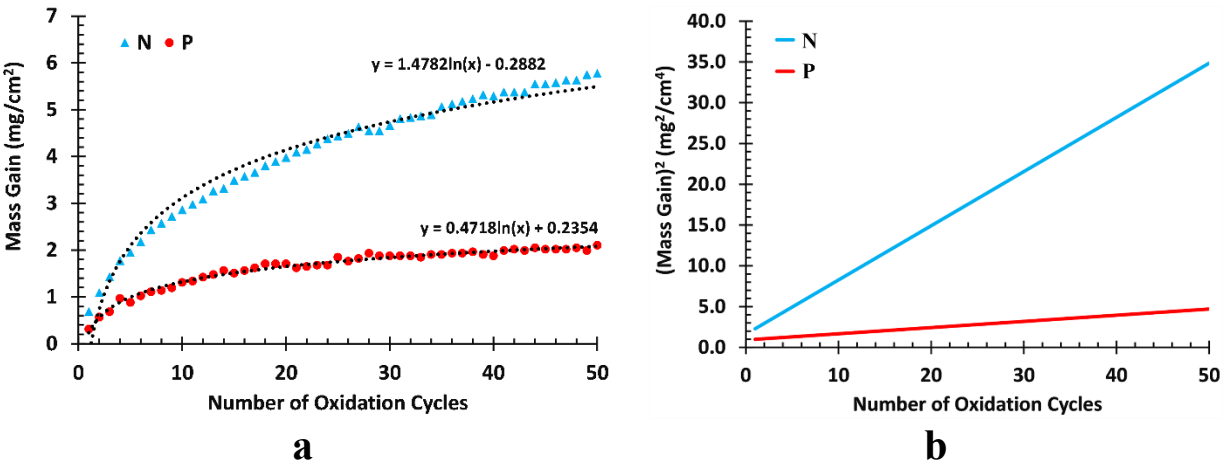


Figure 4.2. Mass gain (a) and the square of the mass gain (b) of the oxidised N and P-type samples as a function of the number of cycles.

### *4.4.2 Phase changes after cyclic oxidation tests*

XRD patterns of as-received N and P-type samples are compared to the oxidised samples as shown in Figure 4.3. Before oxidation, the diffraction pattern of the N-type sample shows a single half-Heusler phase of (Zr,Ti)Ni(Sn,Sb) (cubic, a= 0.603 nm, PDF: 01-089-7155),

crystalising in the C1b structure type. The main phase formed in the P-type material is a typical half-Heusler phase of (Zr,Ti)Co(Sn,Sb) with the crystal structure of C1b, a= 0.599 nm. Some traces of weak peaks can be tentatively indexed to Sb (rhombohedral, a=b= 0.43 nm, c= 1.12 nm, PDF: 01-085-1324).

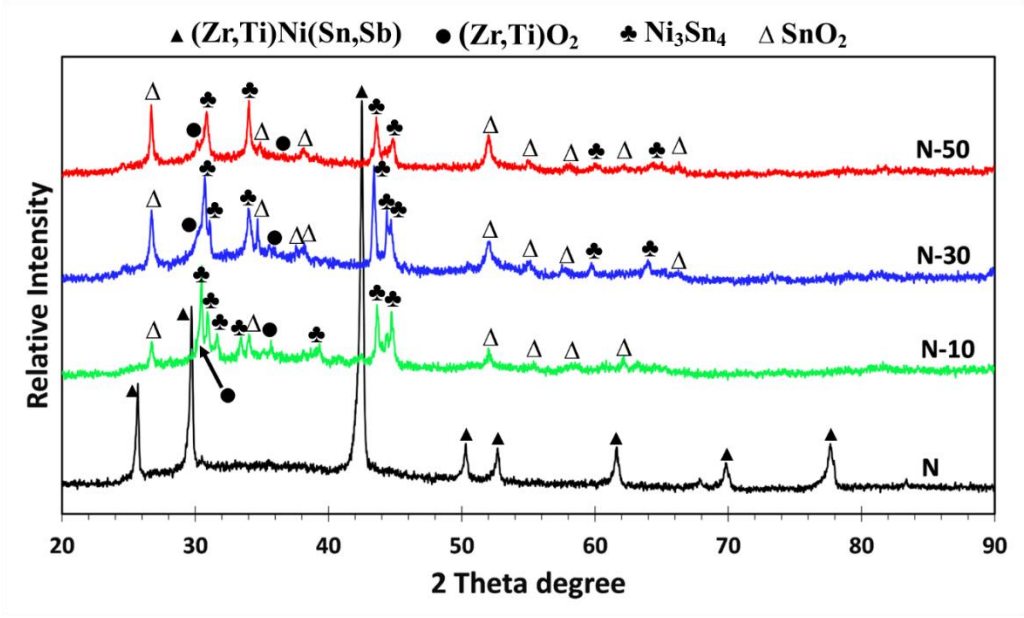


**a**

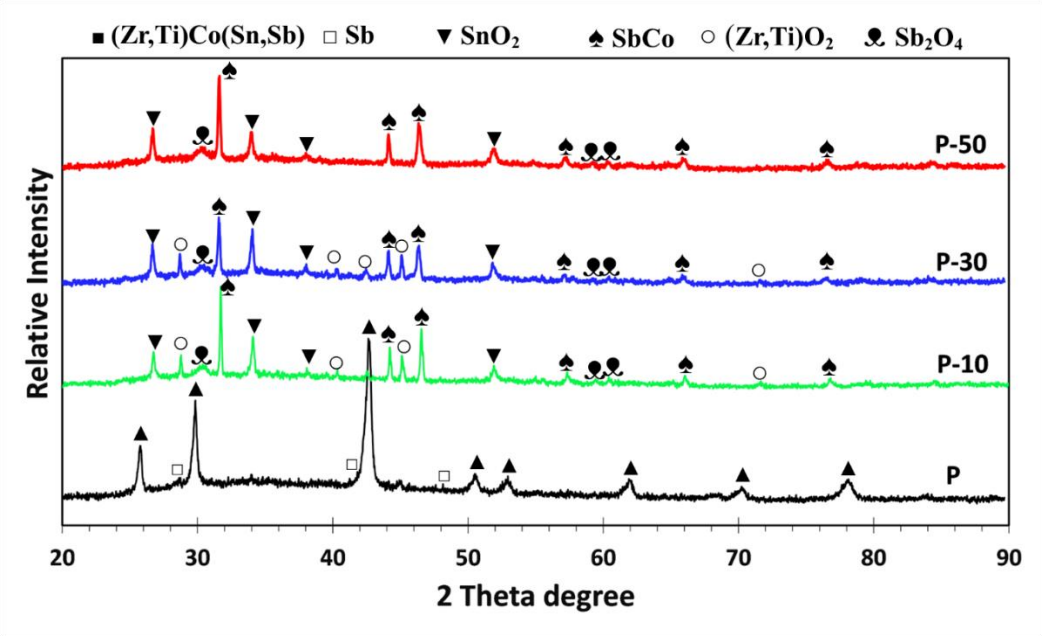


**b**

Figure 4.3. XRD patterns of (a) N-10, N-30 and N-50 samples compared with the N sample, (b) P-10, P-30 and P-50 samples compared with the P sample.

After cyclic oxidation tests, substantial alterations of phase constituents on the surface of N-type and P-type materials were observed. As for N-type samples, crystallographic reflections corresponding to $SnO_2$ (tetragonal, a= b= 0.473 nm, c= 0.318 nm, PDF: 01-070-4177), $Ni_3Sn_4$, (monoclinic, a= 1.22 nm, b= 0.405 nm, c= 0.521 nm, PDF: 03-065-4310) and $(Zr,Ti)O_2$ (orthorhombic, a= 0.504 nm, b= 0.509 nm, c= 0.525 nm, PDF: 00-037-1413) phases were identified for all cyclic tested samples. However, the intensity of the diffraction peaks of $SnO_2$ and $Ni_3Sn_4$ phases exhibited high intensity when the number of oxidation cycles increased. Meanwhile, the $(Zr,Ti)O_2$ phase shows low intensity for all cyclic oxidation tested samples.

The XRD patterns of P-type material after cyclic oxidation tests are presented in Figure 4.3b. For all cyclic oxidation tested samples, four phases can be identified corresponding to $SnO_2$ (tetragonal, a= b= 0.473 nm, c= 0.318 nm, PDF: 01-077-0447), SbCo (hexagonal, a= b= 0.39 nm, c= 0.517 nm, PDF: 96-154-1040), $(Zr,Ti)O_2$ (monoclinic, a= 0.507, b= 0.521 nm, c= 0.519 nm, PDF: 96-210-8456), and $Sb_2O_4$ (orthorhombic, a= 0.543 nm, b= 0.481 nm, c= 1.176 nm, PDF: 01-071-0564), which are markedly different from the original phase composition of P-type material. Notably, the diffraction peaks attributed to SbCo and $SnO_2$ exhibited relatively strong intensities, while reflections corresponding to the $(Zr,Ti)O_2$ phase were very weak for the P-50 sample (Figure 4.3b).

### *4.4.3 Effect of cyclic testing on surface morphology*

Backscattering electron images (BEI) of N and P samples, and SEM images of N-10, N-50, P-10 and P-50 samples are given in Figure 4.4. The surfaces of the N and P samples (Figure 4.4a&d) are greyish with a few light and dark small patches. EDX chemical composition analysis in the dark regions (Figure 4.4a) of the N sample identifies 16.3% Ti, 28.8% Ni, 21.7% Zr, 33.1% Sn and 0.1% Sb (see Table 4.3). In the light regions (Figure 4.4a), EDX analysis revealed a high concentration of Ni (40.1 at.%) and Sn (50.4 at.%) (Table 4.3).

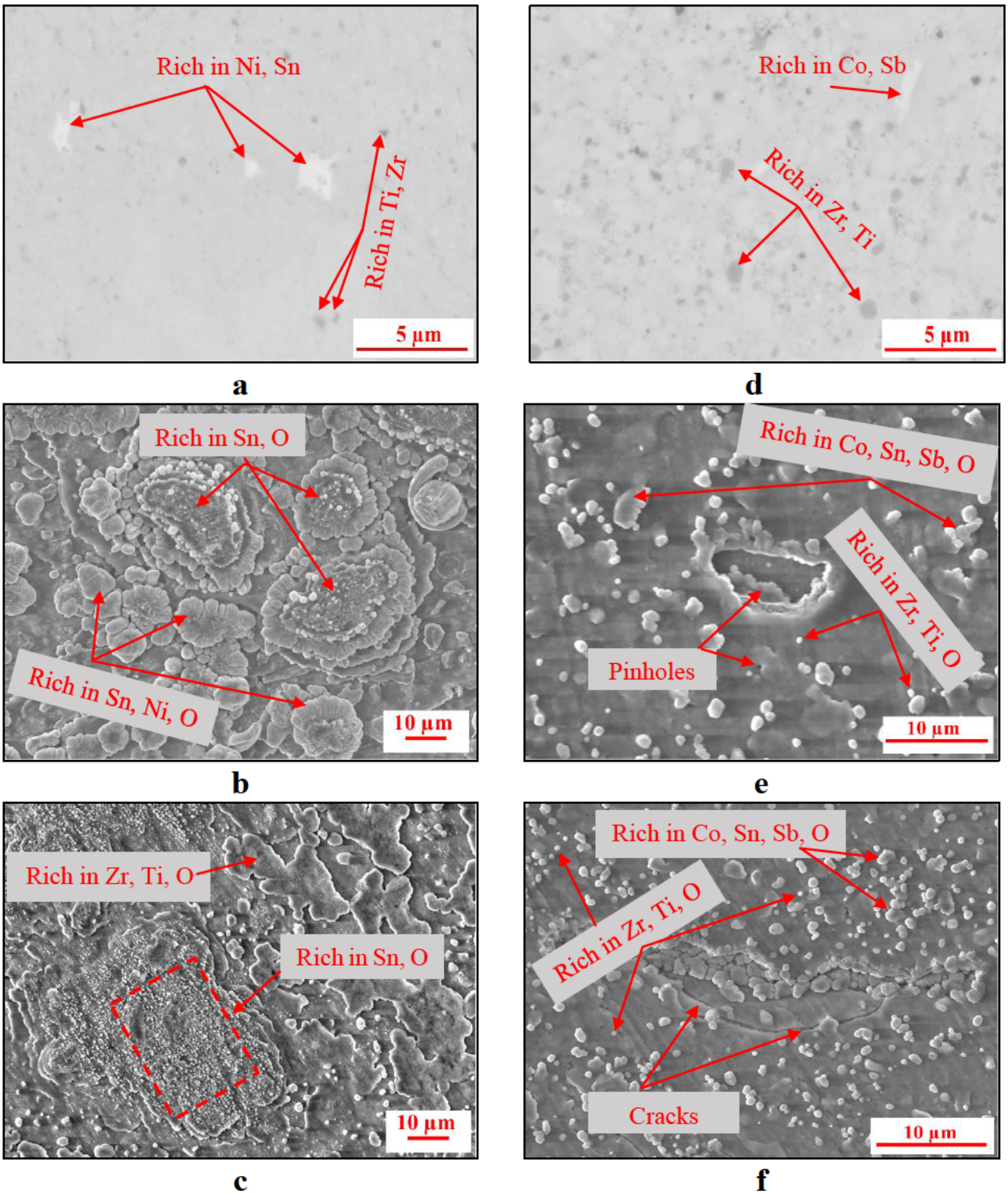


Figure 4.4. Backscattered electron images of the (a) as-produced N compared with SEM images of (b) N-10 and (c) N-50; and (d) as-produced P samples compared with SEM images of (e) P-10 and (f) P-50.

Upon comparing the chemical composition of the dark and bright patches in the N sample (Table 4.1), it can be seen that high Zr and Ti contents led to the change of colour from light grey to dark grey, while regions rich in Ni and Sn appeared bright. A similar feature was observed in the P-type sample (Figure 4.4d) where Zr-rich regions are in dark grey contrast, while the white contrasted patches are rich in Co and Sb (Table 4.3).

After 10 cycles of oxidation, some cauliflower-like patterns were observed on the surface of the N sample without noticeable delamination features (Figure 4.4b). When the oxidation cycles increased, both large areas with fine particles and jigsaw-like patches were observed, and a typical surface morphology of the N-50 sample is shown in Figure 4.4c. EDX surface composition analysis revealed enrichment of Sn, Ni and O from the area with fine particles and high content of Zr, Ti and O from the jigsaw-like patches, as denoted in Figure 4.4c. Limited delamination of the oxides was observed from the surface of the N-50 sample.

Multiple microparticles rich in elements of Co, Sn and Sb and small cracks/delamination were observed on the cyclic oxidation-tested P-type samples (Figure 4.4e&f). When increasing the cycles of the oxidation testing, the particles on the surface and the cracks and delamination of the surface oxide layer increased as shown in Figure 4.4e&f for P-10 and P-50 samples respectively.

Table 4.3. EDS analyses (at. %) of the dark and bright points on the surface of the as-received N and P samples.

| Samples | | Ti | Ni | Co | Zr | Sn | Sb |
|---|---|---|---|---|---|---|---|
| N | Bright Point | 4.3 | 40.1 | - | 4.4 | 50.4 | - |
| | Dark Point | 16.3 | 28.8 | - | 21.7 | 33.1 | 0.1 |
| P | Bright Point | 10.1 | - | 29.3 | 24.7 | 4.9 | 31.0 |
| | Dark Point | 11.2 | - | 18.4 | 44.8 | 4.2 | 21.3 |

### *4.4.4 Cross-sectional layer structure after cyclic oxidation testing*

The cross-sectional layer structures of cyclic-oxidation tested N-type and P-type samples were observed under backscattering electron image mode (Figure 4.5). A multilayered structure was formed on all cyclic oxidation tested samples with the thickness of the multilayers and the cracks increased with the number of cycles. It can be seen that the individual layers within the multilayers showed distinct grey and white contrasts, indicating element segregation and selective oxidation during the cyclic oxidation testing of the material. For the N-10 sample, the multilayer structure consists of thick repeated layers on the top surface as well as thinner alternated layers below the thick layers, as can be seen in Figure 4.5a. The thickness of the multilayered oxide structure of the N-10 sample is greater than that of the P-10 sample (Figure 4.5a&b), which means that the N-type material is oxidised faster than the P-type, leading to more increase in the mass gain (see Figure 4.2). Significant structural defects were observed, the extent of which increased with the oxidation cycles. Severe large cracks were observed near the interface between the matrix and the surface layer for the N-50 sample (Figure 4.5c), while for the P-50 sample, the cracks developed along the interfaces between multilayers (Figure 4.5d). As evidenced from the surface of the oxide structure, deep surface oxide spallation occurred especially for the N-50 sample (Figure 4.4e), which reduced the thickness of the remained oxide layer observed on the cross section. Significant structural defects were observed, the extent of which increased with the oxidation cycles. Severe large cracks were observed near the interface between the matrix and the surface layer for the N-50 sample (Figure 4.5c), while for the P-50 sample, the cracks developed along the interfaces between multilayers (Figure 4.5d).

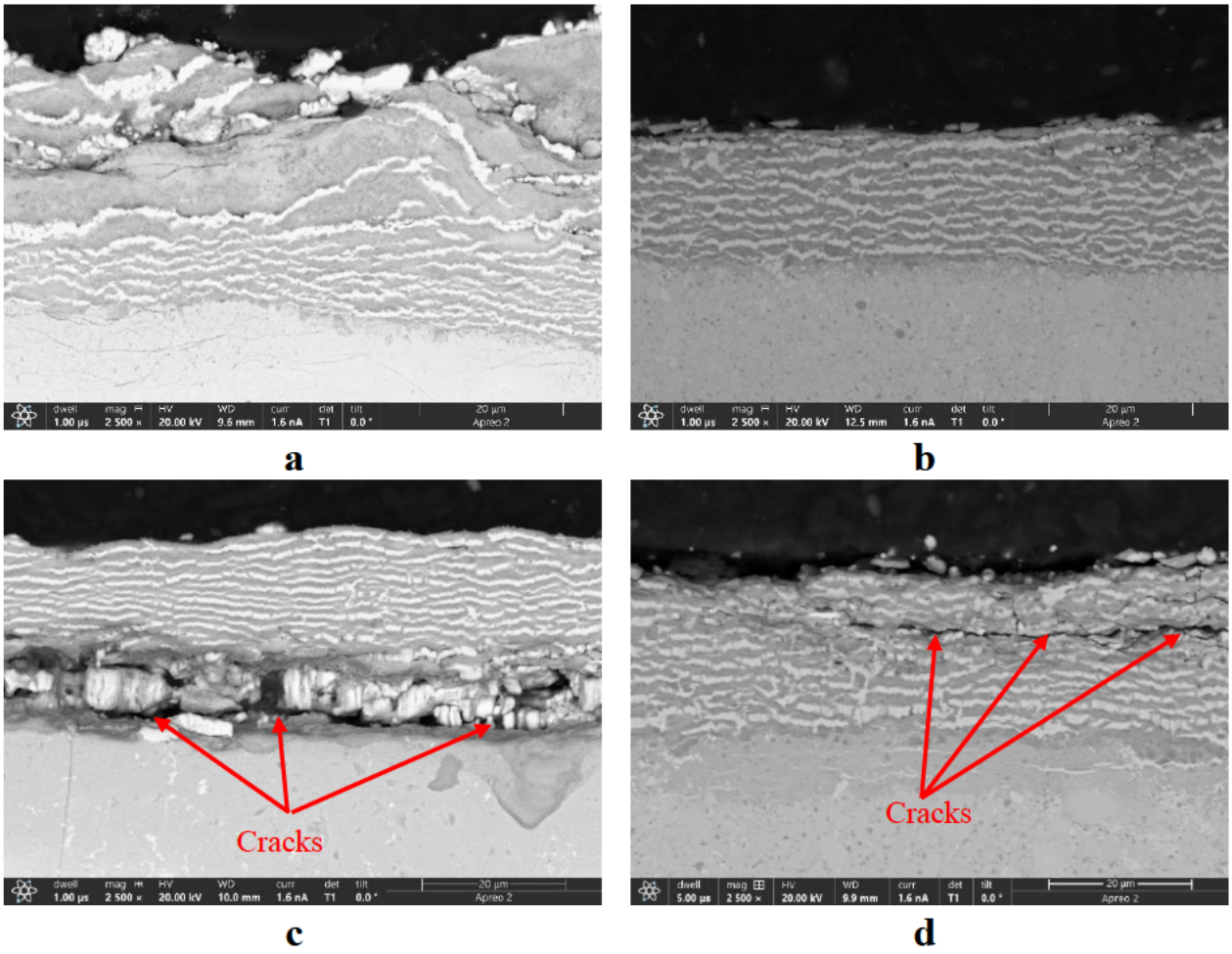


Figure 4.5. Cross-sectional backscattering electron images of (a) N-10 sample, (b) P-10 sample, (c) N-50 sample, and (d) P-50 sample.

The cross-sectional EDS line-scan analysis (Figure 4.6) across the multilayered structure provides element distribution through each thin layer for N-10 and P-10 samples. It is observed that Zr, Ti together with oxygen exhibit prominently heightened signals in the grey layers of the N-10 sample (dashed line in Figure 4.6a), whereas Ni, Sn, and Sb show high intensity in the white layers (solid line in Figure 4.6a). For the P-10 sample, Zr, Ti and oxygen have high concentrations in the grey layer (dashed line in Figure 4.6b), and Co and Sb display high intensity in the white layers (solid line in Figure 4.6b). However, Sn content shows a small fluctuation within grey and white layers for the P-10 sample, indicating moderate segregation of the element during the cyclic oxidation.

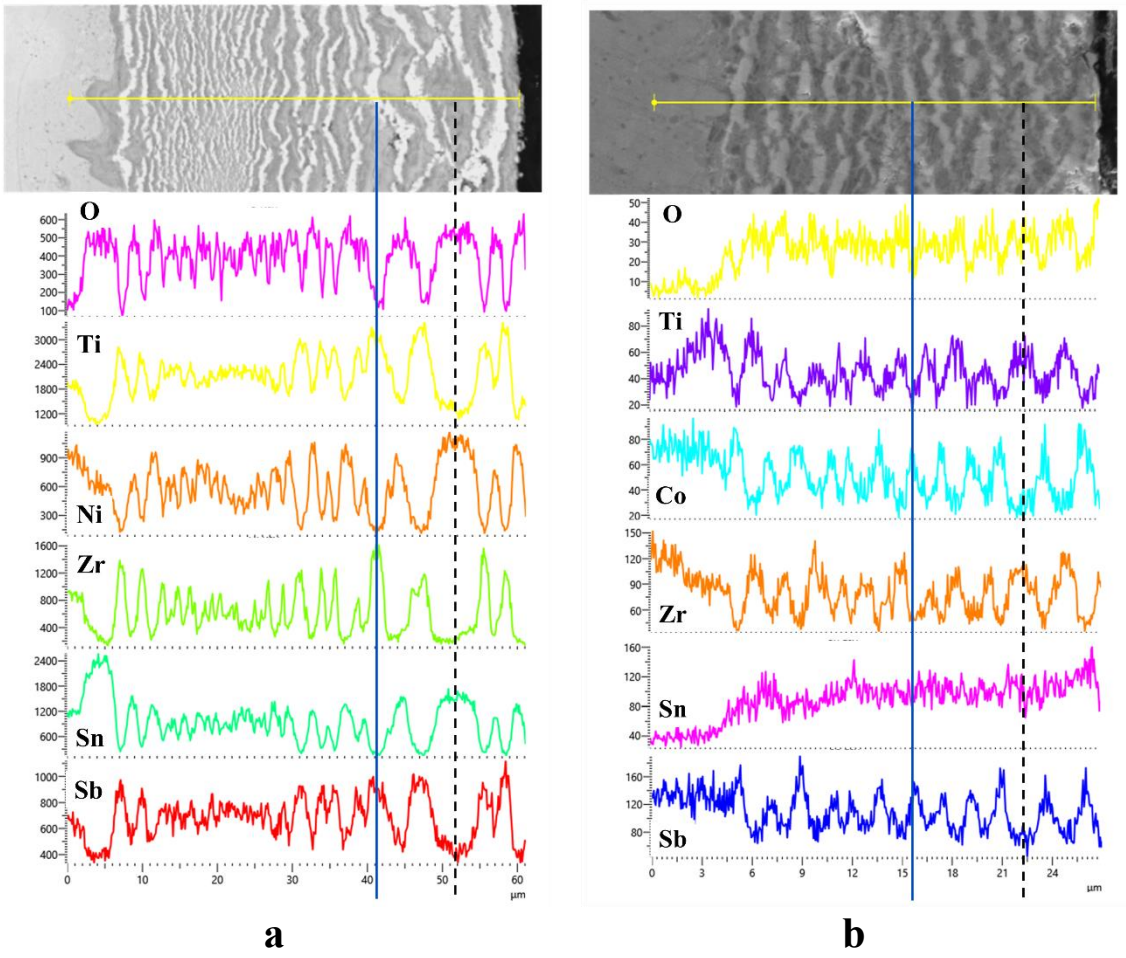


Figure 4.6. EDS line scan analyses of (a) N-10, and (b) P-10 samples.

## 4.5 Discussion

### *4.5.1 Cyclic oxidation of N-type material*

SEM images in Figure 4.4a&d show the overall single-phase contrast of the matrix for both as-received N-type and P-type materials although small patches of element segregation are presented (Table 4.3). XRD pattern analysis confirmed the Hf-free half-Heusler single phase of (Zr,Ti)Ni(Sn,Sb) for the N-type and (Zr,Ti)Co(Sn,Sb) for the P-type materials. As can be seen from Figure 4.4, the surface morphology of the samples changed completely after the cyclic oxidation tests with different features for the N-type and P-type materials. The surface of the N sample presents cauliflower-like oxide features after 10 cycles of oxidation tests. EDX analysis revealed a high content of Sn in these areas, indicating that these cauliflower-like oxides were

initiated from the original Sn(Ni) rich areas, as denoted in Figure 4.4a, where oxygen reacted with Sn to form $SnO_2$.

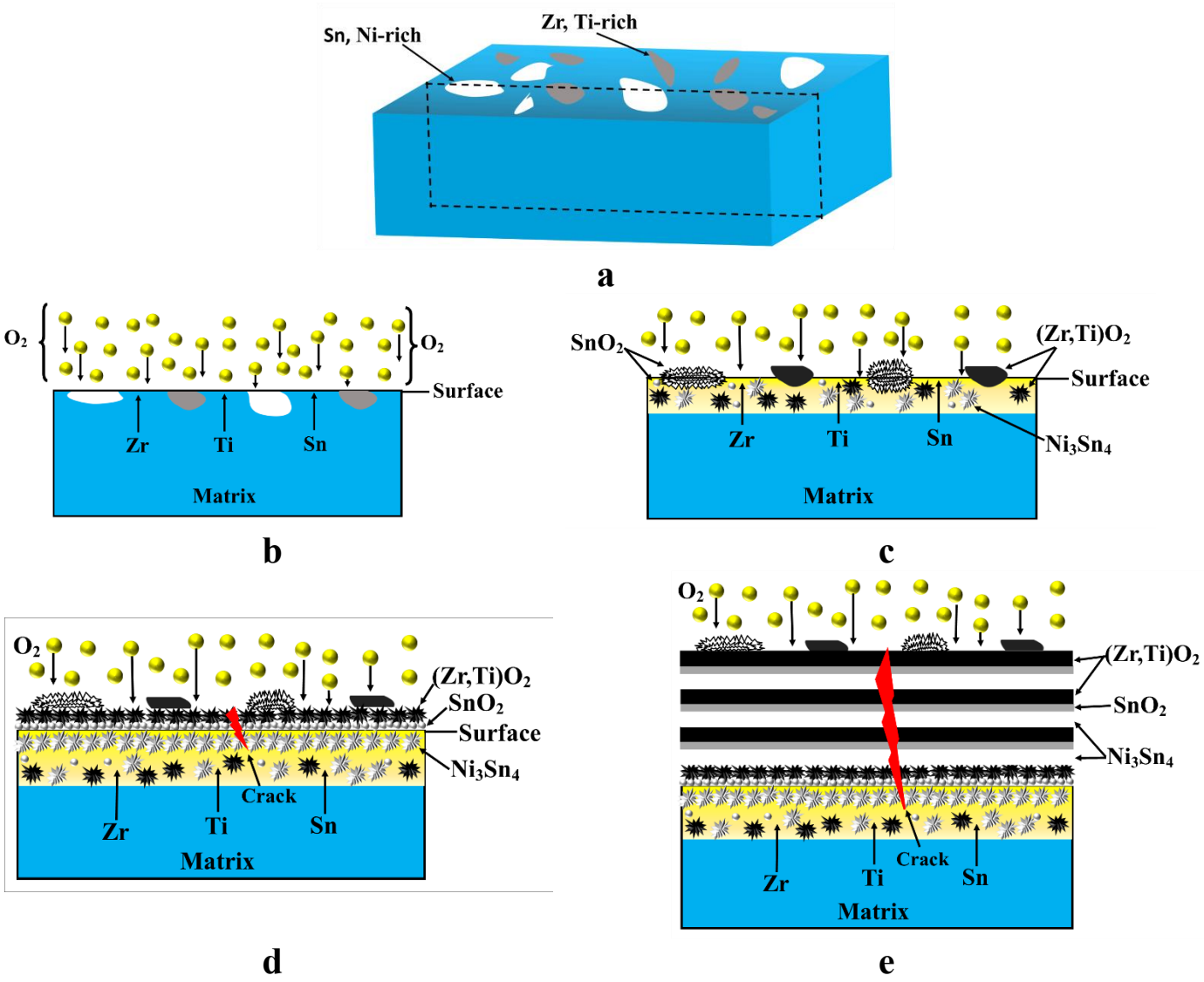


Figure 4.7. Schematics of the formation of surface multilayered surface structure, (a) pre-oxidation of N-type sample, (b) inward diffusion of oxygen, (c) formation of $SnO_2$, $(Zr,Ti)O_2$ and $Ni_3Sn_4$ grains, (d) outward diffusion of Zr, Ti and Sn, starting the formation of $(Zr,Ti)O_2$, $SnO_2$ and $Ni_3Sn_4$ layers, (d) formation of multilayered surface structures.

After long cycle oxidation, the cauliflower-like $SnO_2$ oxide areas merged into flat large patches decorated with nano-particles; the other surface areas formed jigsaw-like $(Zr,Ti)O_2$ (Figure 4.4c), which were initiated from the original (Zr,Ti)-rich particles, as denoted in Figure 4.4a. SEM images (Figure 4.5a&c) and EDX line scan analysis (Figure 4.6a) reveal that the contents

of the elements (Zr, Ti, Ni, Sn, Sb and O) fluctuate periodically along the oxide case corresponding to the multilayered structure. The XRD results (Figure 4.3a) confirmed the oxidation products of $(Zr,Ti)O_2$, $SnO_2$ and $Ni_3Sn_4$ compounds. This indicates that the cyclic oxidation between room temperature and 500°C has led to the formation of alternately repeated layers of oxides ($(Zr,Ti)O_2 + SnO_2$) and $Ni_3Sn_4$.

Formation of this alternated multilayer structure can be considered as a competitive process between internal oxidation and external oxidation as schematically illustrated in Figure 4.7. At the beginning of oxidation, oxygen diffused inward into the surface of the TE material. Those small areas with high concentrations of Sn, (Zr,Ti) reacted with oxygen to form $SnO_2$ and $(Zr,Ti)O_2$ (Figure 4.7b&c) featured as cauliflower-like and jigsaw-shaped patches, respectively (Figure 4.4a&b). In the meantime, oxygen further diffused into the subsurface of (Zr,Ti)Ni(Sn,Sb), where those elements with low enthalpies of formation oxides, such as Zr, Ti and Sn (Figure 4.8, [89, 199]) would form $(Zr,Ti)O_2$ and $SnO_2$. While those unoxidised Ni and Sn remain in-situ forming $Ni_3Sn_4$, and the residual Sn diffused to the outside surface driven by the reduced surface energy [200] where Sn is oxidised to form $SnO_2$ (Figure 4.7c). Detailed information on the oxidation of half-Heusler NiTiSn multi-phased material with the formation of the $Ni_3Sn_4$ and oxide phases determined by the calculated ternary phase diagram can be found in reference [201].

Following that, the low enthalpy oxide forming elements, such as Zr, Ti and Sn diffused outward to the interface between the formed oxide layer and the matrix to form $(Zr,Ti)O_2$ and $SnO_2$, as schematically shown in Figure 4.7d, while unmigrated Ni and part of Sn elements formed additional layer of $Ni_3Sn_4$ intermetallic compound beneath the oxide layer with the remaining Sn diffusing to the top of the $Ni_3Sn_4$ layer formed.

In the literature, a similar multilayer structure was observed for the P-type skutterudite $Ce_{0.9}Fe_3CoSb_{12}$ [202]. An interesting phenomenon called "pesting"-like oxidation explained the formation mechanism of multilayer structure on the material surface after 24-hour exposure to air at 800 K. It was said that the severe oxide layers formed on the surface during the oxidation were periodically peeled off, leading to frequent oxidation of the fresh bulk material, which is still exposed to high concentration oxygen atmosphere. The reputation of oxidation & peeling off led to the formation of the multilayer structure. Clearly, the mechanisms for the formation of multilayer oxide structures depend highly on the materials (skutterudite in [202] vs half-Heusler in this study) and the oxidation testing methods (isothermal in [202] and cyclic in this study).

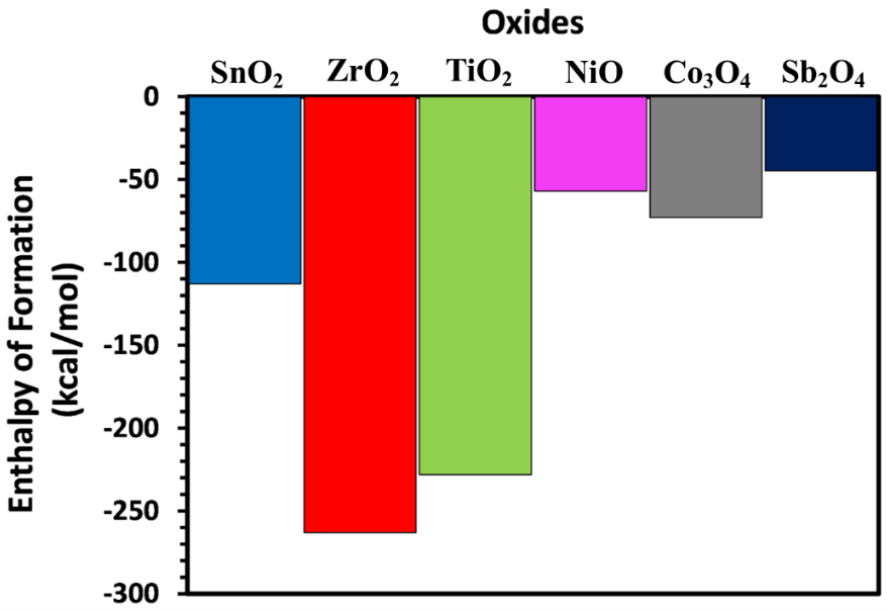


Figure 4.8. Enthalpy of formation of potential oxide products.

Due to the large difference in coefficient of thermal expansion (CTE) between $ZrO_2$ (~$26.8\times10^{-6}$ $K^{-1}$), $SnO_2$ ($11.7\times10^{-6}$ $K^{-1}$) and $Ni_3Sn_4$ ($12.2\times10^{-6}$ $K^{-1}$) [203-205], larger internal stress resulted in the formation of pinholes and cracks in the oxide layer as evidenced in Figure 4.5c and schematically shown in Figure 4.7d&e, which provided rapid paths for oxygen diffusion to the

interface between the oxide layer and the matrix, and the process of forming $(Zr,Ti)O_2$ + $SnO_2$ + $Ni_3Sn_4$ layer structure is repeated thus resulting in the formation of oxides/$Ni_3Sn_4$ alternative layers.

### *4.5.2 Cyclic oxidation of P-type material*

Although the alternating layer feature formed within the cross-sectional oxide case during cyclic oxidation on P-type (Zr,Ti)Co(Sn,Sb) (Figure 4.5b&d) looks similar to that formed on the N-type (Zr,Ti)Ni(Sn,Sb) (Figure 4.5a&c), the surface morphology (Figure 4.4) and mass gain (Figure 4.2) of the P-type (Zr,Ti)Co(Sn,Sb) are significantly different. Instead of the abnormal surface morphology change for the oxidised N-type samples, the P-type samples oxidised under the same conditions only showed small particles on a relatively smooth/flat surface (Figure 4.4e&f) with very limited pinholes and mild cracks.

The mass gain of the P-type sample was 2.1 $mg/cm^2$ after 50 cycles, only one-third of the mass gain of the N-type samples when tested under the same cyclic oxidation conditions. It is also noticed that the mass mainly gained within the initial 20 cycles, and then it kept nearly constant when further increasing the oxidation cycles. The parabolic rate constants $k_p$ calculated according to the parabolic kinetics, $(\Delta m/A)^2 = k_p \times t$, are 0.006165 $mg^2cm^{-4}s^{-1}$ and 0.000109 $mg^2cm^{-4}s^{-1}$ for N and P-type samples, respectively, with the former is more than 56.7 times that of the latter.

The smoother surface (Figure 4.4e&f) and less mass gain (Figure 4.2) indicate the better oxidation resistance of the P-type materials than the N-type ones, which is in line with the calculated much smaller parabolic rate constants. This significantly reduced parabolic rate constants and hence slackened oxidation process could be mainly attributed to the composition difference between the P-type and N-type materials. It can be seen from Table 4.1 that the P-type and N-type TE materials contain similar quantities of Zr and Ti elements, and similarly,

$(Zr,Ti)O_2$ is formed in both N-type and T-type materials as identified by XRD analysis (Figure 4.3).

Although both the N-type and P-type materials contain Sn, the P-type contains much less Sn (10.7 at.%) as compared with that (32.3 at.%) of the N-type. Firstly, the reduction of Sn in the P-type TE material could improve the oxidation resistance of the material. As can be seen from Figure 4.4b&c, Sn initially segregated patches in the N-type material resulted in the formation of cauliflower-like tin oxides after 10 cycles and a large plateau with nano-crystalline tin oxides after 50 cycles of oxidation. The spallation of those features due to large difference in thermal expansion coefficient induced stress concentration increased the exposure surface areas to oxygen leading to fast oxidation. On the other hand, significantly reduced Sn content in the matrix should have helped to reduce the stress concentration, oxide spallation and hence oxidation of the P-type material.

Secondly, the Ni and reduced Sn in the P-type material are replaced by Co and Sb, respectively. The thermodynamic data shown in Figure 4.8 also indicates that the enthalpy of formation $\Delta H$ of $SnO_2$ is more negative (-110 kcal/mol) than that for $Co_3O_4$ (-73 kcal/mol) and $Sb_2O_4$ (-45 kcal/mol). Therefore, the replaced Ni and Sn by Co and Sb, respectively, should have further contributed to the lower oxidation of the P-type material [89, 206]. It can be seen that the Sb content is significantly increased from <1.0 at. %) for the N-type material to 25.7 at. % in the P-type material. Accordingly, peaks of $Sb_2O_4$ are identified from the oxidation-tested P-type material. The enthalpy of formation $\Delta H$ of $Sb_2O_4$ is much less negative than all oxides as shown in Figure 4.8 especially compared with that for $ZrO_2$ and $TiO_2$. Hence, this is reasonable to attribute the reduced oxidation rate of the P-type material as compared with the N-type material to the significantly high Sb content in the P-type material. Indeed, $Sb_2O_4$ has been used as a flame retardant in engineering plastics due to its stability in high temperature [207].

Thirdly, it is also reported that for the P-type TE material, the formation of $Co_3O_4$ oxide is exothermic [69], or entropy reduction reactions, the calculated $\Delta G$ changes from negative to positive with decreasing oxygen content [69], which was the case just beneath the firstly formed (Zr,Ti) oxides, such that the oxidation of Co was suppressed.

Having explained the slackened oxidation of the P-type TE material, the procedure for forming alternated layers in the surface oxide case on P-type material could be proposed as follows:

1) Inward diffused oxygen reacted with the (Zr,Ti)-rich patches formed small $(Zr,Ti)O_2$ particles, while those patches with high content of Sb and Sn reacted with oxygen formed a few $Sb_2O_4$ and $SnO_2$ particles, see Figure 4.4.
2) The remaining procedures would be similar to that for the formation of the alternated layer in N-type by replacing the Ni with Co, reducing Sn and increasing Sb, such that the alternated layers are $(Zr,Ti)O_2$ + $SnO_2$ (very thin) + $Sb_2O_4$ + CoSb.

## 4.6 Conclusions

In this study, the oxidation behaviour of the Hf-free N-type (Zr,Ti)Ni(Sn,Sb) and P-type (Zr,Ti)Co(Sn,Sb) thermoelectric materials produced by mechanical alloying and plasma sintering at 800°C were investigated by cyclic oxidation between room temperature and 500°C for up to 50 cycles. Based on the experimental findings, the following conclusions can be drawn:

- The surfaces of both N-type (Zr,Ti)Ni(Sn,Sb) and P-type (Zr,Ti)Co(Sn,Sb) materials are entirely oxidised after the cyclic oxidation testing, leading to a significant change in the surface morphologies.
- The oxidation of both N-type and P-type materials under cyclic oxidation conditions follows parabolic oxidation kinetics. However, the mass gain of the N-type increased

much faster compared to that of the P-type with the parabolic rate constants being 0.006165 $mg^2cm^{-4}s^{-1}$ and 0.000109 $mg^2cm^{-4}s^{-1}$ for N and P-type materials, separately.

- An alternated multilayer structure was formed on the cross-sections of both N-type and P-type materials, which highly suffered from aggressive oxidation. It is believed that such severe oxidation-induced microstructural changes would negatively affect the thermoelectric performance of these materials, which are constantly subjected to temperature differential.

The findings from the present study suggest in order to improve the thermal stability of N-type and P-type half-Heusler materials with favourable thermoelectric performance, it is necessary to protect the TE materials against oxidation by developing advanced surface coatings such as the CrSi coating developed recently in our group. Very promising oxidation protection results are obtained, which will be published in another paper.

# Chapter 5 Developing advanced CrSi coatings for combatting surface degradation of n-type (Zr,Ti)Ni(Sn,Sb) and p-type (Zr,Ti)Co(Sn,Sb) half-Heusler thermoelectric materials

* This chapter has been published in the Journal of Materials Research and Technology.

**[1]Gurtaran, M.,** [1]Zhang, Z., [1]Li, X., & [1]Dong, H. (2024). Developing Advanced CrSi Coatings for Combatting Surface Degradation of N-type (Zr, Ti) Ni (Sn, Sb) and P-type (Zr, Ti) Co (Sn, Sb) Half Heusler Thermoelectric Materials, Journal of Materials Research and Technology, 32, 3288-3301. https://doi.org/10.1016/j.jmrt.2024.08.169

1- School of Metallurgy and Materials, University of Birmingham, Birmingham, UK

**Acknowledge of Collaborative Work:**

**Mikdat Gurtaran:** Writing-Original draft, Methodology, Validation, Investigation; Zhenxue Zhang: Investigation; Xiaoying Li: Writing – Review & Editing, Validation, Conceptualization; Hanshan Dong: Supervision, Funding acquisition.

## 5.1 Abstract

In this study, advanced oxidation-protective CrSi coatings were developed and deposited on N-type (Zr,Ti)Ni(Sn,Sb) and P-type (Zr,Ti)Co(Sn,Sb) thermoelectric (TE) materials using an environmentally friendly closed field unbalanced magnetron sputtering PVD system. The oxidation behaviour of the CrSi-coated and uncoated samples was evaluated through static oxidation tests at 500℃ and 600℃ for 10h and 50 h, respectively. In addition, the samples were exposed to cyclic oxidation tests between 25℃ and 500℃ for 10, 30 and 50 cycles, with each cycle consisting of 1h of oxidation at 500℃, to examine the coating ability to withstand thermal shock, which is involved in the service of TE devices. The surface morphology, cross-section layer structure, elemental distribution and phase constitution were analysed using scanning electron microscopy (SEM), energy dispersive spectroscopy (EDX) and X-ray diffraction (XRD). The mass gain after the oxidation tests was measured and calculated for each sample to study the oxidation kinetics. The uncoated samples exhibited a considerable amount of oxidation, leading to change in the surface morphologies, and the formation of alternated layers including oxide products ($Zr(Ti)O_2$, $SnO_2$) and $Ni_3Sn_4$ compound for the N-type and ($Zr(Ti)O_2$, $SnO_2$, $Sb_2O_4$) and CoSb compound for the P-type material, after static and cyclic oxidation tests. The experimental work in this study has, for the first time, demonstrated that the CrSi coatings developed with very high thermal stability and oxidation resistance can effectively protect both the N-type and P-type materials from oxidation and sublimation even during cyclic oxidation tests. The strong affinity of Cr and Si to oxygen can trap oxygen, retard its inward diffusion and thus protect the TE material substrate from oxidation. This finding could pave the way towards the further development of long-life high-performance TE generators and devices, thus contributing to the net zero target.

## 5.2 Introduction

Thermoelectric (TE) devices that produce electricity from waste heat have become of great importance in recent years for green energy harvesting thus contributing to achieving the net-zero target [208, 209]. To this end, high-performance TE materials and modules with a high TE power factor have been developed as one of the sources of clean energy production methods [78, 210]. Many thermoelectric materials are being explored for power generation applications, such as GeTe [172], $Bi_2Te_3$ [173], PbTe [56, 174], and half-Heusler compounds [175]. Although researchers are pursuing TE materials with high figure of merit (zT) [86, 120, 171], how to maintain the high-performance over a long service period has emerged as a major challenge for the successful long-term application of TE devices [120, 208, 211]. TE materials, which convert the heat (driven by temperature differences between the hot source and the cold side) directly into electrical energy, are inherently exposed to high-temperature and frequent temperature changes during their application. This will cause the degradation of the TE materials over time leading to a worsening of the TE efficiency of the TE materials [88]. The chemical stability and hence the resistance to surface degradation of TE materials are affected by two major issues. The first issue is the reaction of active TE materials with the oxygen in the air at high temperatures leading to severe oxidation and deterioration of TE performance. For instance, it has been reported that the output power of the MNiSn/MCoSb-based TE generator decreased by about 50% after 5 days of operation at a hot-side temperature of 823 K in air [193]. The second issue is the sublimation of high vapour pressure elements of Pb, Ge, Te, Sb, Sn, etc at high working temperatures. For example, high-entropy TE materials contain such elements as Sn [90, 212] and Te [99] that sublimate at even moderate temperatures and the composition changes can cause a decrease in the number of electron-charged particles and negative changes in electrical and thermal conductivity, such that the thermoelectric properties inevitably deteriorate.

Half-Heusler (HH) thermoelectric materials have become attractive among TE materials in recent years due to their high efficiency in waste heat conversion into electricity (i.e. high zT) at medium-to-high temperatures [46, 59, 213, 214]. Although their thermal stability is superior to PbTe and skutterudite, the interaction of HH TE materials with an oxygen-containing environment will induce severe oxidation [68, 201] and sublimation [215] as most HH TE materials still contain high vapour pressure elements such as Sb and Sn, resulting in reduced TE performance. Therefore, it is necessary to apply surface coatings to protect TE materials from surface oxidation and sublimation.

Great efforts have been made by many researchers in developing protective coatings for TE materials. For example, several types of coatings were researched to protect MgSi-based TE materials against oxidation such as silane-based amorphous [22], glass [161], silica [216], and/or hybrid coatings [167, 217]. Similar coatings were applied on other types of TE materials such as $CoSb_3$ [163, 218], skutterudites [21, 217] and BiTe-based [20, 219]. These coatings can meet the requirements for low thermal conductivity to prevent parasitic heat loss, low electrical conductivity to prevent short-circuiting and high thermal stability for oxidation protection and showed satisfactory oxidation protection in static or isothermal oxidation testing. However, there is limited information on the application of these oxidation-protective coatings on HH TE materials. It should also be pointed out that although these coatings showed a certain level of success in protecting TE materials from oxidation in static or isothermal oxidation tests, their effectiveness under cyclic oxidation conditions which are more relevant for application, to the best of our knowledge, has not been investigated. The mismatch of the coefficients of thermal expansion (CTE) between these coatings and the TE materials substrate would lead to stress concentration and coating spallation when subject to cyclic heating and cooling in service. Consequently, it is imperative to develop tailored surface coatings to protect half-Heusler TE

materials from surface degradation and high-temperature oxidation in particular under cyclic oxidation conditions, which formed the aim of this paper.

As known, chromium characteristically provides considerably good oxidation resistance at high temperatures [220, 221] thanks to the formation of stable chromium oxide films, but its insufficient mechanical properties at high temperatures are still a concern [222]. To address this limitation and provide desirable mechanical properties, it is suggested that adding a small amount of Si to the Cr structure may contribute to delaying oxidation [223, 224]. As reported by He et al. [225], the solid solution phase formed by Si in the CrSi coating can delay the oxidation of the coating. The oxidation performance was higher with more Si content, up to 15%, as it stabilises the CrSi coating at elevated temperatures up to 1160°C. Zhao et al. also reported that the hardness of the CrSi coating with a Si content of 11% (at.) is almost five times greater than that of the pure Cr coating, highlighting that the insufficient mechanical performance of the pure Cr coatings is enhanced by the addition of a small amount of Si into the Cr coatings. Godlewska et al. [226] deposited the Cr5Si layer on skutterudite TE materials and tested its protective performance against oxidation at 500℃ and 600℃ for 80 hours. They reported that the Cr5Si coating prevented Sn loss by sublimation and oxidation at 500℃, whereas the adhesion of the coating was not satisfactory at 600℃. In addition, in our earlier feasibility study [169], it was found that 4-7 at.% of Si in Cr coatings deposited on the stainless steel exhibited optimum oxidation protection up to 800℃. However, it is not clear if such Si-doped Cr coatings could be applicable to HH TE materials for oxidation protection under cyclic oxidation conditions, which is highly dependent on the bonding and CTE match between the CrSi coating and the HH TE materials.

In the present study, Cr coatings with the desired amount of Si were deposited on the N-type (Zr,Ti)Ni(Sn,Sb) and P-type (Zr,Ti)Co(Sn,Sb) TE materials using a closed-field unbalanced magnetron sputtering system. The CrSi-coated TE materials samples were both statically and

cyclically oxidised. The oxidation behaviour of the CrSi-coated TE materials was comprehensively investigated by analysing the mass gain, observing surface morphology and cross-sectional microstructure, and examining the change of the phase constitution. The current study aims to provide new sights into and thus advance scientific understanding of the protection of HH TE materials against oxidation at high temperatures by CrSi coatings under both static and cyclic oxidation conditions for the first time. Additionally, it may also offer guidance for the application of the CrSi coatings for other types of TE materials for oxidation protection.

## 5.3 Experimental

### *5.3.1 Materials and sample preparation*

The test samples provided by Matres Scrl (Italy) were produced by mechanical alloying through high-energy ball milling of metal powders of Zr, Ti, Ni, Co, Sn, and Sb in an inert environment followed by plasma sintering for 4 minutes at 800°C under a pressure of 500 kg/cm². The approximate dimension of the samples was 0.5×0.5×4.0 $cm^3$ and the chemical compositions of the fabricated products are given in Table 5.1. The test samples were ground with SiC papers up to 1200 grit and then subjected to ultrasonic cleaning with acetone and deionised water for ten minutes, respectively.

Table 5.1. The chemical composition of thermoelectric materials used in this study.

| Type | Materials | Elements (at. %) | | | | | |
|---|---|---|---|---|---|---|---|
| | | Ti | Ni | Co | Zr | Sn | Sb |
| N | (Zr,Ti)Ni(Sn,Sb) | 17.1 | 33.5 | 0 | 16.3 | 32.3 | <1.0 |
| P | (Zr,Ti)Co(Sn,Sb) | 16.4 | 0 | 29.1 | 18.1 | 10.7 | 25.7 |

### *5.3.2 CrSi coating deposition process*

The CrSi coatings were deposited on the N-type and P-type samples as well as on Si wafers (for coating characterisation) using an unbalanced closed-field magnetron sputtering system. Inside the chamber, Cr and Si cathode targets were placed opposite each other. The coating process was carried out in three steps. First, the sample surfaces were ion-cleaned for 15 min using a low current of 0.05 A (Si) and 0.2 A (Cr), under a bias potential of 200 V. Afterwards, the current applied to the Cr and Si targets gradually increased to 2A and 0.3A, respectively, while the bias potential was simultaneously reduced from 200 V to 40 V. In the final stage, CrSi was deposited in an argon atmosphere at a pressure of $13.33\times10^{-2}$ Pa for 70 minutes. To achieve the desired CrSi composition, a constant 2A current was applied to the Cr target, 0.3A current was applied to the Si target and the sample holder rotated at 5 rpm during the coating process. A temperature increment inside the deposition chamber (up to 100℃) due to ion bombardment was also observed throughout the deposition process.

### *5.3.3 Static and cyclic oxidation testing*

The TE samples were individually placed in a ceramic boat and statically oxidised in a muffle furnace at 500℃ for 10 hours and 600℃ for 50 hours, respectively. Before and after the static oxidation testing, the weight of the samples was measured using the Ohaus high-precision scale with a sensitivity of $10^{-4}$ g.

To simulate the realistic service conditions for TE generators, cyclic testing was designed to investigate the effect of cyclic heating and cooling on the bonding of the CrSi coating to the TE materials substrate. During the tests, the ceramic containers with the samples were placed in the same muffle furnace at 500℃ for 1 hour before they were removed from the furnace and cooled to room temperature within 15 minutes in the air. This process was repeated for 10, 30, and 50 cycles. After each cycle test, the samples were weighed using the same sensitive scale mentioned above.

### *5.3.4 Microstructure characterisation*

Microstructural investigation of the uncoated and as-coated CrSi samples before and after static and cyclic oxidation testing was carried out by examining surface and cross-sectional microstructures of the coatings using Jeol 7000 and Apreo2 scanning electron microscopies (Jeol-UK Ltd., Welwyn Garden City, UK and Thermofisher Scientific, Stafford, UK, respectively). The chemical composition and elemental distribution were also investigated by EDX analysis. Phase identification of the samples was made using a ProtoA XRD diffractometer employing a Cu-Kα source (λ = 1.540598 Å). The sample code and their corresponding processing parameters are given in Table 5.2. As the oxidation behaviour of the uncoated N-type (Zr,Ti)Ni(Sn,Sn) and P-type (Zr,Ti)Co(Sn,Sb) TE materials has been reported in an early paper [227], the shadowed sample codes for these uncoated samples subject to the same cyclic oxidation testing are included for comparison purpose.

Table 5.2. Sample codes and their corresponding processing parameters.

| **Oxidation State** | **Oxidation Temperature (°C)** | **Duration** | **Code for uncoated samples** | | **Code for CrSi-coated samples** | |
|---|---|---|---|---|---|---|
| | | | **n-type** | **p-type** | **n-type** | **p-type** |
| As-received | - | - | N | P | NC | PC |
| Static Oxidation | 500 | 10 h | NO5 | PO5 | NCO5 | PCO5 |
| | 600 | 50 h | NO6 | PO6 | NCO6 | PCO6 |
| Cyclic Oxidation | 500 | 1h×10 cycles | NO5-10 | PO5-10 | NCO5-10 | PCO5-10 |
| | | 1h×30 cycles | NO5-30 | PO5-30 | NCO5-30 | PCO5-30 |
| | | 1h×50 cycles | NO5-50 | PO5-50 | NCO5-50 | PCO5-50 |

Note: these shadowed codes are included for comparison.

## 5.4 Results

### *5.4.1 Microstructure of CrSi coatings*

The microstructures of the CrSi coatings deposited were examined both on the surface and on the fractured cross-sections. As exemplified in Figure 5.1a&b, the coating is dense and uniform with a close-packed, columnar intergrowth structure. No pores or spallation were observed at the coating/substrate interface on the cross-section of the coatings. The thickness of the coating was approximately 2.63±0.2 μm. EDX analysis of the CrSi coatings revealed the coating's atomic Cr/Si ratio to be 92.46/7.54. XRD patterns taken from CrSi coating samples (Figure 5.2b) can be identified as Cr-body-centred cubic (bcc) phase (a=b=c= 0.28 nm, PDF: 00-006-0694) with a dominant (110) reflection indicating the preferred orientation of the columnar structure with a (110) perpendicular to the surface.

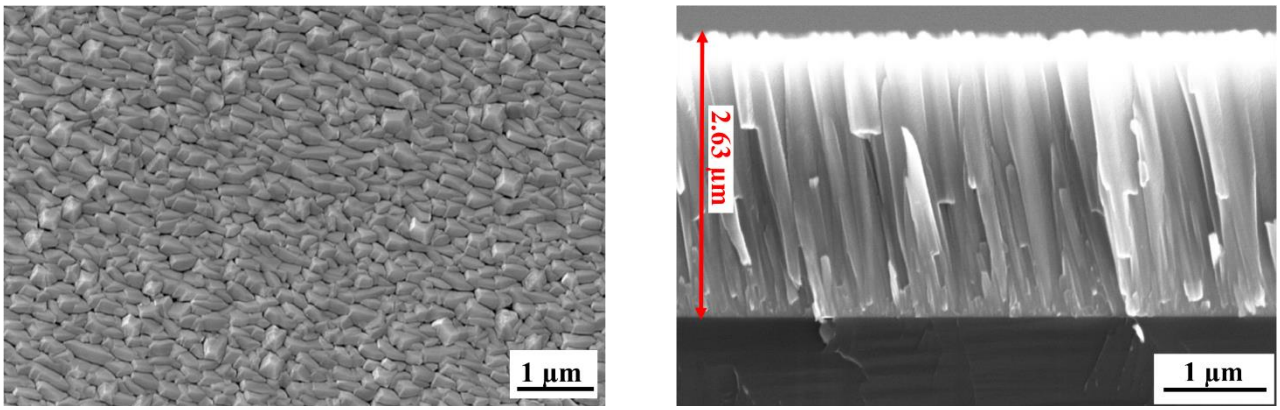


Figure 5.1. SEM images of CrSi coatings on Si wafer; (a) surface morphology, and (b) fractured cross-section layer structure.

### *5.4.2 CrSi coating protection against static oxidation of the P-type TE material*

*5.4.2.1 Phase identification of the oxide layers*

The XRD patterns of the P-type samples, both with and without CrSi coatings are presented in Figure 5.2. The as-produced P-type sample displayed main diffraction peaks corresponding to

the fcc structured (Zr,Ti)Co(Sn,Sb) half-Heusler phase (cubic, a=b=c= 0.59 nm, PDF: 03-065-0990). Additionally, a secondary phase of Sb (rhombohedral, a=b= 0.43 nm, c=1.12 nm, PDF: 01-085-1324) with relatively weak peaks was observed (Figure 5.2a).

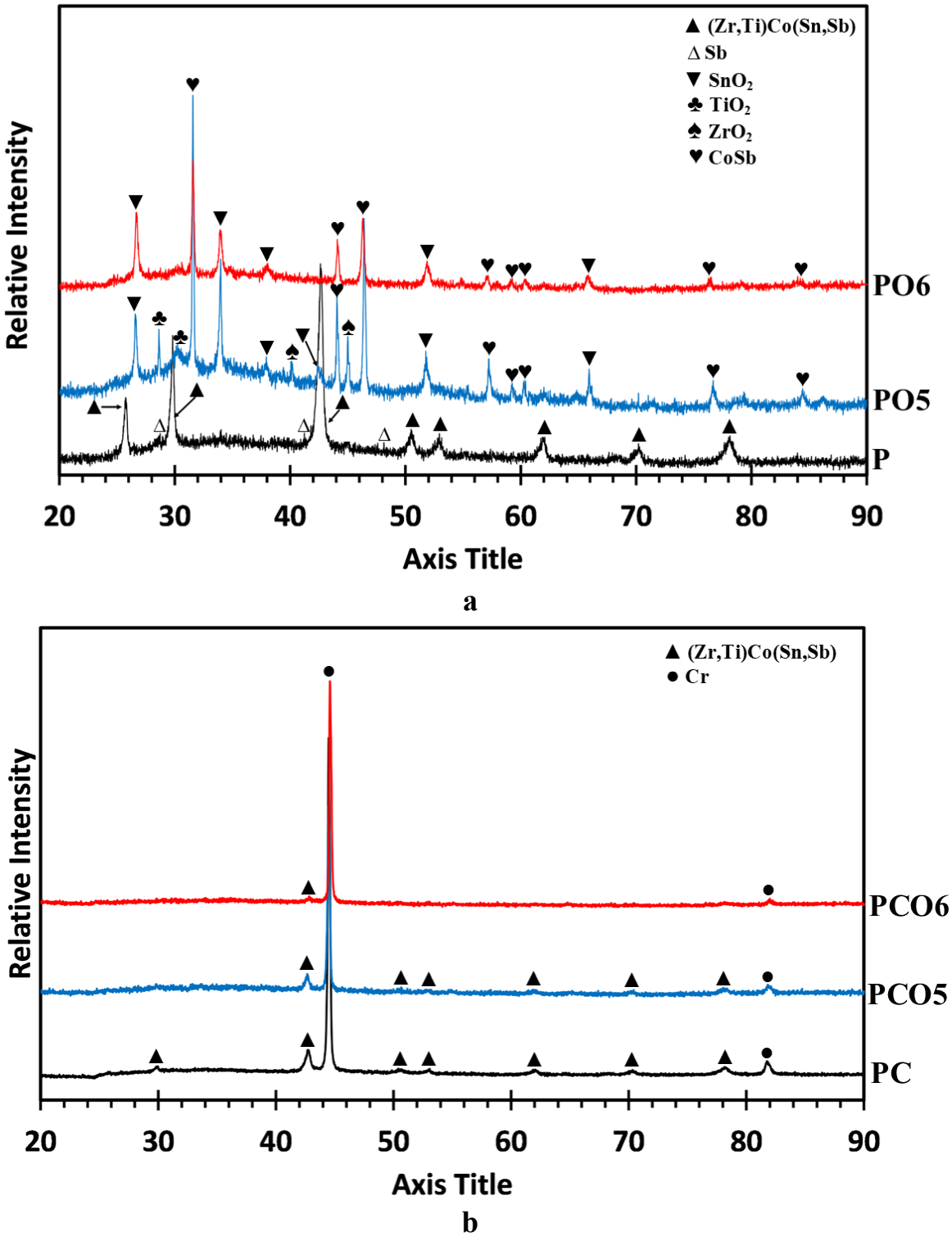


Figure 5.2. Typical XRD patterns of (a) P, PO5 and PO6 samples, and (b) PC, PCO5 and PCO6 samples

In contrast, after oxidation tests at 500℃ and 600°C for the PO5 and PO6 samples respectively, the diffraction peaks exhibited marked differences from that for the P-type sample. Specifically, for both PO5 and PO6 samples, high-intensity peaks corresponding to $SnO_2$ (tetragonal, a=b= 0.47 nm, c=0.31 and PDF: 01-072-1147) and CoSb (hexagonal, a=b= 0.39 nm, c=0.51 nm, and PDF: 03-065-0671) phases were identified. The diffraction peaks also revealed the presence of $ZrO_2$ (monoclinic, a=b= 0.52 nm, c= 0.53 and PDF: 01-072-597) and $TiO_2$ (monoclinic, a= 1.22 nm, b= 0.37 nm, c= 0.65 nm, and PDF: 00-046-1238) phases for the PO5 sample, whereas very weak peaks corresponding to these oxide phases were observed for the PO6 sample (Figure 5.2a), which was caused by the spallation of these oxide layers (see Section 3.2.2).

XRD patterns for the CrSi-coated P-type samples can be identified as the Cr phase (cubic, a=b=c= 0.28 nm, and PDF: 00-006-0694) with high intensity and the half-Heusler phase of (Zr,Ti)Co(Sn,Sb) coming from the substrate (Figure 5.2b). It is noteworthy that no appreciable phase alteration was observed for the CrSi-coated samples after the static oxidation testing at 500℃ and 600°C, indicating effective oxidation protection of the CrSi coating to the TE substrate materials. Very thin superficial chromium oxide film would be expected to form during the static oxidation tests, but the thickness of the oxide film is most probably too thin to be detected by the XRD method used.

*5.4.2.2 Surface morphology and layer structure*

The surface morphology and cross-sectional layer structure of the statically oxidised P-type material with and without CrSi coating were examined using SEM and EDX, and the obtained images and data are presented in Figure 5.3. It can be seen that the surface of the PO5 sample (Figure 5.3a) exhibits minor delamination with oxide particles formed on the surface. As the oxidation time and temperature increased to 600℃ for 50 hours, large oxide particles and deep cracks were observed, as evident in Figure 5.3c.

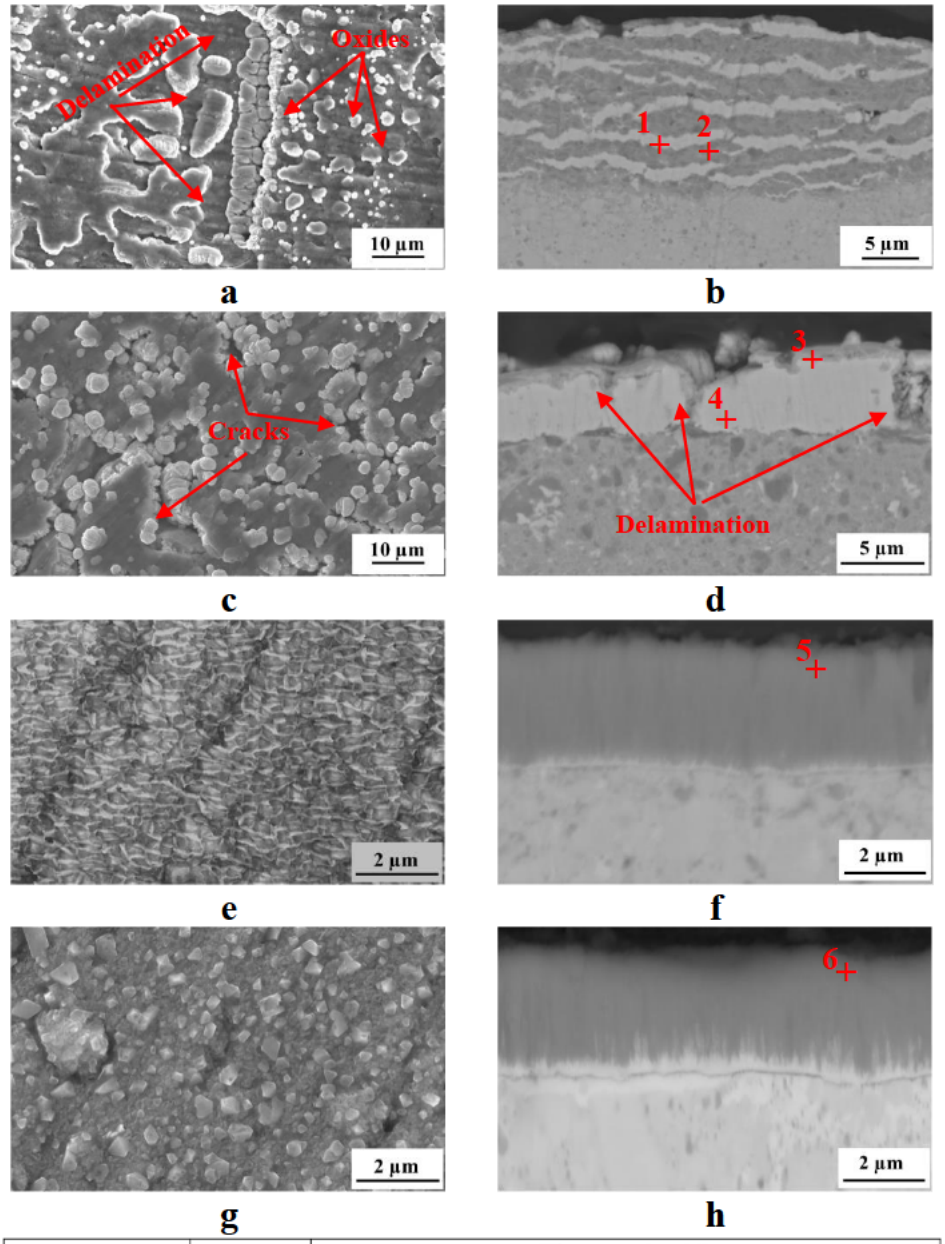


| Materials | Spectrum | Elements (at. %) | | | | | | | |
|---|---|---|---|---|---|---|---|---|---|
| | | Cr | Si | O | Ti | Co | Zr | Sn | Sb |
| PO5 | 1 | - | - | 35.3 | 12.4 | 6.4 | 16.2 | 26.5 | 3.2 |
| | 2 | - | - | 10.6 | 2.4 | 33.1 | 4.2 | 20.2 | 29.5 |
| PO6 | 3 | - | - | 76.6 | 2.7 | 2.0 | 4.3 | 12.8 | 1.6 |
| | 4 | - | - | 3.1 | - | 44.0 | 0.2 | 13.7 | 39.0 |
| PCO5 | 5 | 71.8 | 7.9 | 20.4 | - | - | - | - | - |
| PCO6 | 6 | 42.7 | 4.2 | 53.1 | - | - | - | - | - |

i

Figure 5.3. Surface morphology and cross-sectional SEM images of (a,b) PO5, (c,d) PO6, (e,f) PCO5 and (g,h) PCO6 samples with i) EDX analyses of the spots indicated within b, d, f and h.

Cross-sectional SEM images of the PO5 sample (Figure 5.3b) revealed the repeated lamellar structure of greyish and white layers. EDX analyses indicated that the white layer (spot 1 in Figure 5.3b) is rich in Zr (16.2%), Ti (12.4%), and O (35.3%), while the greyish layer (spot 2 in Figure 5.3b) contains a high concentration of Co (33%) and Sb (29.5%). In contrast, the PO6 sample (Figure 5.3d) displayed a top white layer with vertical cracks instead of the multi-layer structure observed in the PO5 sample.

It is of interest to note by comparing the oxide cases formed on the cross-section PO5 and PO6 (Figure 5.3d) that the oxide case formed on PO5 (Figure 5.3b) looks thicker than that formed on PO6 (Figure 5.3d) although PO5 was oxidised at 500 ℃ for 10h whilst PO6 was tested at a higher temperature of 600 ℃ for a longer duration of 50h. This implies that severe spallation might have occurred during the static oxidation testing of the PO6 sample.

The retained surface case observed from Figure 5.3d could be divided into two layers according to their contrast: a very thin grey superficial layer on a thick white layer. The top grey thin layer was found to be oxygen-rich (76.6%, Spectrum 3 in Figure 5.3i), indicating the formation of oxides, while the white thick layer is rich in Co (33%) and Sb (29.5%) with a low oxygen concentration of 3.1% (Spectrum 4, Figure 5.3i), signifying the formation of CoSb compound.

As shown in Figure 5.3e&g, the surface morphologies of CrSi-coated P-type materials after oxidation revealed no spallation. PCO5 sample surface (Figure 5.3e) looked similar to that for the as-coated sample but close observation revealed some fine flake-like features (Figure 5.1a). While for the PCO6 sample, the coating surface was covered with polygonal-shaped particles (Figure 5.3g). Cross-sectional SEM images of PCO5 and PCO6 samples (Figure 5.3f&h) demonstrate that the CrSi coatings remained their integrity without spallation, cracks or interface debonding. No appreciable oxide films could be seen although the superficial surface looked dark, especially for the PCO6 sample (Figure 5.3h).

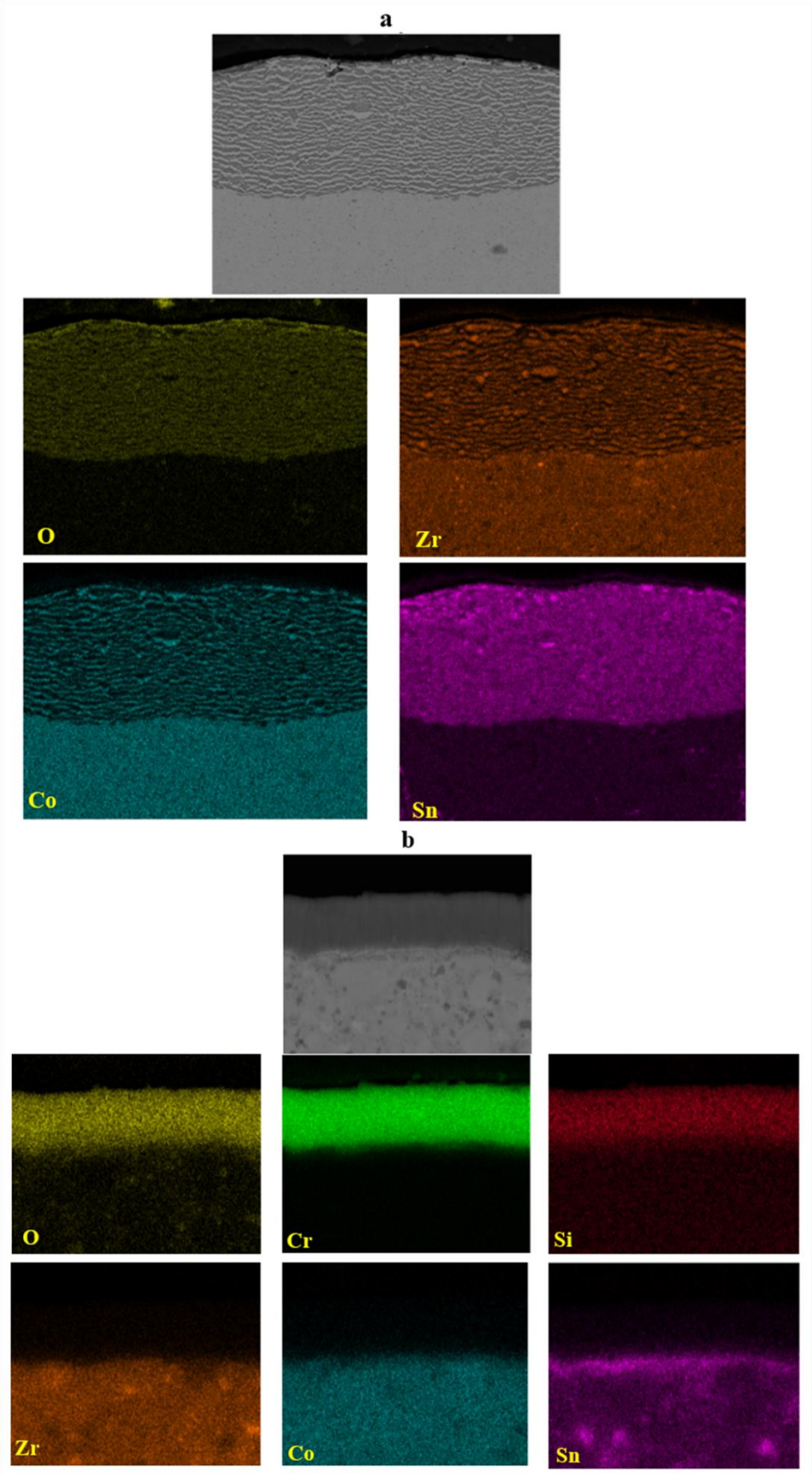


Figure 5.4. Cross-sectional elemental distribution of (a) PO5 and (b) PCO5 samples.

EDX analysis within the CrSi coating layers revealed high oxygen contents at the area chosen to the top surfaces (Figure 5.3i, Spectrums 5&6) with the PCO6 showing very high oxygen content (53.1 at%) and significantly reduced Cr (42.7 at%) and Si (4.2 at%) after oxidation at high temperature (600°C) and for a long time period (50h).

To investigate the distribution of the elements, EDX element mappings were conducted on the cross-sections of PO5 and PCO5 samples and the results are presented in Figure 5.4. It can be seen from Figure 5.4a that a multi-layered oxide case is formed, which is enriched with oxygen and Tin (Sn). This indicates that both severe oxidation and sublimation of Sn from the TE material occurred during the static oxidation tests. In contrast, the multilayer structure observed on the PO5 sample surface (Figure 5.4a) was fully eliminated by the CrSi coating layer (Figure 5.4b). As expected, the coating layer mainly consists of Cr and Si and no macro diffusion of such elements to the TE substrate could be detected.

It can also be seen that the coating layer is enriched with oxygen, but the oxygen was trapped in the CrSi coating layer without diffusion to the TE substrate. The trapped oxygen most probably existed as interstitial in the bcc structure of the CrSi coating because no oxides could be identified by either XRD or SEM. However, it is of interest to note that element Sn diffused outward from the underneath TE material to form a Sn-rich interface layer (Figure 5.4b). A similar elemental distribution was observed for the PCO6 sample.

### *5.4.3 CrSi coating protection on static oxidation of the N-type TE material*

#### *5.4.3.1 Phase identification of the oxide layers*

The phase constitution of the N, NO5, and NO6 samples was analysed using XRD, and the typical patterns obtained are presented in Figure 5.5a. The N sample can be identified a singular half-Heusler phase of (Zr,Ti)Ni(Sn,Sb) (cubic, a=b=c= 0.603 nm, PDF: 01-089-7155). However, distinct phase changes were observed for the oxidised N-type samples.

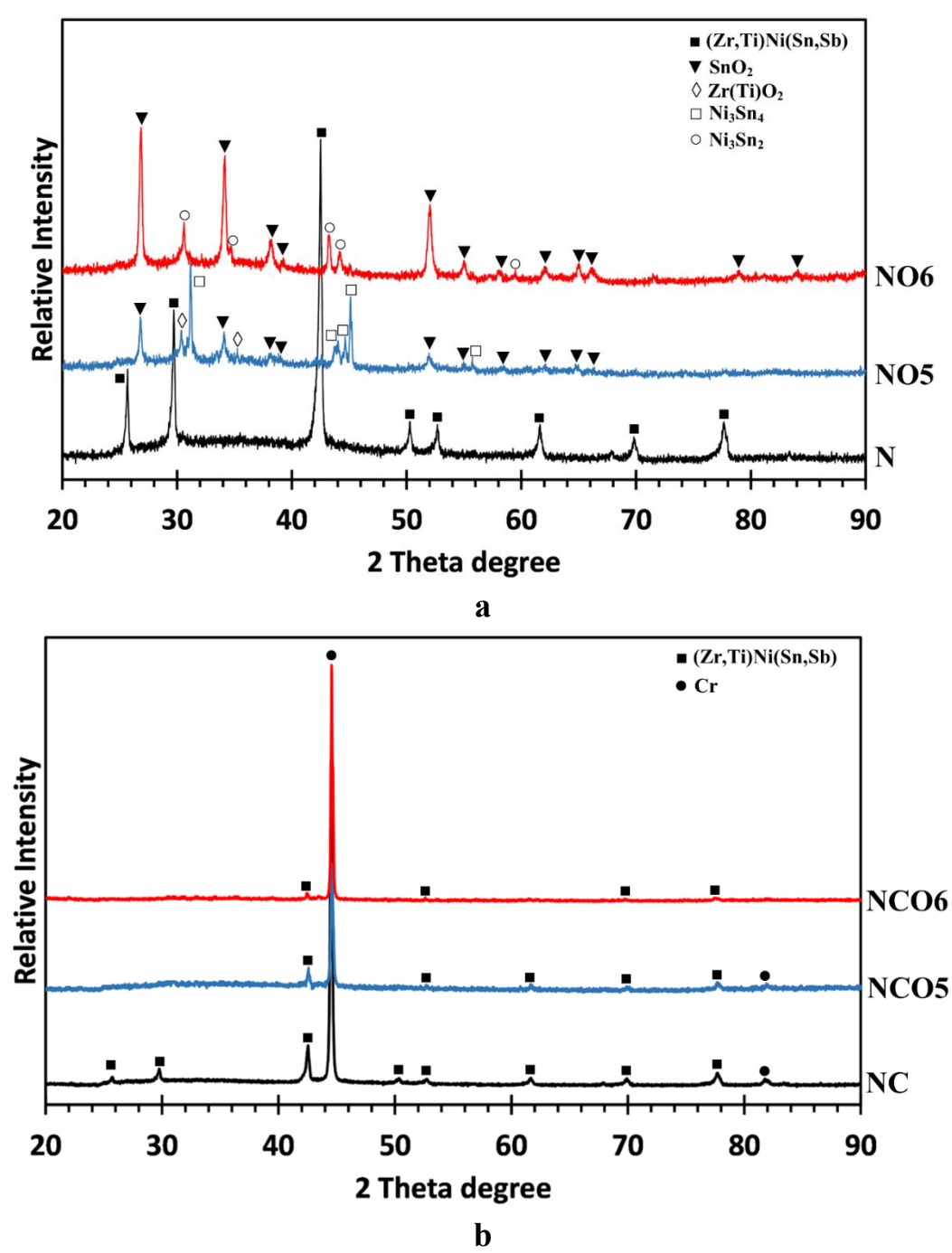


Figure 5.5. XRD patterns of (a) N, NO5, NO6 samples, and (b) NC, NCO5 and NCO6 samples

The typical XRD patterns of the NC, NCO5, and NCO6 samples are presented in Figure 5.5b.

In addition to relatively weak diffraction peaks attributed to the secondary $Zr(Ti)O_2$ phase (tetragonal, a=b= 0.35 nm, c=0.51 nm, and PDF: 01-079-1763) for the NO5 sample, high-intensity diffraction peaks corresponding to the $SnO_2$ (tetragonal, a=b= 0.47 nm, c=0.31 nm, and 96-153-3668) and $N_3Sn_4$ (monoclinic, a= 1.21 nm, b= 0.40 nm, c= 0.51 nm, and PDF: 03-

065-9639) phases were identified. In contrast, strong diffraction peaks corresponding to $SnO_2$ and $Ni_3Sn_2$ (hexagonal, a=b= 0.41 nm, c= 0.51 nm, and PDF: 96-152-3549) phases were identified for the NO6 sample and the $N_3Sn_2$ phase formed in the NO6 sample possibly was transformed from the $Ni_3Sn_4$ phase observed for the NO5 sample, owing to an increase in the oxidation temperature and duration.

For all these samples, a strong diffraction peak corresponding to the bcc Cr phase was observed, indicating that Si-doped Cr coatings remained stable on the surface even after oxidation at high temperatures. The half-Heusler phase of (Zr,Ti)Ni(Sn,Sb) from the substrate was also detected with weak diffraction peaks. Remarkably, no such phases identified from the NO5 and NO6 samples could be detected from the NCO5 and NCO6 samples, indicating effective oxidation protection of the CrSi coating to the N samples.

*5.4.3.2 Surface morphology and cross-section SEM observations*

SEM observations on the surface of the NO5 sample (Figure 5.6a) revealed the formation of swirly features and large particles. On the NO6 sample surface (Figure 5.6c), both large and small oxide particles were observed. The cross-sectional view of the NO5 sample (Figure 5.6b) shows a layer-by-layer structure, similar to the layered structure observed from the cross-section of the PO5 sample, consisting of alternate greyish and white layers. EDX analyses disclosed that the white layers were rich in Sn and Ni, and the greyish layers were enriched with Zr, Ti, and O (Figure 5.6g). Minor delamination defects are visible between some multilayers as arrowed in Figure 5.6b. In contrast, only two layers, a thick top layer enriched in Sn and O (possibly an oxide layer) and a second layer with high Ni and Sn content, were observed from the cross-section of the PO6 sample (Figure 5.6d). Most probably, spallation occurred as evidenced by the thin white superficial layer retained from the spalled white layer. These observations point out a rapid diffusion of a significant amount of Ni and Sn toward the surface. Subsequently, the diffused Sn reacted with oxygen and formed the $SnO_2$ top layer on the

surface. The surface morphologies of the NCO5 and NCO6 samples are similar to that of the PCO5 and PCO6 samples. However, on the cross-section, a notable interface layer was observed between the CrSi coating and the TE material for both NCO5 and NCO6 samples (Figure 5.6e&f).

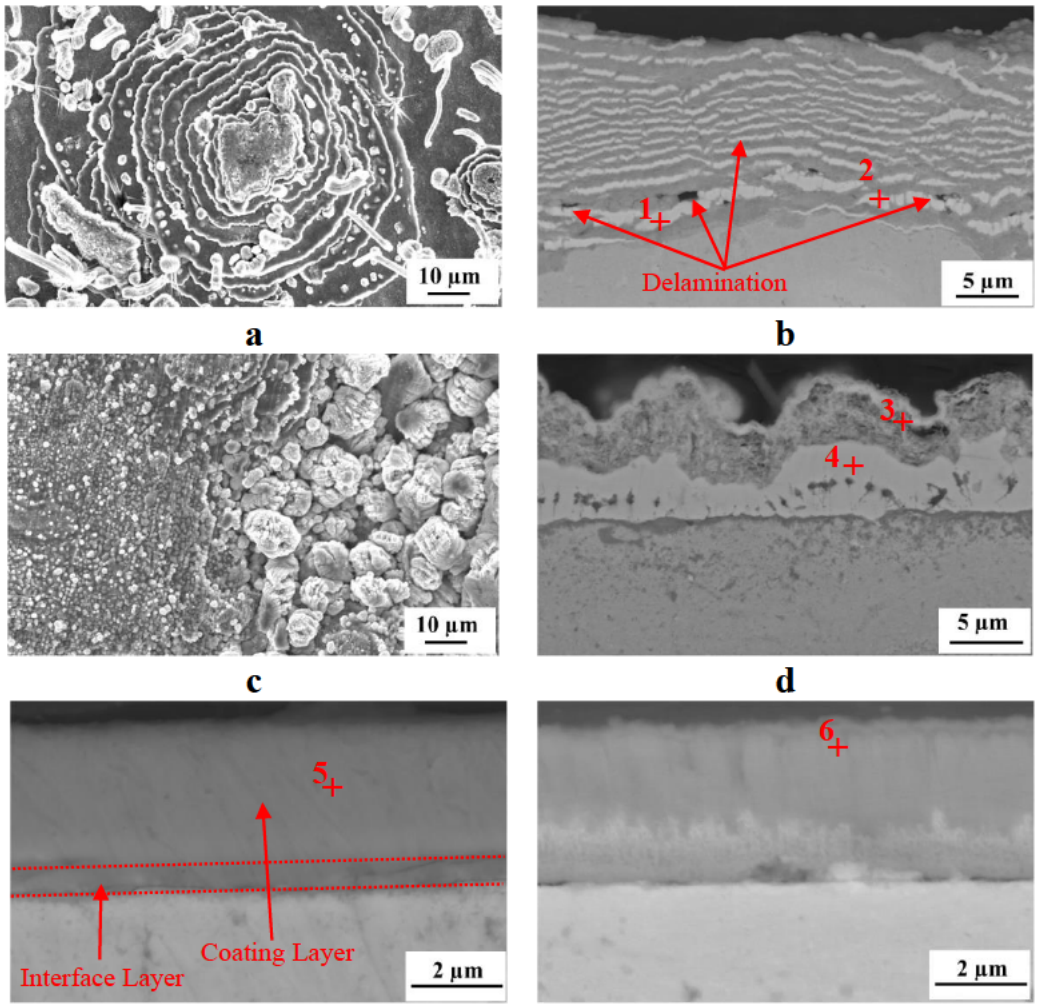


| Materials | Spectrum | Elements (at. %) | | | | | | | |
|---|---|---|---|---|---|---|---|---|---|
| | | Cr | Si | O | Ti | Ni | Zr | Sn | Sb |
| NO5 | 1 | - | - | 21.2 | 8.4 | 14.1 | 5.6 | 35.7 | - |
| | 2 | - | - | 50.5 | 5.9 | 5.7 | 15.7 | 22.3 | - |
| NO6 | 3 | - | - | 73.4 | - | 0.3 | - | 26.3 | - |
| | 4 | - | - | 25.7 | - | 39 | - | 35.1 | - |
| NCO5 | 5 | 51 | 6.1 | 42.9 | - | - | - | - | - |
| NCO6 | 6 | 43 | 4.7 | 52.3 | - | - | - | - | - |

g

Figure 5.6. Surface morphology of (a) NO5 and (c) NO6 samples, and the cross-sectional SEM images of (b) NO5, (d) NO6, (e) NCO5 and (f) NCO6 samples, and g) EDX analyses of the spots indicated within b, d and f.

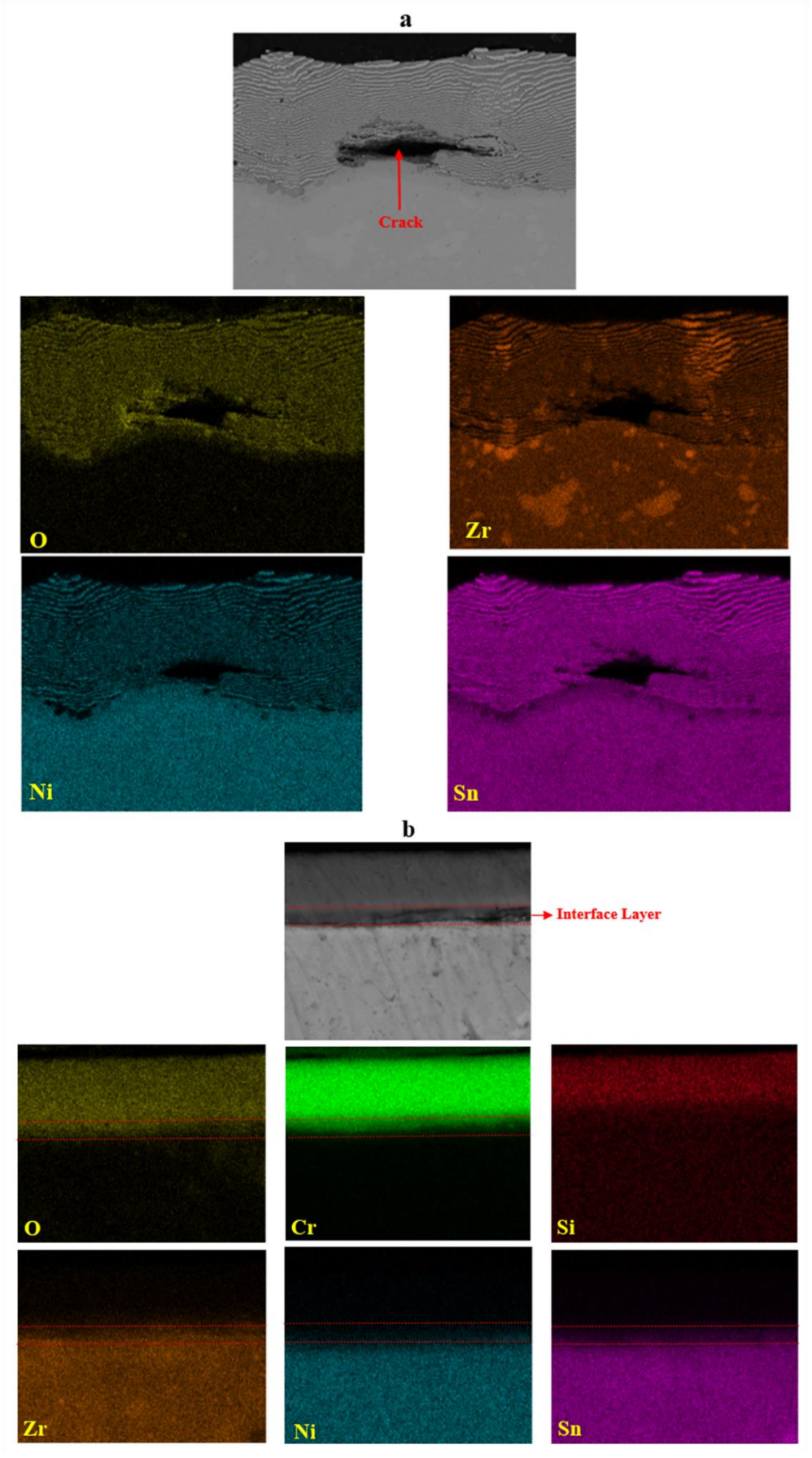


Figure 5.7. Cross-sectional elemental distribution of (a) NO5 and (b) NCO5 samples

The EDX elements mapping on the multilayer structure of the NO5 sample shows that the white contrasts are rich in Ni, Sn, and Sb, while the greyish contrasts exhibit high Zr and Ti concentrations (see Figure 5.7a). Certain regions in both multilayer structure and matrix showed high Zr content, which can be attributed to the initial inhomogeneous microstructure of the sample. In contrast, for the NCO5 sample, although oxygen can penetrate into the CrSi coating, negligible oxygen can be detected in the TE material substrate, demonstrating the effective oxidation protection of the CrSi coating. An interface layer (as denoted in Figure 5.7b) between the substrate material and the coating was formed by the diffusion of Sn, Ni from the TE material, and Cr, O from the coating. Silicon stably stayed within the coating layer. Similar features were observed for the NCO6 sample.

### *5.4.4 CrSi coating protection on cyclic oxidation of TE materials*

#### *5.4.4.1 Mass gain*

During cyclic oxidation testing at 500℃ for 50 cycles, the mass gains of both N-type and P-type samples with and without CrSi coating after each cycle were measured separately, and the obtained data are presented in Figure 5.8. For the NO5-50 sample, a sharp increase in mass gain was seen after 50 cycles, while it gradually increased up to 20 cycles and then remained nearly constant until 50 cycles for the PO5-50 sample. The final mass gains for the N-type and P-type samples after 50 cycles were 5.77 mg/cm² and 2.1 mg/cm², respectively. In contrast, the mass gains during the cyclic oxidation at 500℃ for CrSi-coated N-type and P-type increased very slowly with the cycling number. After 50 cycles, the total mass gains for the NCO5-50 and PCO5-50 samples were 0.77 mg/cm² and 0.21 mg/cm², respectively. This demonstrates the effectiveness of the CrSi coating layer in protecting the TE materials from oxidation when compared to the PO5-50 and NO5-50 samples.

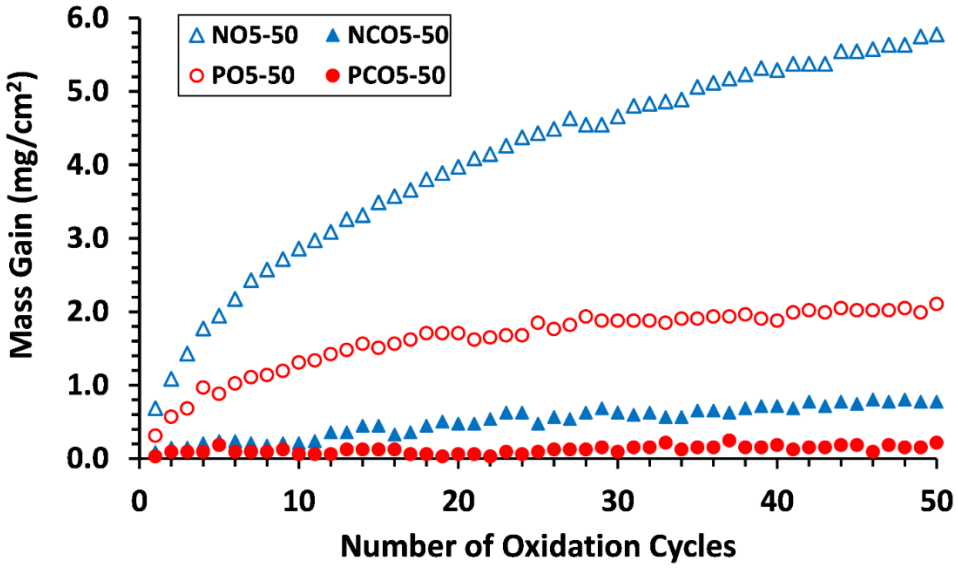


Figure 5.8. Mass gain of N (uncoated N-type), NC (coated N-type), P (uncoated P-type) and PC (uncoated P-type) samples after each cycle of the cyclic oxidation at 500°C/1h for 50 cycles. The N and P results [227] are included for comparison.

### 5.4.1 3.4.2. Phase identification of the oxide layers

Figure 5.9a shows typical XRD patterns of the PO5-50 and PCO5-50 samples compared with the P sample. For the PO5-50 sample, the $SnO_2$ (tetragonal, a= b= 0.47 nm, c= 0.31 nm, PDF: 01-077-0447) and CoSb (hexagonal, a= b= 0.39 nm, c= 0.51 nm, PDF: 96-154-1040) phases with high intensity were detected. A few diffraction peaks corresponding to the $Sb_2O_4$ phase (orthorhombic, a= 0.54 nm, b= 0.48 nm, c= 1.17 nm, PDF: 01-071-0564) were also identified. For the PCO5-50 sample, strong peaks of the bcc Cr phase from the CrSi coating were observed with a few diffraction peaks from the half-Heusler matrix phase of (Zr,Ti)Co(Sn,Sb). Weak peaks of the $Cr_2O_3$ phase were also identified for the PCO5-50 sample.

The XRD patterns of the N, NO5-50 and NCO5-50 samples after the cyclic oxidation test are presented in Figure 5.9b. The diffraction patterns for the NO5-50 sample reveal phases of $SnO_2$ (tetragonal, a= b= 0.47 nm, c= 0.31 nm, PDF: 01-070-4177) and $Ni_3Sn_4$ (monoclinic, a= 1.22 nm, b= 0.40 nm, c= 0.52 nm, PDF: 03-065-4310) with high intensity, and Zr(Ti)$O_2$

(orthorhombic, a=b= 0.50 nm, c= 0.52 nm, PDF: 00-037-1413) with low intensity. For the NCO5-50 sample, the substrate phase of (Zr,Ti)Ni(Sn,Sb), bcc structured Cr phase with high intensity, and an oxide phase of $Cr_2O_3$ (hexagonal, a=b= 0.49 nm, c=1.35 nm, and PDF: 96-210-4123) weak peaks were identified. The detected $Cr_2O_3$ oxide phase can be attributed to the oxidised CrSi coating remaining on the sample. No oxide phases of the substrate elements can be detected for both PCO5-50 and NCO5-50 samples, indicating the oxidation protection of the CrSi coating to the TE materials

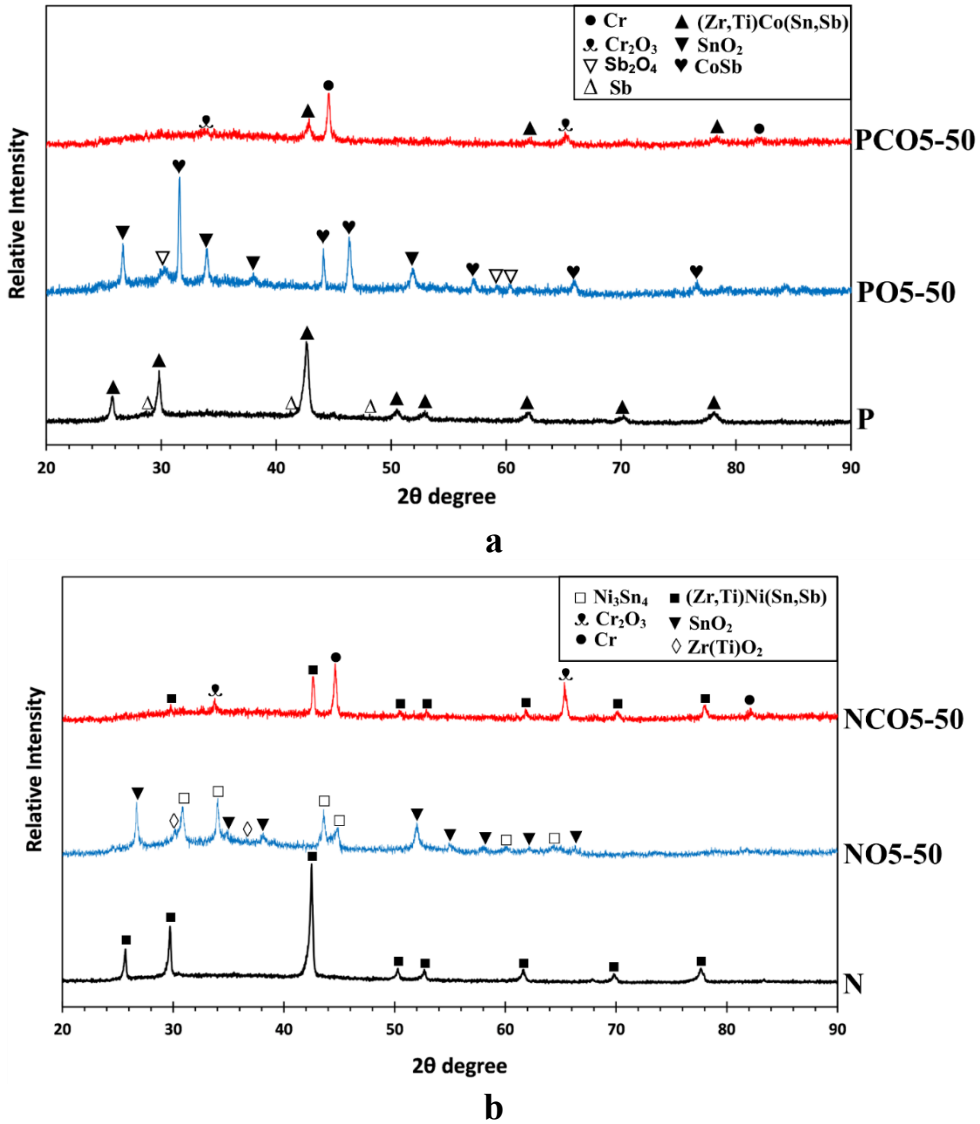


Figure 5.9. Typical XRD patterns of (a) P, PO5-50 and PCO5-50 samples, and (b) N, NO5-50 and NCO5-50 samples. The N and P results [227] are included for comparison.

*5.4.1.1 Surface morphology and layer structure*

Figure 5.10 shows the surface morphologies and cross-sections of N, P, NC and PC samples after cyclic oxidation at 500℃ for 50 cycles. Large cauliflower-like particles formed on the NO5-50 sample surface (Figure 5.10a), while small particles formed on the PO5-50 sample surface (Figure 5.10c). The cross-sectional view exhibits a multi-layer structure on both the NO5-50 and PO5-50 samples (Figure 5.10b&d), similar to the structures observed on the NO5 and PO5 samples. However, in contrast to the PO5 sample, an interface layer was identified between the multi-layer structure and the matrix for the PO5-50 sample. Delamination and cracks were observed at the interface between the layered structure and matrix in the NO5-50 sample (Figure 5.10b), while similar defects occurred within the layered structure of the PO5-50 sample (Figure 5.10d). For the CrSi coating samples, some polygonal-shaped particles formed on the surfaces (Figure 5.10e&g), and the quantity of the polygonal-shaped particles is more for the NCO5-50 sample than that for the PCO5-50 sample. As shown in Figure 5.10f&h, a very thin surface layer with a slightly dark contrast was formed on the CrSi coating; the main part of the coating looks featureless; and the interface between the CrSi coating and the substrate is perfectly integrated. Neither cracking nor delamination could be observed on the CrSi-coated samples after 50 cycles of oxidation. The EDX elements mapping for the PO5-50 sample (Figure 5.11a&b) revealed that element distribution within the white and greyish contrasted multi-layer structure was similar to that of the PO5 sample (see Figure 5.4). For the PCO5-50 sample, the abovementioned interface layer between the multilayer structure and the matrix was identified as rich in Zr, Ti as well as oxygen (Figure 5.11a). It can be seen that the oxygen was only trapped in the CrSi coating for the PCO5-50 sample (Figure 5.11b). In addition, Sn was diffused to the interface between the matrix and the CrSi coating. The elemental mapping of the NO5-50 and NCO5-50 samples was also studied, and the findings were similar to those observed for the NO5 and NCO5 samples, as presented in Figure 5.7.

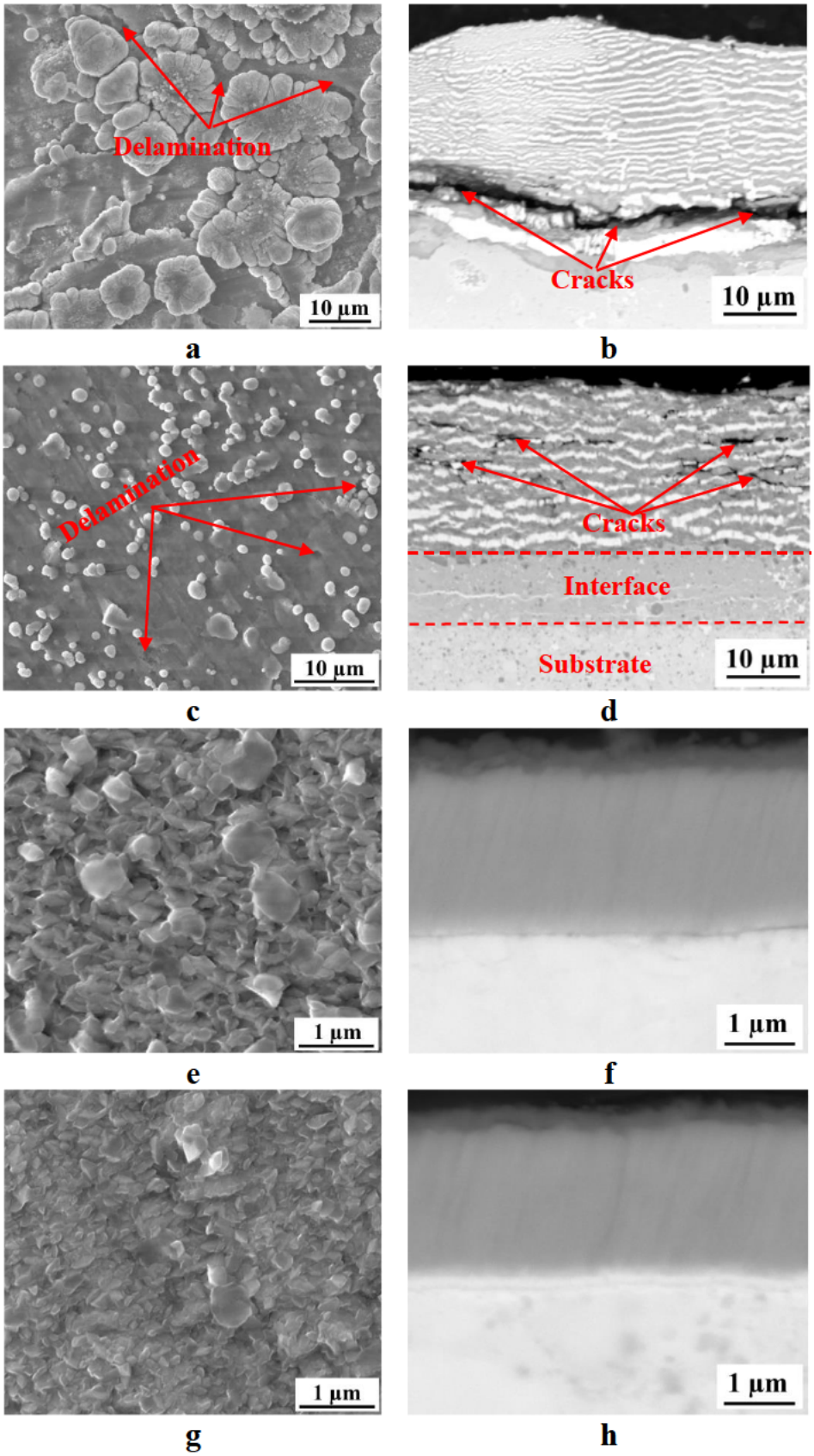


Figure 5.10. Surface morphologies and cross-sectional microstructures of (a,b) NO5-50, (c,d) PO5-50, (e,f) NCO5-50, (g,h) PCO5-50 samples.

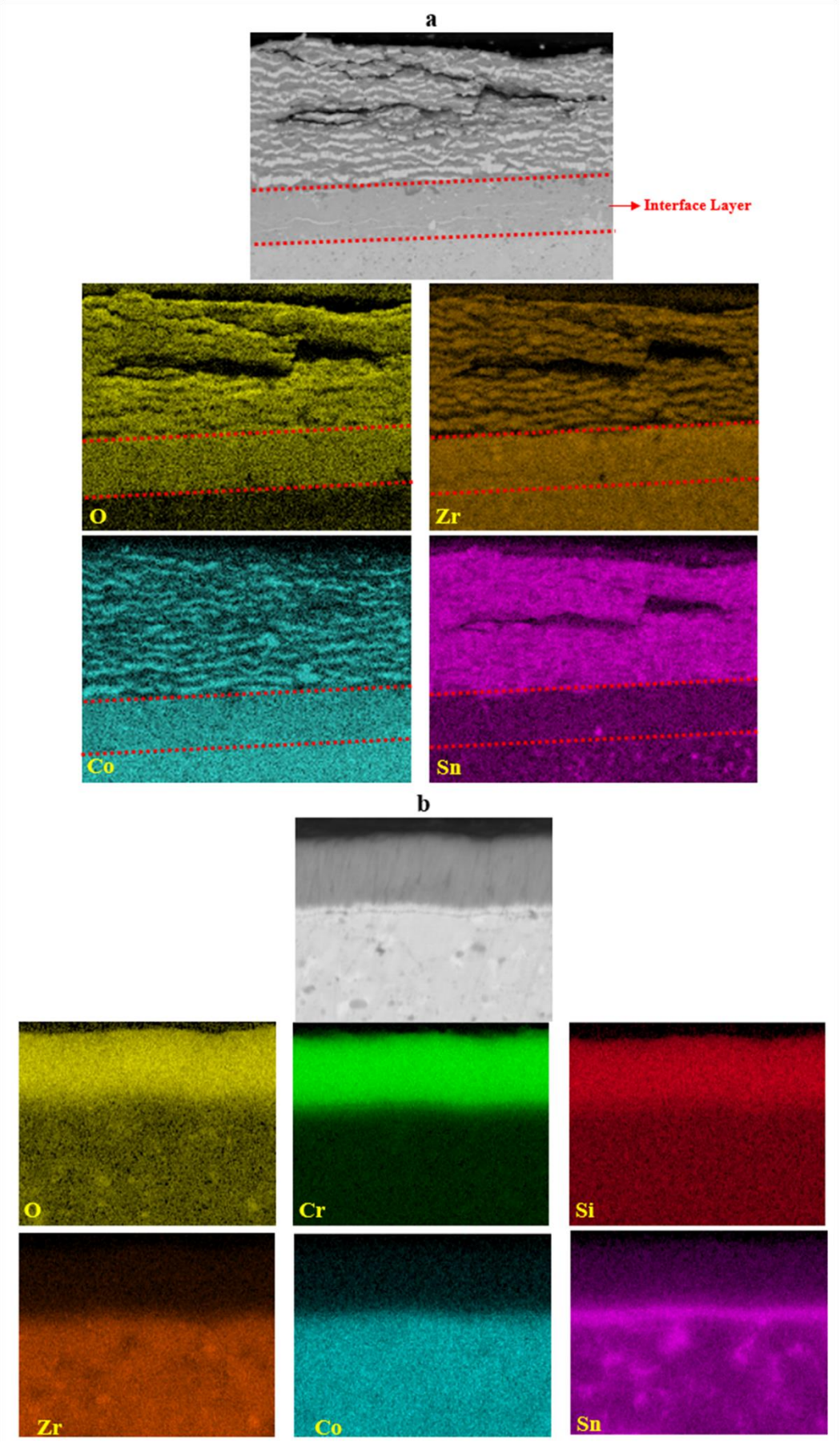


Figure 5.11. Cross-sectional elemental distribution of (a) PO5-50 and (b) PCO5-50 samples

## 5.5 Discussion

### *5.5.1 Oxidation behaviour comparison for P-type and N-type TE materials*

In this paper, the oxidation behaviour of N-type (Zr,Ti)Ni(Sn,Snb) and P-type (Zr,Ti)Co(Sn,Sb) TE materials under static oxidation conditions (500℃/10h and 600℃/50h) is reported, which has been established a foundation for the comparison of the oxidation behaviour of the P-type and N-type TE materials under both static and cyclic oxidation conditions when referring to the results we published in Ref [227].

To this end, the mass gain results reported in this paper (static oxidation at 500℃ for 10h) and Ref [227] (cyclic oxidation for 10 cycles with a total oxidation duration at 500℃ for about 10h) are compared in Table 5.3. It is clear that the oxidation behaviour judging by mass gain is closely related to both the type of TE materials (N or P) and the oxidation condition (static or cyclic).

Table 5.3. Mass gain during static and cyclic oxidation for N-type and P-type TE materials

| Type of Materials | N-type | | P-type | |
|---|---|---|---|---|
| Oxidation method | Static | Cyclic | Static | Cyclic |
| Sample Code | NO5 | NO5-50 | PO5 | PO5-50 |
| Mass gain ($mg/cm^2$) | 1.8 | 2.8 | 1 | 1.2 |

It can be seen from Table 5.3 that the mass gain for the N-type TE material is larger than that of the P-type under both static and cyclic oxidation conditions. This is supported by the examination of the surface morphologies and cross-section structures of the oxidation-tested TE materials. After being tested under static oxidation conditions at 500℃ for 10h, SEM images of the surface of the P-type sample (Figure *5.3*a) present small oxide particles ($ZrO_2$, $TiO_2$ and $SnO_2$), while large features and multilayered mountain-like-growth structures formed on the N-type sample surface (Figure *5.6*a) after 10 hours. Although a similar lamellar structure was formed on the cross-sections of both N-type and P-type materials, observable delamination

between the multilayers of the NO5 sample (Figure *5.6*b) led to further inward diffusion of oxygen into the material, leading to more oxidation and a thicker multilayered oxide case compared to that for the PO5 sample (Figure 5.3b). When intensifying the oxidation testing conditions by increasing the temperature to 600℃ and the oxidation duration to 50h, the size of the oxide particles increased with deep cracks on the PO6 surface (Figure 5.3c), whereas very large oxide products with loose contact formed on the NO6 sample surface (Figure 5.6c).

Similarly, as shown in Table 5.3, after cyclic oxidation between room temperature and 500℃ for 10 cycles (equivalent to about 10h in total at 500℃), the mass gain is greater for the N-type (2.8 mg/cm$^2$) than that for the P-type (1.2 mg/cm$^2$). SEM observation on the cross-sections revealed strong evidence that severe spallation of the surface layer occurred in the tested N-type sample whilst a very mild superficial crack was observed for the P-type sample [227].

The above-observed difference in mass gain for the N-type and P-type materials could be related to the difference in their chemical compositions (Table 5.1) and hence oxidation products. Thermodynamically, Zr, Ti and Sn are prone to be oxidised compared with Ni, Co and Sb, as they have higher oxygen affinity and more negative enthalpy of formation of oxide products. As evidenced in Table 5.1, both the N-type and the P-type materials possess a similar amount of Ti and Zr but the N-type material contains a much larger amount of Sn (33.3 at%) as compared with the P-type material. Therefore, a fast Sn diffusion to the surface, due to its high sublimation at even low temperatures, during the oxidation led to the fact that the majority of the oxide particles formed on the NO5 surfaces is $SnO_2$. This is supported by the strong peaks corresponding to the $SnO_2$ phase, as shown in Figure *5.5*a (for static oxidation) and Figure *5.9*b (for cyclic oxidation). The spallation of the multi-layered surface case on oxidised N-type material is most probably related to the difference in the thermal expansion coefficient of $ZrO_2$ ($7x10^{-6}$ $K^{-1}$), $TiO_2$ ($10.2x10^{-6}$ $K^{-1}$) and $SnO_2$ ($11.7x10^{-6}$ $K^{-1}$) [204, 228]. On the other hand, as shown in Table 5.1, compared with the N-type, the P-type contains much less (10.7at%) Sn and

a large amount of Co (29.1 at%) and Sb (25.7 at%). As depicted in Figure 5.2a and Figure 5.9a, in addition to the $SnO_2$ phase, the oxidised P-type surfaces are dominated by the CoSb intermetallic phase. Hence, the significantly reduced amount of Sn in the P-type can help to reduce the stress concentration, oxide layer spallation and oxidation of the P-type material.

### *5.5.2 Comparison of static and cyclic oxidation*

The cyclic oxidation behaviour of the N-type and P-type materials was comprehensively investigated in our previous publication [227], and some of the results for the cyclically oxidised materials were included in this paper to investigate the effect of thermal cycles involved in the service of TE materials and devices by comparing cyclic oxidation to static oxidation.

As evidenced in Table 5.3, the weight gain for both N-type and P-type materials is more from the cyclic oxidation than that from static oxidation; however, the difference in weight gain caused by different oxidation methods (static vs cyclic) is larger for the N-type than for the P-type.

The phases of CoSb and $SnO_2$ dominated the surface of the oxidised P-type material after long-term oxidation regardless of the oxidation method (see Figure 5.2a&Figure 5.9a), whilst the oxidised N-type surface mainly contains phases of $Ni_3Sn_4$ and $SnO_2$ (see Figure 5.5a&Figure 5.9b). Although the phases formed during static and cyclic oxidation are similar, the oxidation damage is different. Some cracks were observed at the interface of the multilayers for the cyclic oxidation-tested P-type PO5-50 sample (Figure 5.10d) and very large cracks at the interface between the multilayered surface case and the substrate for the NO5-50 sample (Figure 5.10b), which happened because of the stress concentration at the surface case and substrate or at the interface of the multilayers due to the effect of cyclic heating and cooling. In contrast, only very short cracks at the interfaces of the multilayers were observed on the cross-sections of statically oxidised PO5 (Figure 5.3b) and NO5 (Figure 5.6b) samples.

Clearly, the cyclically oxidised P-type and N-type materials suffered from thermal cycles between 25℃ and 500℃. Due to the thermal shock effect, the residual stress intensity at the multilayer structure could have reached critical levels over time, leading to micro/nano cracks formation where the coefficient of thermal expansion of the oxide products in the bright and dark contrasted layers is largely different [203-205]. Accordingly, the micro/nano crack growth along the interface of the alternated layers eventually caused delamination of the oxidised surface case on NO5-50 and the formation of micro-cracks at alternated layers for the PO5-50 sample, as denoted in Figure 5.10b&d. In particular, cracks and delamination formed in the multilayered structure created the pathways for further diffusion of oxygen into the material, leading to oxygen being rich under the multilayer structure and accelerated oxidation. From the CrSi coating view, it can be said that the PC and NC samples are well protected against static and cyclic oxidation. However, an interdiffusion layer between the CrSi coating and the substrate identified for the NO5 sample indicates that the quality of the produced coatings on different substrate materials is not the same (see Figure 5.4b&Figure 5.7b). The CrSi coating on the N-type material should have had more nanopores, which enabled further inward diffusion of oxygen along the coating, leading to diffusion of substrate elements and Cr to the interdiffusion layer (see Figure 5.7b). On the other hand, the stress-induced micro/nano cracks formed due to the cyclic and thermal shock effects also promoted further diffusion of oxygen into the coatings (NCO5-50 and PCO5-50 samples), resulting in the formation of the $Cr_2O_3$ phase for the NCO5-50 and PCO5-50 samples (see Figure 5.9), which was not detected for the statically oxidised NCO5, PCO5, NCO6 and PCO6 samples (see Figure 5.2b & Figure 5.5b).

### *5.5.3 CrSi coating protection of N-type and P-type TE materials*

It is well-known that the coating structure has great importance in the protection of the underlying substrate materials when exposed to high-temperature oxidation. As shown in Figure 5.1, the CrSi coatings deposited are quite dense with no appreciable pores and uniform

with a fine columnar structure. The coating layer is well adhered to the substrates without any spallation, which could help to prevent peeling-off and breaking of the coating layer during oxidation. As reported in Section 3, the CrSi coating can provide effective protection of both the P-type and N-type TE materials, which are characterised by inherent poor oxidation resistance when directly exposed to high-temperature environments in air, from oxidation under both static (Figure 5.4&Figure 5.7) and cyclic (Figure 5.10&Figure 5.11) oxidation conditions.

As shown in Figure 5.4b, neither cracks in the coating nor spallation at the interface can be observed after the static oxidation test at 500℃ for 10h (PCO5); the CrSi coating can successfully protect the P-type substrate material from oxidation. Although outward diffusion of Sn occurred, it was stopped by the CrSi coating thus preventing further sublimation of Sn from the substrate. Similar oxidation protection and element distribution were observed for the PCO6 sample tested at 600℃ for 50h.

Although the oxidation protection mechanism for Cr and/or Si coating is normally attributed to the strong affinity of Cr and Si to oxygen thus forming stable oxidation protection chromium oxides and silicon oxides, in this study XRD analysis failed to detect any peaks for any of these oxides from the oxidised surfaces of PCO5 and PCO6 (Figure 5.2b), which is in agreement with the XRD results for NCO5 and NCO6 samples (Figure 5.5b). However, oxygen penetration into the CrSi coating is clearly shown by O mapping (Figure 5.4) and it is of great interest to note that O did not penetrate through the whole coating layer, Si co-exists with the O and Cr is even across the whole coating depth.

The columnar structure of the CrSi coatings would provide a pathway along the grain boundaries for oxygen diffusion; however, the experimental results revealed that oxygen is mainly bounded in the coating (see Figure 5.4, Figure 5.7b and Figure 5.11b), thus stopping or retarding rapid diffusion of oxygen into the substrate and preventing the substrate from oxidation. Such seemingly contradicting results could be explained by the trapping effect of Cr

and Si. Due to the strong affinity of oxygen with Cr and Si, the inward diffusion of oxygen would be slowed down. In particular, the outward diffusion of Si (judged by its enrichment at the outer part of the coating) could effectively retard or stop the further diffusion of oxygen. Most probably, local clusters of Cr-O and Si-O would form at relatively low temperatures for a short period of oxidation; then extremely thin Cr/Si oxide films might have been formed when increasing the temperature and/or duration of time although the amount of the oxides is too low to be detectable by XRD.

The above-proposed mechanisms are supported by the oxidation results reported in this paper. As depicted in Figure 5.3i, the surface oxygen content measured at the very surface for PCO5 (500℃/10h) sample is 20.4 at%, which increased to 53.1 at% for PCO6 (600℃/50h). The ratio of Si to Cr is 11.0% and 9.8% for PCO5 and PCO6 respectively, which is higher than the original Si to Cr ratio of 8.2%. This is in line with the observation that a very thin black superficial layer could be observed from the PCO6 sample (Figure 5.3h), which is difficult to identify from PCO6 (Figure 5.3f). The formation of such a superficial black layer becomes clearer on the cross-sections of 50-cycle oxidation-tested NCO5-50 (Figure 5.10f) and PCO5-50 (Figure 5.10h). This is believed to be facilitated by the thermal stress concentration induced nano/micro-cracks, which promoted more oxidation at the near-surface.

The above mechanism is also supported by our early work on the oxidation behaviour of similar CrSi coating on 316 stainless steel at 600, 700 and 800°C for 80h [169]. Some weak peaks for $Cr_2O_3$ and $SiO_2$ were detected from the statically oxidised CrSi surface at 600°C due to the longer oxidation time (80h) as compared with the shorter (50h) tested samples in this study. When tested at higher temperatures of 700℃ and 800℃ for 80h, $Cr_2O_3$ (CTE: $7.3\times10^{-6}$/℃) and $SiO_2$ (5.8×10-6/℃) dominated the tested Si-doped Cr coating surfaces (CTE: $9.5\times10^{-6}$/℃) [229-231].

## 5.6 Conclusions

In this study, CrSi coatings were developed and deposited on the N-type (Zr,Ti)Ni(Sn,Sb) and P-type (Zr,Ti)Co(Sn,Sb) half-Heusler TE materials using a closed field unbalanced magnetron sputtering PVD system. A comprehensive and comparative study on the oxidation behaviour of CrSi-coated and uncoated TE materials was carried out by applying both static oxidation testing at 500℃ for10h and 600℃ for 50h, and cyclic oxidation between 25℃ and 500℃ for up to 50 cycles to simulate the service conditions for TE devices. Based on the experimental findings and comparative discussion, the study can be concluded as follows:

1. The surface of the uncoated N-type and P-type TE materials are entirely oxidised at 500℃ for 10h and 600℃ for 50h, leading to the formation of multilayered oxide cases and a significant change in the surface morphologies, phase constitution and potentially thermoelectric properties. The N-type material showed much worse oxidation damage as compared with the P-type material due to the difference in their chemical composition.
2. The oxidation behaviours of the uncoated N-type and P-type materials vary significantly depending on the oxidation method employed with the weight gain for both N-type and P-type materials being more from the cyclic oxidation than from static oxidation. Cyclic oxidation resulted in the formation of large cracks at the interface between the multilayered oxide case structure and the substrate for the N-type material and short cracks between multilayers for the P-type material.
3. The CrSi coatings developed showed very high thermal stability and oxidation resistance, which can effectively protect the N-type and P-type materials from oxidation and sublimation during both static and cyclic oxidation tests. The strong affinity of Cr and Si to oxygen can trap oxygen, retard its inward diffusion and thus protect the TE material substrate from oxidation. As implied by the dark superficial layer observed at

the edge of cyclic oxidation tested samples, most probably a thin chromium and/or silicon oxide layer might have formed on the coating surfaces although it is too thin to be detected by XRD, which has been confirmed by increasing the temperature and/or duration of oxidation tests.

Clearly, the promising results from the current study suggest that the CrSi coatings can effectively protect the N-type and P-type half-Heusler thermoelectric materials from oxidation and sublimation under both static and cyclic oxidation conditions. This finding could pave the way towards the further development of long-life high-performance TE generators and devices, thus contributing to the net zero target.

# Chapter 6 Development of Ni/NiGO contact layers for p-type (Zr,Ti)Co(Sn,Sb) thermoelectric material by low-cost electro-brush plating technique

## 6.1 Abstract

In this study, a conductive nickel (Ni) layer was deposited on P-type (Zr,Ti)Co(Sn,Sb) thermoelectric material (TE) using a highly flexible and low-cost electro-brush plating technique. Before deposition on the TE material, a comprehensive optimisation study was carried out by applying the Ni layer on 316 stainless steel substrate using voltages between 4V and 8V. In addition, a small amount of graphene oxide was incorporated into the Ni coating to improve the layer's electrical conductivity. However, the experimental findings showed no significant difference between the GO-added Ni (NiGO) coating and pure Ni coating in terms of the coating structure, hardness, sheet and interfacial contact resistances. Once the optimum voltage of 6V was determined, the developed optimal brush plating process was used to deposit the Ni layer on the P-type TE material. The thermal stability of the Ni-plated TE material was tested at 500℃ for 10 hours, and the results showed that the Ni layer was stable after oxidation and also protected the surface against further oxidation and sublimation.

## 6.2 Introduction

The ever-increasing need for energy has led to the development of alternative energy sources in addition to the use of fossil-based fuels [232]. Especially considering the negative effects of widely used fossil-based energy sources on the environment, it has become essential to develop technologies that use clean, renewable and sustainable energy sources. Among these energy sources, the development of thermoelectric (TE) technology has gained considerable momentum, especially in the last two decades [209, 233]. In addition to converting the primary

source of solar energy into usable electrical energy, TE technology can also convert the released waste heat.

However, heat-to-electricity conversion of TE modules with high efficiency is still a concern. In recent years, many researchers have focused on increasing the figure of merit ($zT=S2\sigma\kappa-1T$) value of TE materials [79, 171], which is an important way to increase thermoelectric efficiency. Even if the zT value can be enhanced to high values based on operating temperature for different TE materials [53, 234], heat-to-electricity conversion efficiency in practical applications depends to a large extent on TE module design [235, 236]. In addition to TE materials with high zT values, the use of appropriate electrode material and the optimisation of metallised contact layers with high electrical and thermal conductivity are also considered in thermoelectric module design to increase efficiency [237].

The contact of thermoelectric materials to the electrode is crucial to ensure TE module integrity and performance. The common ways to connect the TE materials to the electrode are welding or soldering [116]. However, the contact interface may degrade when exposed to high-temperature static or cyclic oxidation. As an effective alternative, metallising coatings are deposited on TE materials, acting as a contact layer at the interface between TE material and the electrode both to increase the electrical and thermal conductivity and to protect the TE material against oxidation. The operating temperature of the TE module needs to be taken into account when designing a high-quality contact layer. Single-layer metal contacts are generally applied to TE modules operating at low temperatures, while multilayer metal layers may be applied for high-temperature applications [238]. These contact layers prevent a possible chemical reaction between the electrode and high-entropy TE materials, ensure chemical composition stability in the TE material, and enable effective heat and electricity transmission due to its high electrical and thermal conductivity (low contact resistance) [116]. Recently, nickel (Ni) [239, 240], copper (Cu) [241] and cobalt (Co) [242] contact layers have become the

most promising because of their high conductivities and good adhesion properties on TE materials. In addition to the metallising coatings, such metal-matrix nanocomposite coatings as graphene oxide embedded Ni or Cu may also improve the contact properties.

Chemical and electrochemical coating techniques are widely preferred for the deposition of the abovementioned contact elements as a layer on TE materials [239]. However, the high initial investment cost and complicated operation limit the use of these methods. The electro-brush plating is a highly flexible and cost-effective technique to produce high-quality layers at a low cost. In this study, pure and GO-added Ni coatings were deposited on AISI 316 stainless steel and (Zr,Ti)Co(Sn,Sb) TE materials using the electro-brush plating technique. The parameter optimisation and microstructural characterisation were carried out on the Ni/NiGO-plated stainless steel. The optimal plating parameters were then employed to deposit the Ni coating onto the TE material. The thermal stability of the Ni-plated TE materials was also tested at 500°C for 10 hours, and the results indicated that the Ni contact layer could protect the material against oxidation and possible sublimation, in addition to its contribution to decreasing contact resistance.

## 6.3 Experimental

### *6.3.1 Materials*

Optimization of Ni and NiGO coatings was performed on 316 stainless steels with a chemical composition given in Table 6.1. A commercially obtained stainless steel bar with a diameter of 25.4 mm was cut to a thickness of 5 mm. The samples were sanded up to 1200 grit using SiC abrasive paper. The samples were cleaned with an ultrasonic device in sequential water and acetone for 10 minutes before the coating process.

The Ni coating determined by the optimisation study on the stainless steel was applied on the P-type (Zr,Ti)Co(Sn,Sb) half-Hesuler TE material as a contact layer. The TE material was

produced through high-energy ball milling of commercially obtained Zri Ti, Co, Sn and Sb powders in an inert environment (Ar) and plasma sintering at 800℃ for 4 minutes under a pressure of 500 kg/cm² using a uniaxial press (DSP 475, Dr. Fritsch).

Table 6.1. The chemical composition (at.%) of AISI 316 stainless steel used in this study.

| Material | Elements | | | | | | | |
|---|---|---|---|---|---|---|---|---|
| | C | Si | Mn | Cr | Ni | Mo | Fe | Other |
| AISI 316 | 0.03 | 1.00 | 2.00 | 16.50-18.50 | 10.00-13.00 | 2.00-2.50 | Bal. | <1.00 |

The chemical composition of the produced material is given in Table 6.2. The same sample preparation procedure for the stainless steel was followed to prepare the P-type material before the deposition of Ni & NiGO coating layers.

Table 6.2. The chemical composition (at.%) of the P-type half-Heusler TE material

| Material | Elements | | | | |
|---|---|---|---|---|---|
| | Zr | Ti | Co | Sn | Sb |
| (Zr,Ti)Co(Sn,Sb) | 18.1 | 16.4 | 29.1 | 10.7 | 25.7 |

### *6.3.2 Electro-brush plating*

#### *6.3.2.1 Preparation of plating solutions*

A commercial Ni ductile solution was used for Ni plating, while the NiGO plating solution was prepared in two steps. Initially, a 4 g/L GO suspension was prepared by activating 0.2 g of GO powders in 50 mL of deionised water through ultrasonication for 2 hours. Subsequently, varying amounts (1.25 mL, 2.5 mL, and 3.75 mL) of the prepared GO suspension were mixed with 50 mL of Ni ductile and subjected to ultrasonication for an additional hour, resulting in final compositions of 0.1 g/L, 0.2 g/L, and 0.3 g/L NiGO suspensions, respectively. A ready-to-use

electro-cleaning solution was used to remove potential dust and contaminations from the sample surface.

*6.3.2.2 Processing of Ni&NiGO deposition*

Ni and NiGO coatings were deposited to the substrates using the electro-brush plating kit (SPA Plating), providing precise control of DC voltage output. The plating kit contains the anode integrated with a pen holding the carbon electrode and the cathode with a crocodile mouth in contact with the sample. The electrode covered by cotton was periodically immersed in the solutions every ten seconds to prevent the cotton from drying. Before the coatings, the surface of the samples was subjected to electro-cleaning, the first stage of the brush plating, under 10 volts for 1 minute.

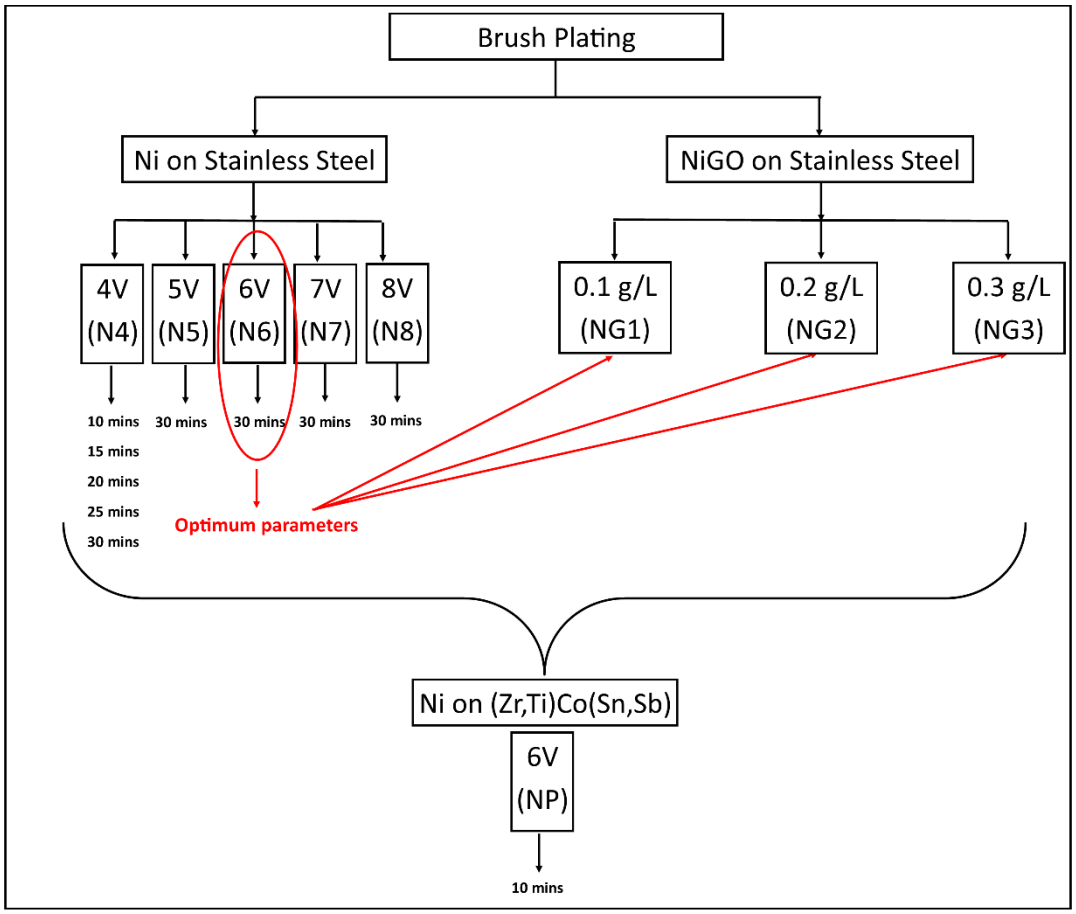


Figure 6.1. The selected Ni and NiGO plating parameters on the stainless steel with sample codes.

The Ni coatings were applied on the stainless-steel substrate with varying voltages from 4 to 8 for 30 minutes, as schematised in Figure 6.1. The corresponding sample codes are also indicated in brackets (N4 to N8 for Ni coatings, and NG1 to NG3 for NiGO coatings) in Figure 6.1. The optimum voltage (6V) and time (30 mins) parameters were then used for NiGO coatings.

Based on the findings, no major differences between Ni and NiGO coatings on the stainless steel were observed. Therefore, only Ni coating was deposited on the P-type material. The plating was carried out by applying the same voltage of 6V. As known, the deposition rate is comparably higher on the conductive substrates in the electro-brush plating technique. To this end, before the deposition of Ni coating on TE material, the electrical conductivity of the TE material was compared with that of the stainless steel to predict the process duration to get the optimum layer thickness. As the electrical conductivity of P-type material was higher than that of stainless steel, the plating time was reduced to 10 minutes to balance the thickness of the coating layer as expected. Specific parameters for the Ni & NiGO electro-brush plating process can be found in Table 6.3.

Table 6.3. Plating procedures for electro-brush plating of Ni and NiGO.

| Operation | Substrate | Voltage (V) | Time (min.) |
|---|---|---|---|
| Electro-cleaning | Stainless steel | 10 | 1 |
| | TE material | | |
| Electro-plating | Stainless steel | 6 | 30 |
| | TE material | | 10 |

### *6.3.3 Annealing and thermal stability tests*

The produced Ni & NiGO coatings were separately annealed at temperatures of 100℃, 200℃, 300℃… up to 800℃ for half an hour in the muffle furnace (Pyrotherm) in air. Furthermore, the uncoated and Ni-coated P-type TE materials were progressively oxidised at 500℃ for 10 hours to assess the material's thermal stability and the impact of Ni on oxidation protection.

### *6.3.4 General characterisation*

Microstructure, surface morphology and cross-section of the Ni & NiGO coating samples were analysed by the scanning electron microscope (SEM, Jeol UK Ltd.) and energy-dispersive spectroscopy (EDX, Oxford Instrument). The samples were X-ray scanned using a ProtoA XRD device with a Cu-Kα source (λ = 1.540598 Å), fixed resolution of 0.01493, step size of 4º (2θ) and dwell time of 2 (seconds) to analyse phase constitutions. The surface roughness was measured using an Ambious XP-200 profilometer (Cntech, UK) with a scanning speed of 0.05 mm/s over 8 mm in length. Depth profile analyses were conducted on the Ni & NiGO coated samples using the glow discharge optical emission spectroscopy technique. The hardness of the coatings was tested using Vickers Zwick-Roell hardness equipment by applying a load of 10 g, considering the material (very brittle) and coating thickness to be examined. The hardness of the annealed Ni & NiGO coating stainless steel samples was measured via a NanoTest Vantage instrument (Micro Materials Ltd) by applying an initial load of 0.02 mN and a maximum load of 20 mN, with a loading and unloading durations of half-minute. The sheet resistance of the samples was determined using an Ossila four-probe instrument, which was repeated five times on the same sample surface.

## 6.4 Results and discussion

### *6.4.1 Ni&NiGO coatings on stainless steel*

#### *6.4.1.1 Coatings microstructure and depth profiling*

Depth profile analyses of Ni-coated stainless steel samples were performed using GDOES, and the results are given in Figure 6.2a. As expected, the Ni coating thickness increased with increasing voltage because of the increased electric field, which accelerates the ion transport, leading to thicker coatings in a short time. On the other hand, the use of high voltage reduces the adhesion of the coating to the substrate, which causes degradation or peeling of the coating over time. In this case, the intended coating thickness (6 microns, medium deposition rate), was

achieved at 6V with a medium-speed deposition, which is also preferred for the deposition of GO-added Ni coatings. As seen in Figure 6.2b, coatings with almost the same thickness (range 6.5 – 8 microns) were obtained at the same voltage value of 6V, regardless of the GO concentration, meaning that although electro-brush plating is a manual process, it is quite reliable for obtaining specific coating thickness. For GO-added Ni coatings, the GO concentration in the coatings was analysed thanks to the presence of carbon, showing that GO nano-powders were impregnated into the Ni coating, as demonstrated in Figure 6.2c.

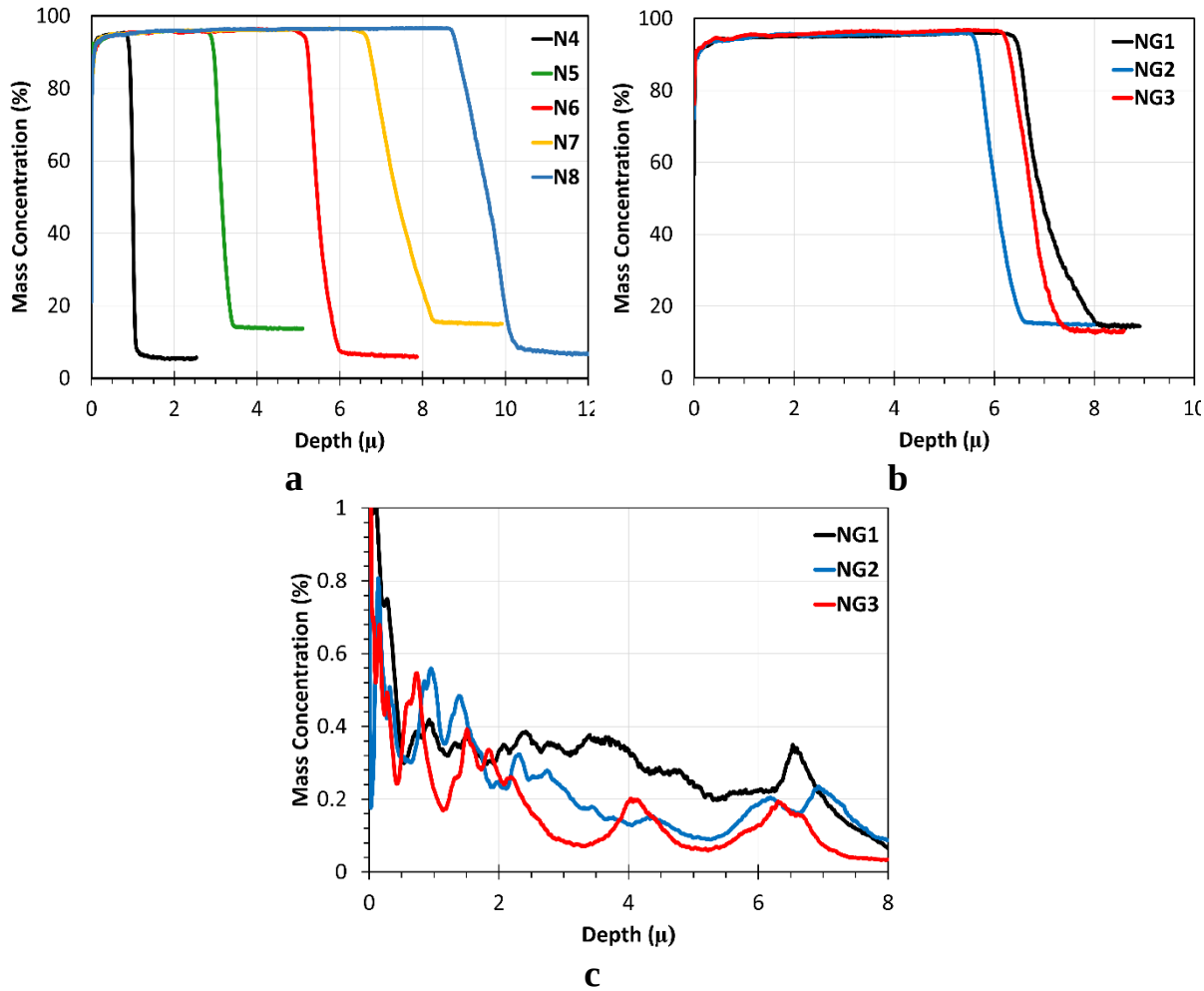


Figure 6.2. Mass concentration of the coatings along the depth; a) Ni coatings, b) NiGO coatings, c) carbon distribution in the NiGO coatings.

SEM images showing some characteristics of Ni-coated stainless steel samples are presented in Figure 6.3. The cross-sectional image of the N6 sample reveals a uniform Ni coating with no cracks and pores, and well adhesion to the substrate, indicating a high-quality deposition. Although the coating thickness differed depending on the voltage value, the coating quality (adhesion and no degradation) was similar for samples N4, N5 and N6. On the other hand, for the N7 and N8 samples, the coating at the edges of the sample was degraded during the brushing, which means that the quality of the coating decreased at high voltages, as shown in Figure *6.3* c&d.

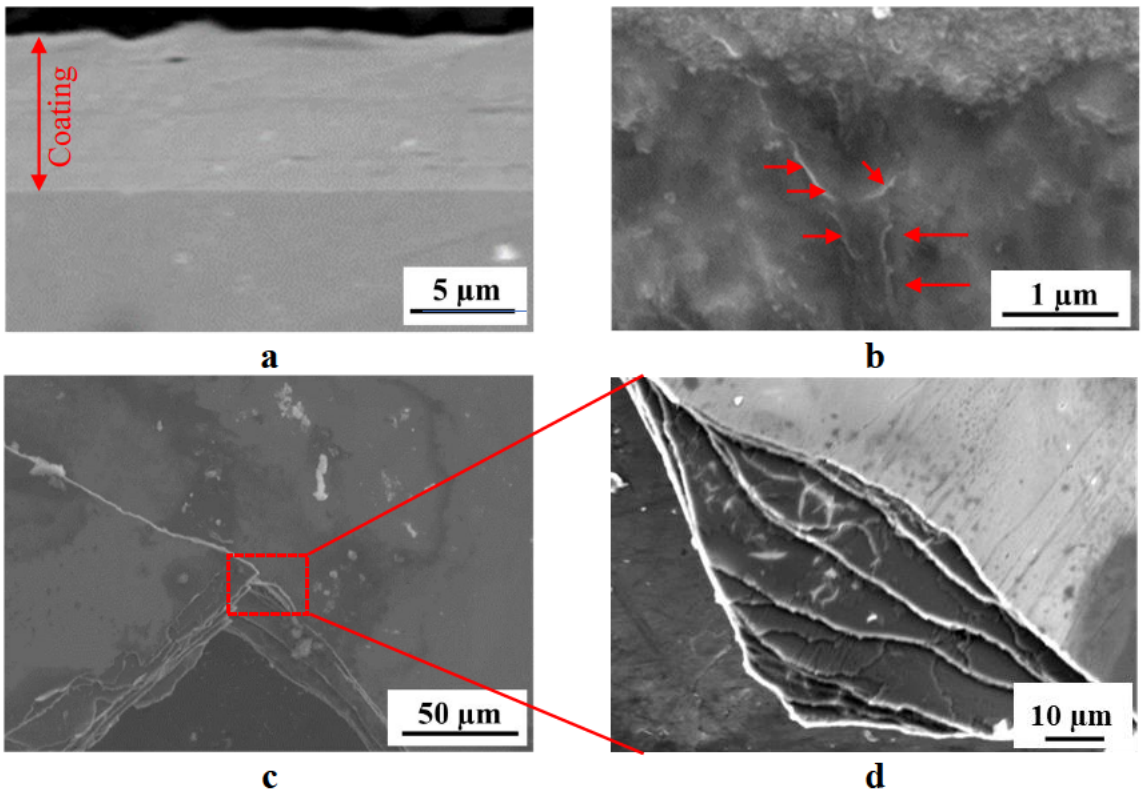


Figure 6.3. SEM images of the produced coatings; a) Cross section of N6 sample, b) GO sheets in the NG3 sample, c) crack formation during plating in the N8 sample, d) higher magnification of the fractured coating layer of the N8 sample showing the layer-by-layer structure.

The broken coating is further examined under high magnification (Figure 6.3d), and it was seen that the layer-by-layer structured coatings were deposited on the substrate. As it is known, the carbon electrode wrapped in cotton is dipped into the solution every 10 seconds and the plating

process continues. With each brushing, a nanosized coating layer is deposited. As the brushing continues, these nanosized layers accumulate on each other, creating multilayer structured coatings. For the NG3 sample, the GDOES crater was also analysed by SEM. As can be seen in Figure 6.3b, GO sheets were successfully incorporated into the Ni coating.

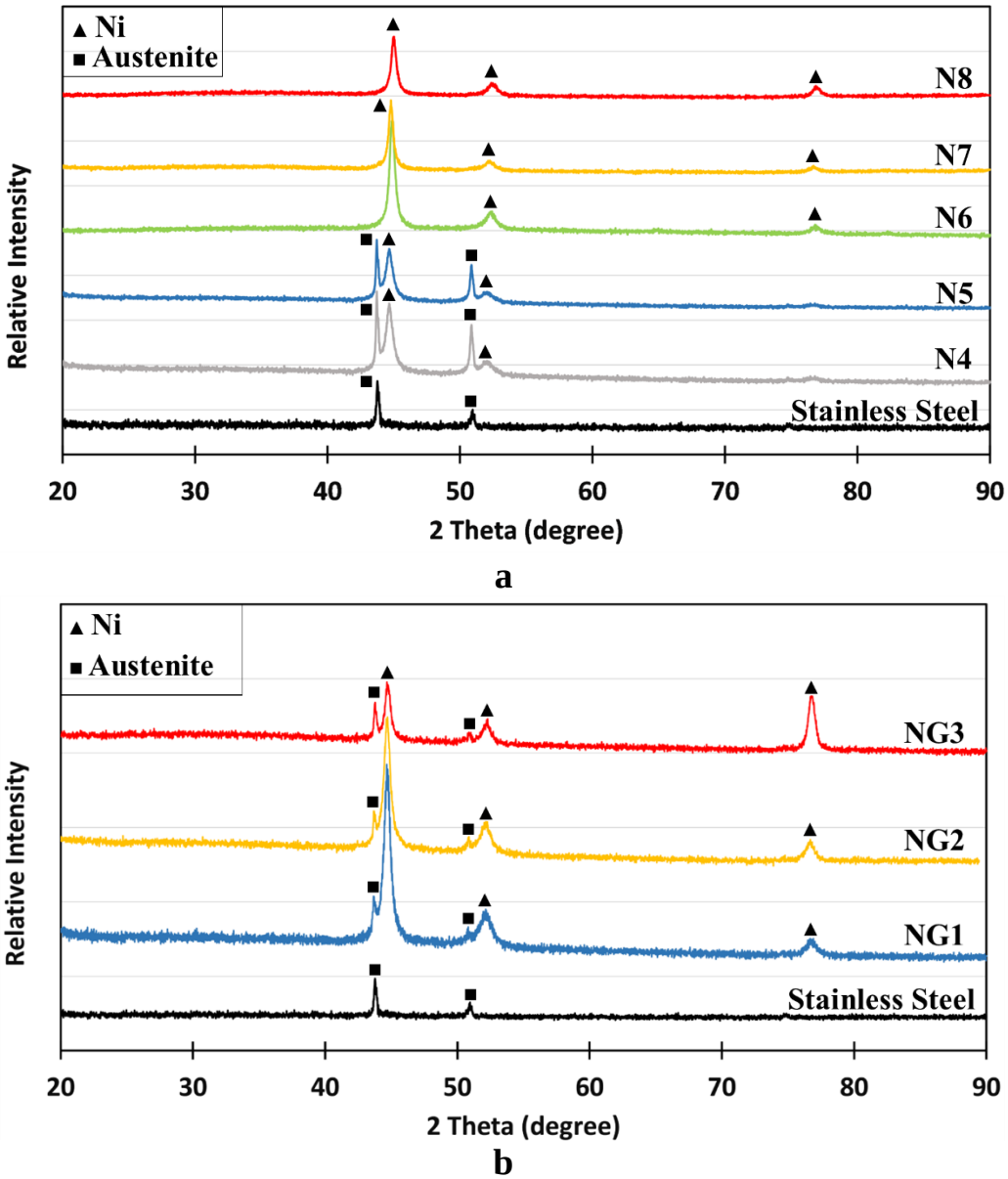


Figure 6.4. Typical XRD patterns of; a) Ni coatings, b) NiGO coatings.

XRD patterns of Ni coatings deposited at lower plating voltages (N4 and N5 in Figure 6.4a), where the coating thickness was less than 3 microns, revealed the primary Ni peaks with

additional peaks corresponding to the austenite phase of the stainless steel substrate. This indicates that the X-rays penetrated through the thin Ni coatings, reflecting the presence of both Ni and austenite. In contrast, for the coatings deposited at higher voltages (N6, N7, and N8), a strong Ni peak at approximately 44º, along with weaker Ni peaks, and no peaks corresponding to the austenite substrate were observed.

The XRD analysis of NiGO coatings revealed that the main Ni peaks appear at the same 2 theta positions as those observed for the pure Ni coatings; however, the intensities of these peaks are notably lower. This indicates that the incorporation of graphene oxide (GO) into the Ni matrix disrupts the regular arrangement of Ni atoms, leading to a decrease in peak intensity [243]. Additionally, unlike the pure Ni coatings (N6, N7, and N8), which showed no reflection of the austenite phase, NiGO coatings exhibited weak austenite peaks regardless of the GO concentration.

Average roughness (Ra) and root mean square roughness (Rq) were measured for each sample, and the results are given in Figure 6.5. It can be said that the surface roughness changed significantly with the applied voltage. As seen in Figure 6.5a, the lowest surface roughness was observed for sample N6 with Ra≈0.7 μm and Rq≈0.17, whereas the highest surface roughness was measured for sample N4 with Ra≈1.6 μm and Rq≈0.34 μm. As known, the deposition rate is quite slow at lower voltages, which results in the formation of larger and irregular Ni grains, increasing the surface roughness. On the other hand, the adhesion of rapidly nucleating Ni particles to the substrate does not occur at the desired quality at high deposition rates, which causes partial peeling, which also increases the surface roughness as seen in N7 and N8 samples. Additionally, high-speed deposition increases the internal stress within the coating, causing degradation of the coating, and leading to an increase in the surface roughness.

On NiGO coating samples, it was observed that the surface roughness increased proportionally depending on the increasing GO concentration (see Figure 6.5b). This indicates the presence of

GO in the coating as the regular accumulation of Ni was disrupted by the GO sheets, which increased the surface roughness.

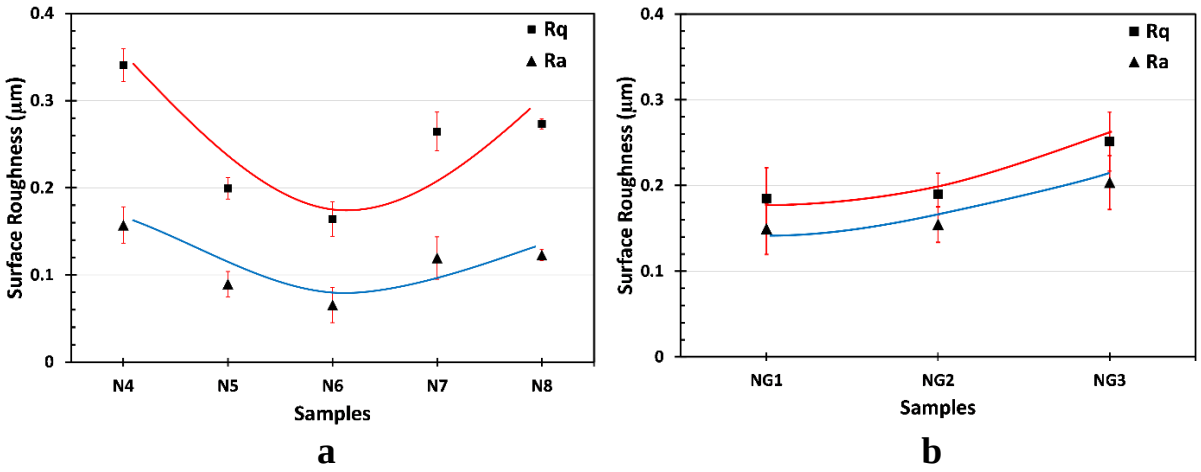


Figure 6.5. Surface roughness of the produced; a) Ni coatings, b) NiGO coatings.

*6.4.1.2 Mechanical properties*

The hardness for the Ni-coated samples (N4 to N8 in Figure 6.6a) demonstrated significant variation with the applied voltage during electroplating. Sample N6 exhibited the highest hardness at almost 498 HV, with minimal variation, while the lowest value was obtained for the N7 sample at around 472 HV, indicating that the worsening coating quality at high voltages also decreased the hardness of the coating. It is understood that the optimal plating voltage of 6V enhances mechanical properties, likely due to finer grain structure and improved uniformity of the coating.

In contrast, for the NiGO-coated samples (NG1 to NG3 in Figure 6.6b), a clear trend of increasing hardness with higher GO concentrations was seen, and the highest value of 482 HV was measured for sample NG3. Even though this enhancement in hardness can be attributed to the reinforcing effect of GO within the Ni matrix by impeding dislocation movement, the most desired hardness was achieved for sample N6.

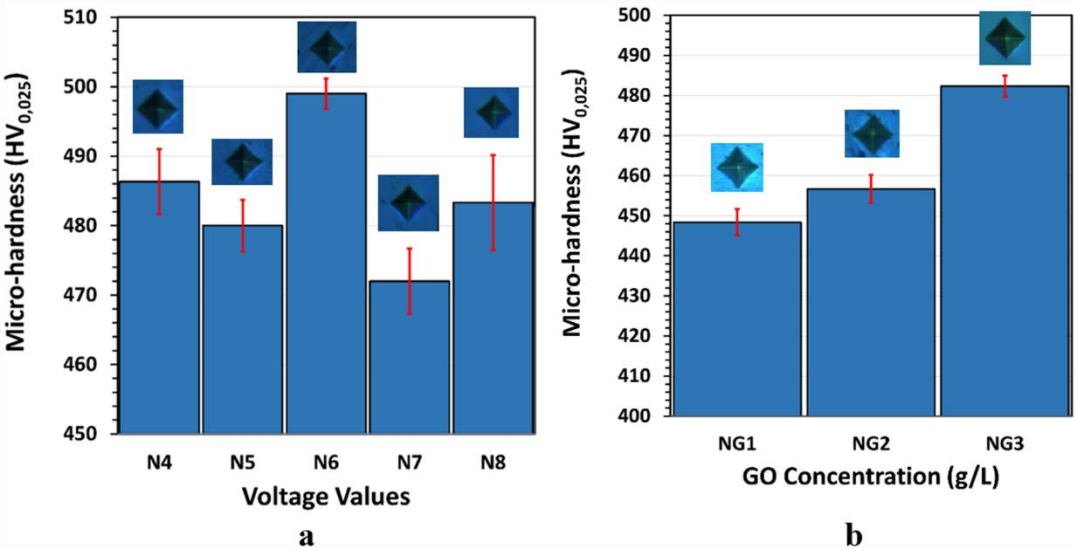


Figure 6.6. Microhardness of the produced; a) Ni coatings, b) NiGO coatings.

To improve and test the adhesion and mechanical properties of the coatings, annealing was employed on the samples N6 and NG3. The hardness and phase constitution of the annealed samples were analysed and the results were given in Figure 6.7 and Figure 6.8, respectively. A significant decrease in hardness for both N6 and NG3 samples was observed at 300°C, with further reductions at 400°C, reaching the lowest values at 500°C, because of the recrystallisation of Ni (330°C). This reduction is likely due to the annealing-induced grain growth and reduction in internal stresses. However, hardness began to increase at 600°C, 700°C, and 800°C, which can be attributed to the formation of nickel oxide (NiO), as confirmed by the XRD results of the annealed samples N6 and NG3 given in Figure 6.8a&b. XRD patterns of N6 and NG3 annealed at 600°C and above identified the oxidised austenite ($NiFe_2O_4$) coming from the substrate, indicating the coatings were degraded during the annealing.

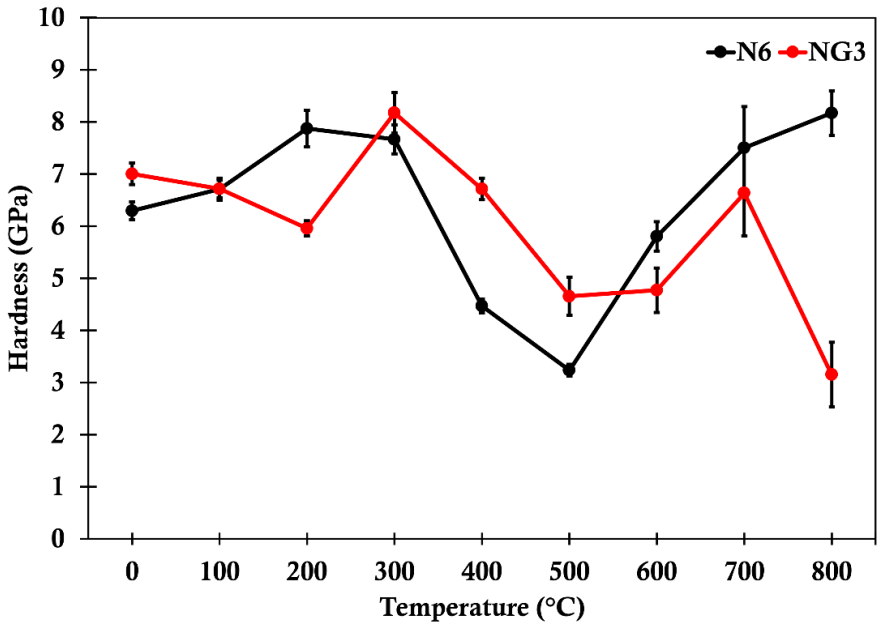


Figure 6.7. Nano-indentation results of the annealed N6 and NG3 samples.

As known, the region where hardness was measured is also crucial, as it directly influences the observed values. For the NG3 sample, a significant drop in hardness at 800°C was noted, possibly due to coating failure and delamination. This also indicates that while annealing can improve hardness through oxide formation, excessive temperatures may compromise coating integrity, particularly in composite samples where differential thermal expansion and microstructural changes can lead to mechanical failure.

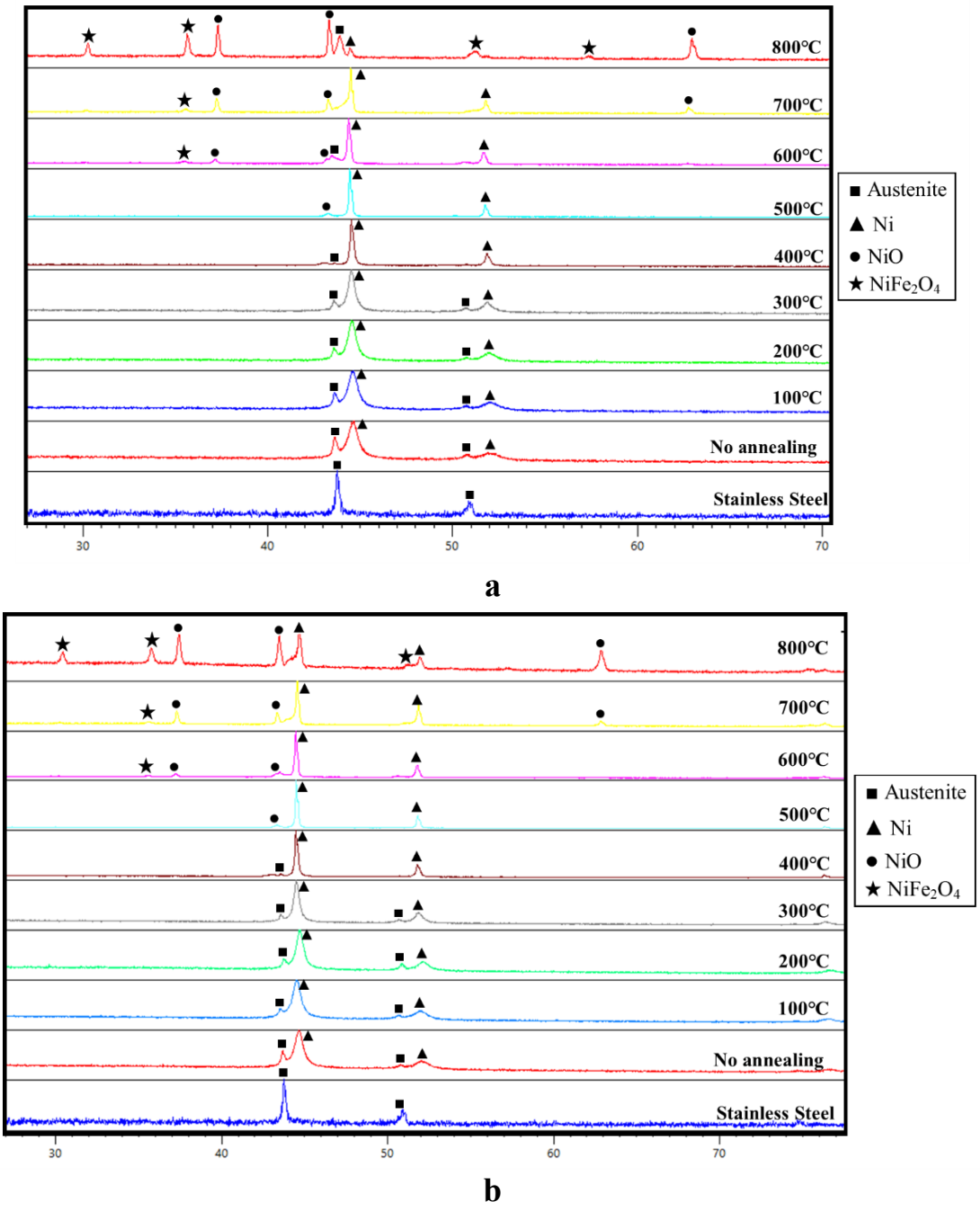


Figure 6.8. Typical XRD patterns of the annealed a) N6 sample, b) NG3 sample

The scratch test results presented in Figure 6.9a compared the frictional performance of the coating samples of N6 and NG3 under increasing load and provided insight into the adhesion of the coatings. The analysis revealed no significant differences in friction between the two samples. However, surface examination on the scratched region displayed more extensive degradation for sample N6 with deeper scratches and partial peeling (Figure 6.9b), in contrast

to NG3 (Figure 6.9c), indicating the contribution of GO incorporation to the adhesion of the coating to the substrate. These findings are similar to that of the repeated stretch test on the separate Ni/NiGO coating samples.

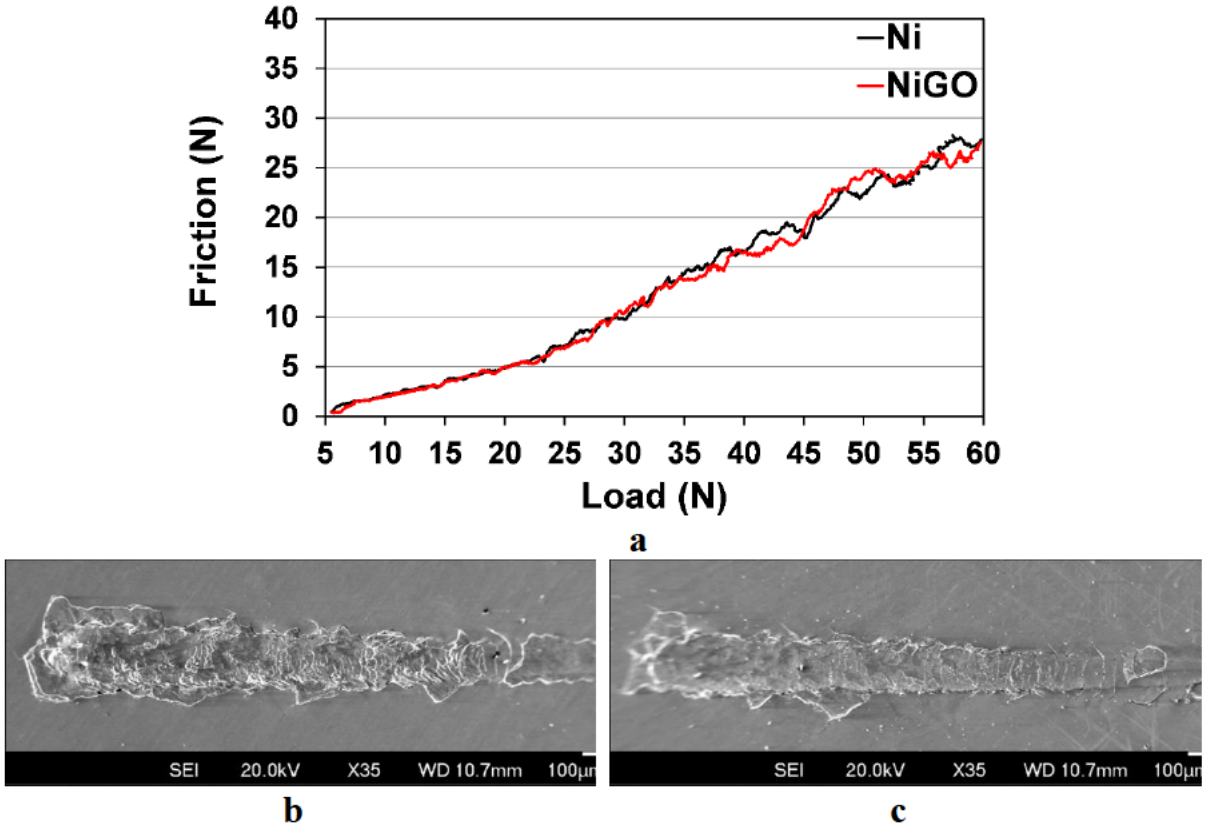


Figure 6.9. Scratch test on the produced coatings, a) friction along the load applied, b) scratched surface of the N6 sample, b) scratched surface of the NG3 sample.

*6.4.1.3 Sheet and interfacial contact resistances*

The sheet resistances for the Ni and NiGO coating samples are shown in Figure 6.10. For the Ni coating samples (Figure 6.10a), N4 exhibited the highest sheet resistance at approximately 248 ohms per square, with significant variability, possibly because of the uniformity of the less-thickened Ni layer. Similar results were obtained for the N5 sample with a large but relatively smaller error bar than N4. The sheet resistance of the N6, N7, and N8 samples displayed similarity, with considerably greater consistency. It is known that thinner coatings generally have higher sheet resistance due to reduced conductive pathways and increased influence of

surface roughness, defects and substrate contribution. The thicker N6, N7, and N8 coatings likely contributed to their lower and more consistent sheet resistance values. It should be noted that the measurements were taken from the undegraded regions of the N7 and N8 samples.

In contrast, the NiGO coating samples (NG1, NG2, and NG3) all demonstrated similar sheet resistance values of approximately 223 ohms per square, with highly reliable and consistent measurements (Figure 6.10b).

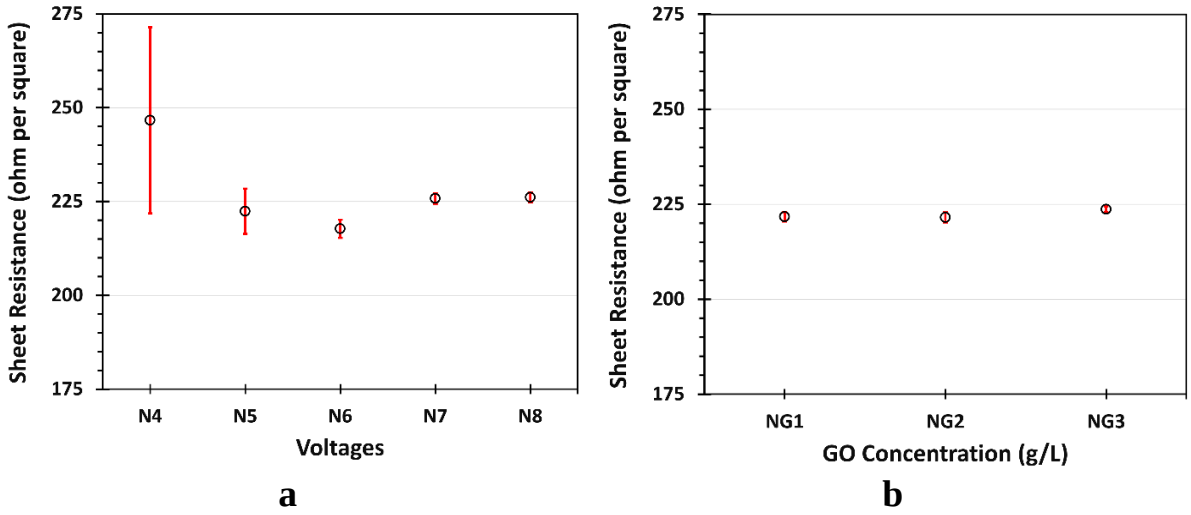


Figure 6.10. The sheet resistance of; a) Ni coatings, b) NiGO coatings

The interfacial contact resistance (ICR) for the N6 and NG3 samples is displayed in Figure 6.11. For both samples, the ICR was observed to gradually decrease with increasing load. This trend is due to the enhanced contact pressure, which minimizes gaps and increases the real contact area, thereby reducing the resistance. The results also reveal that the ICR of the NG3 sample is consistently higher than that of the N6 sample across a range of loads from 30N to 180N. It may be because the adhesion quality of NiGO coatings (for the NG3 sample) may not be as robust as that of the N6 sample. The increased resistance can be attributed to potential gaps in the contact region, which impede effective electrical conduction. Additionally, the presence of graphene oxide (GO) in NG3 might introduce interfacial defects or irregularities that contribute to higher ICR values.

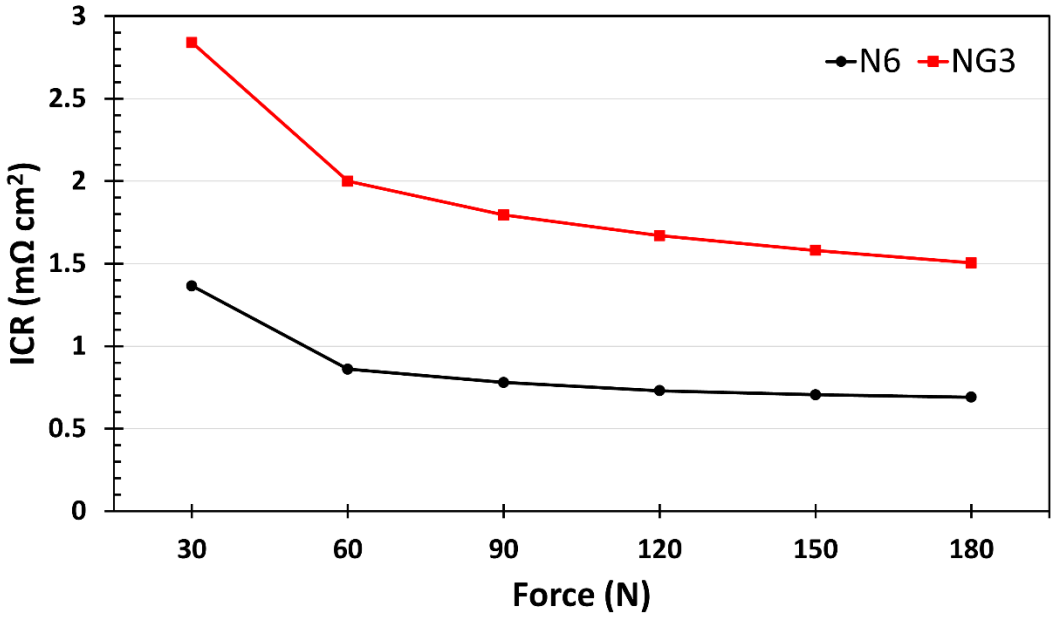


Figure 6.11. The interfacial contact resistance of the N6 and NG3 samples

### *6.4.2 Ni coating on the P-type (Zr,Ti)Co(Sn,Sb) TE material*

The result of the detailed characterisation of Ni and NiGO coatings deposited on stainless steel implied that the deposition of pure Ni coatings without GO addition on P-type (Zr,Ti)Co(Sn,Sb) thermoelectric materials would be sufficient to obtain the desired contact properties as evidenced by the that the increase in electrical conductivity obtained in the optimised Ni coating (N6) are almost similar to that of NiGO The fact that there is no significant difference in the microstructure and properties of the optimised N6 and NG3 samples suggested that the use of GO is unnecessary, considering the production cost. For this reason, metallising Ni coatings were applied to the interface of P-type (Zr,Ti)Co(Sn,Sb) thermoelectric materials using the optimum voltage value (6V) and their oxidation resistance at high temperatures was characterised.

#### *6.4.2.1 Coating structure*

Macro images of the uncoated and Ni-coated P-type material presented in Figure 6.12a compared the sample surfaces before and after the coating process. It can be seen that the Ni

was successfully deposited onto the P-type material, with no evidence of peeling or degradation during the plating process. The surface of the Ni-plated sample exhibited a shiny appearance, indicating a smooth and uniform coating. Cross-sectional analysis further confirmed the presence of the Ni layer on the substrate (Figure 6.12b), with a thickness of approximately 6 microns. The coating displays a layer-by-layer structure, similar to the Ni and NiGO coatings observed on stainless steel substrates. This structural uniformity suggests effective deposition and strong adhesion, contributing to the mechanical and functional integrity of the coated material.

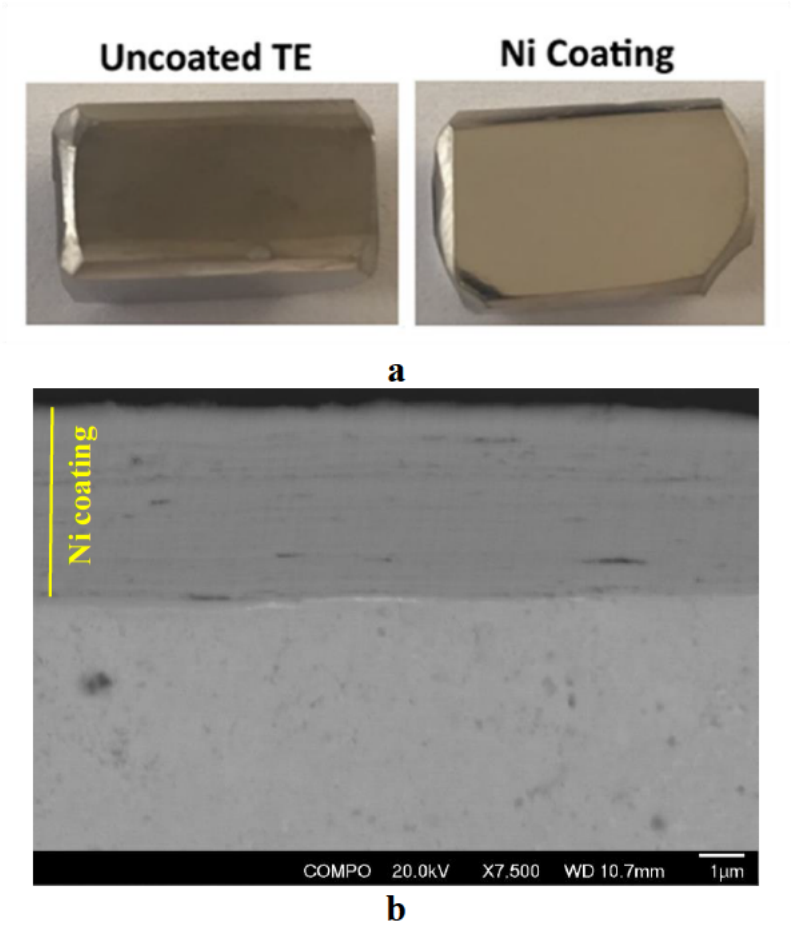


Figure 6.12. a) Macro images of the deposited coatings on the P-type TE material compared with the uncoated sample, and b) cross-sectional backscattered electron microscope (BEI) image of the coating layer.

*6.4.2.2 Thermal stability*

XRD patterns of as-received P-type TE material were compared with the Ni-plated samples before and after oxidation testing, as displayed in Figure 6.13. mainly consisting of a half-Heusler phase of (Zr,Ti)Co(Sn,Sb) with high-intensity peaks. In addition, some weak traces corresponding to the Sb phase were also detected. As expected, high-intensity Ni peaks were identified for the Ni-plated sample. After oxidation, in addition to the Ni peaks detected for the NP sample, very weak peaks corresponding to NiO were identified, indicating the formation of a superficial oxide layer on the sample surfaces after oxidation. It was also seen that the full width at half maximum (FWHM) of the Ni peaks considerably decreased after oxidation, implying that the Ni grain size on the sample became larger with the oxidation.

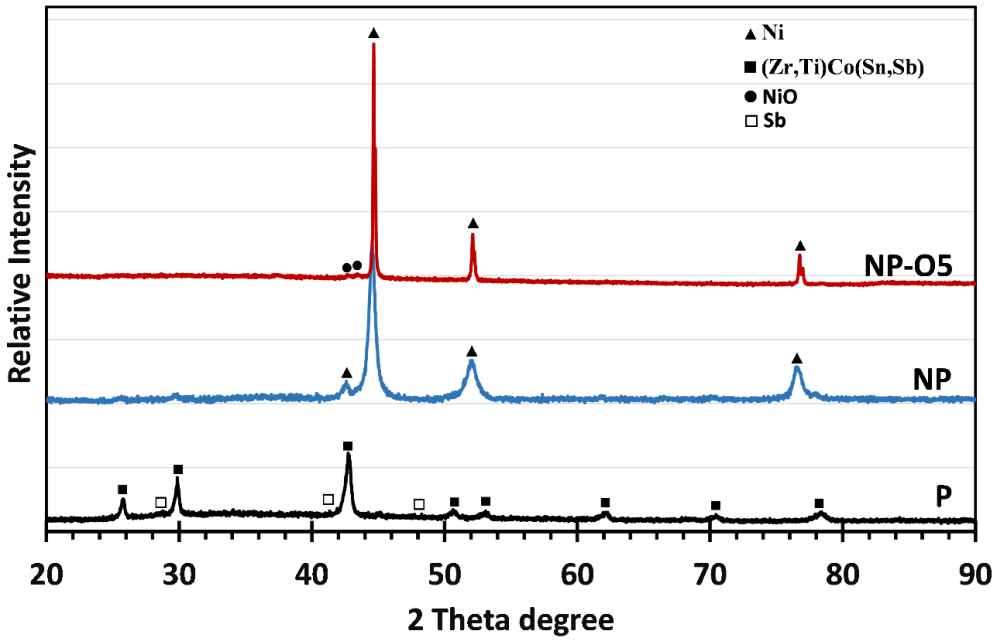


Figure 6.13. XRD patterns of NP and NP-O5 samples compared with the as-received P sample.

The SEM and EDX analyses were used to characterise the surface of the NP-O5 sample, and the obtained images and data were presented in Figure 6.14. As shown in Figure 6.14a, some part of the Ni coating was bubbled and several small-sized oxides were formed around these

bubble-likefeatures, which are also rich in oxygen (see Figure 6.14c). However, the cross-sectional SEM image of the NP-O5 sample shows that bubble-like growths are formed on the top surface of the coating only (Figure 6.14b), indicating that the majority of the Ni coating is still on the sample. It is also seen that the oxygen quantity on the top surface of the coating is higher than that at the interface (Figure 6.14c), which is in line with the XRD results given in Figure 6.13.

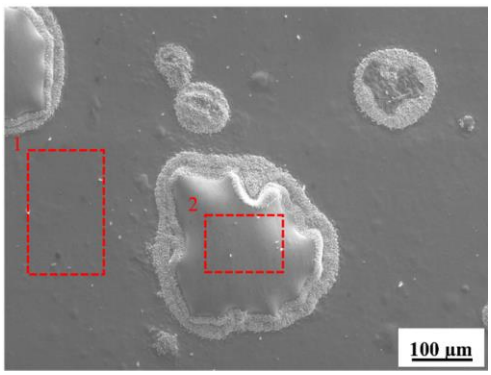


a

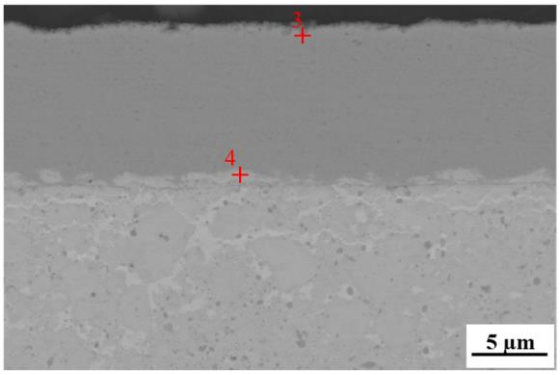


b

| Coating | Analysis | Elements (at. %) | | | | |
|---|---|---|---|---|---|---|
| | | Ni | O | Sn | Sb | Others |
| Ni | Spectrum 1 | 68.9 | 31.1 | - | - | - |
| | Spectrum 2 | 66.2 | 33.8 | - | - | - |
| | Spectrum 3 | 83.4 | 16.6 | - | - | - |
| | Spectrum 4 | 69.2 | 6.7 | 16.8 | 2.8 | 4.5 |

c

Figure 6.14. (a) Surface morphology and (b) cross-section of the Ni coating samples after oxidation testing, and (c) EDX analyses on the surface and cross-section of the oxidised Ni coating.

The element distribution was investigated on the cross-section of the NP-O5 sample by the EDX elemental mapping and the obtained results are presented in Figure 6.15. It can be seen that an oxide layer formed on the top surface of the coating. The formation of the superficial oxide layer significantly blocked oxygen diffusion into the coating. It is also noteworthy that no elemental diffusion between the coating and substrate at the interface was observed. As previously mentioned, the substrate material contains Sn and Sb, which can sublimate at

moderate and high temperatures. Fortunately, the Ni coating prevented sublimation of those elements and provided microstructural stability at 500℃ for 10 hours.

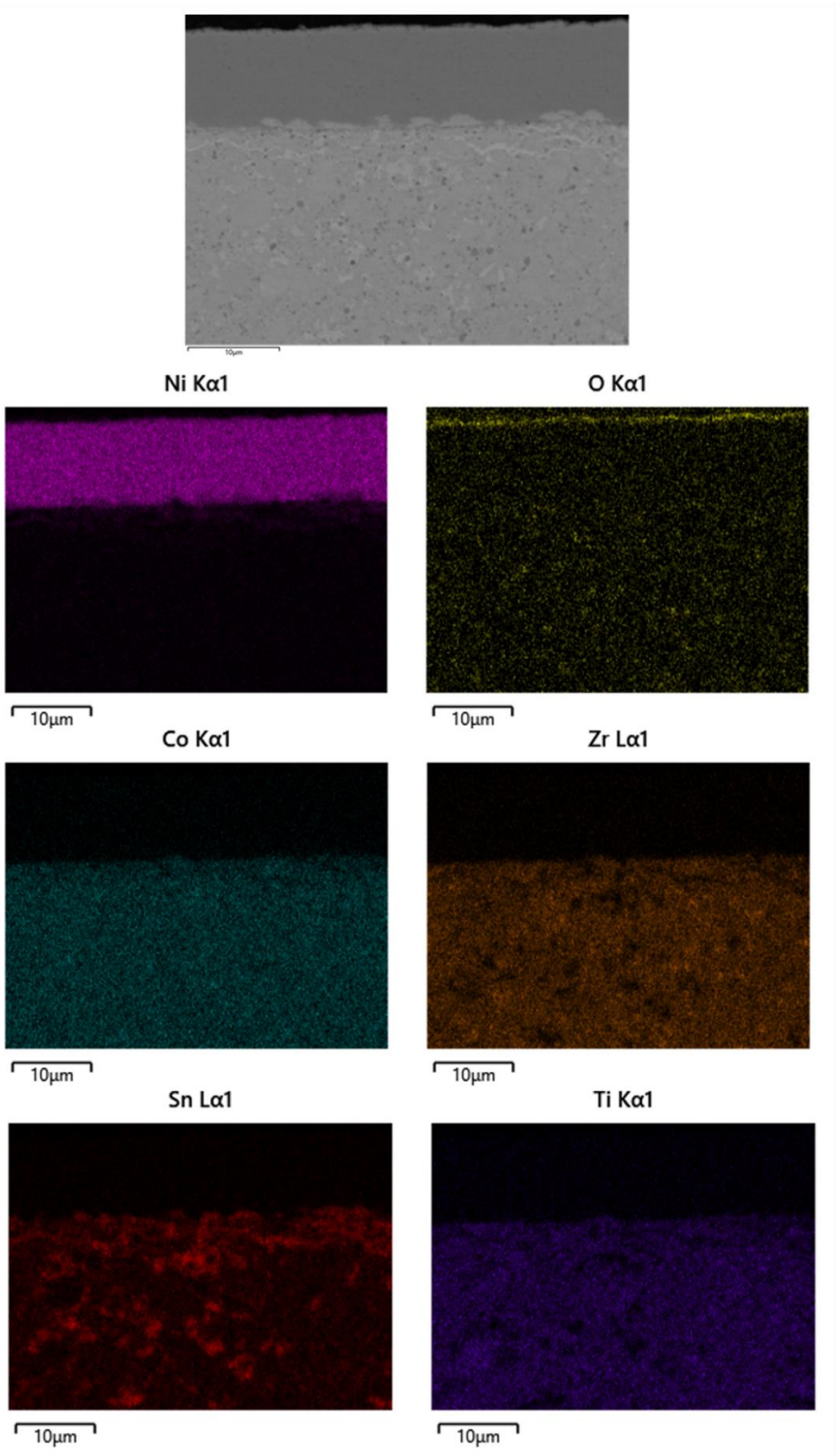


Figure 6.15. Elements mapping of the cross-section view of the oxidised Ni coating

## 6.5 Conclusions

In this study, the Ni and NiGO metallising coatings were deposited on the stainless steel and P-type (Zr,Ti)Co(Sn,Sb) thermoelectric material by the low-cost electro-brush plating technique. The produced coatings were characterised in detail to determine the optimum contact layer for a high-performance P-type half-Heusler thermoelectric material. The experimental findings can be concluded as follows:

- The Ni and NiGO coatings are successfully deposited on the stainless steel and the conductive P-type thermoelectric material by the electro-brush plating technique. The applied voltage is crucial to get a high-quality layer with no degradation or peeling during the plating.
- GO is well incorporated into the Ni coatings. However, the optimisation study showed that there was no significant reduction in the sheet resistance, interfacial contact resistance and hardness of the NiGO layer as compared with Ni layers.
- The layer-by-layer structure of the Ni coating deposited on the P-type material was the same as on the stainless steel. The coating was well-adhered to the TE substrate and no peeling was observed even after oxidation.
- The Ni layer provided microstructural stability in the TE materials after oxidation, indicating its protectivity against oxidation and sublimation at 500°C. The formation of a very thin nickel oxide layer on the surface of the coating prevented oxygen diffusion into the coating and prevented further oxidation.

The outcome of the study suggests that the interfacial contact properties of the P-type (Zr,Ti)Co(Sn,Sb) TE material can be enhanced by the deposition of highly conductive and oxidation-protective nickel layer by cost-effective and easy-to-apply electro-brush plating technique. The future study will focus on both the deposition of Ni coating on different types

of TE materials to improve their contact properties and the production of high-quality nanocomposite coatings by using graphene oxide.

# Chapter 7 Characterisation of magnetron sputtered BiTe based thermoelectric thin film

* This chapter has been published in the Nanomaterials.

[1]Zhang, Z., [1]**Gurtaran, M.,** [1]Li, X., [2]Un, H. I., [3]Qin, Y., & [1]Dong, H. (2023). Characterization of magnetron sputtered BiTe-based thermoelectric thin films. Nanomaterials, 13(1), 208.

1- School of Metallurgy and Materials, University of Birmingham, Birmingham, UK
2- Cavendish Laboratory, University of Cambridge, Cambridge, UK
3- Design, Manufacturing and Engineering Management, University of Strathclyde, Glasgow, UK

**Acknowledge of Collaborative Work:**

**Mikdat Gurtaran:** Investigation, Validation; Zhenxue Zhang: Writing – Original Draft Preparation, Investigation, Validation, Methodology; Hio-Leng Un: Investigation; Xiaoying Li: Writing – Review & Editing, Formal Analysis; Yi Qin: Funding acquisition; Hanshan Dong: Conceptualization, Writing – Review & Editing, Supervision, Funding acquisition.

## 7.1 Abstract

Thermoelectric (TE) technology attracts much attention due to it can convert thermal energy into electricity and vice versa. Thin-film TE materials can be synthesised on different kinds of substrates, which offer the possibility of the control of microstructure and composition to higher TE power, as well as the development of novel TE devices meeting flexible and miniature requirements. In this work, we use magnetron sputtering to deposit N-type and P-type BiTe-based thin films on silicon, glass and Kapton HN polyimide foil. Their morphology, microstructure and phase constituents were studied by SEM/EDX, XRD and TEM. The electrical conductivity, thermal conductivity, as well as Seebeck coefficient of the thin film were measured by a special in-plane advanced test system. The output of electrical power (open-circuit voltage and electric current) of the thin film was measured by an in-house apparatus at different temperature gradients. The impact of deposition parameters and the thickness, width and length of the thin film on the power output was also investigated for optimizing the thin-film flexible TE device to harvest thermal energy.

## 7.2 Introduction

In the past decades, extensive research on renewable energy has witnessed a significant advance in harvesting thermal energy into electricity via different pathways to maximise the Seebeck coefficient (S), the electrical conductivity (σ), as well as the reduction of the thermal conductivity (k) [244]. The progress on the conventional heavy atom doped semiconductors, such as $Bi_2Te_3$, PbTe, Si–Ge or Te–Ag–Ge–Sb has resulted in increased thermoelectric figure of merit (zT) which makes the technology more efficient in producing power [245]. To overcome the deficit of rare elements like tellurium and avoid hazardous elements like lead, alternative materials, such as Bismuth Sulphide ($Bi_2S_3$) [246], Tin Selenide (SnSe) [247] and Magnesium Silicon-based new materials [248], have attracted much attention, and higher performance reports emerge regularly. However, properties of bulk TE materials are

determined primarily by composition and microstructure, which limits the usage of thermoelectric energy conversion to niche applications. Furthermore, bulk TE materials are limited by shape and size, which restricted the application in the area of intelligent and flexible TE devices. In contrast, thin films technology has advantage in controlling the composition, thickness and microstructure, and higher TE power can be realized by quantum effects and band gap engineering using reduced-dimensionality materials [249]. Nanosized structure results in the presence of a large number of interfaces (grain boundaries), which may effectively scatter phonons and thus reduce the thermal conductivity considerably and lead to a substantial increase in thermopower [250]. In the meantime, di-versified substrates, for example, polymer, can be used to meet the flexible, lightweight and miniature requirements [251].

Different film growth methods based on molecular-beam epitaxy (MBE) [252], metalorganic chemical vapour deposition (MOCVD) [253] and flash evaporation [254] have been used to grow single layers and superlattices on various substrates. Evaporation is not ap-propriate for compound film deposition like Bismuth telluride, as the vapour pressure of Te is as much as 104 times higher than those of Bi and Sb at the melting points. CVD technique often needs a higher temperature, while MBE has a very low deposition rate which restricts its application. Magnetron sputtering is a versatile technique with a high deposition efficiency, and it can deposit conductible materials as well as insulative materials by using different powers like direct current (DC), radio frequency (RF) or pulsed DC power. Therefore, the technique has stimulated the abundant interest of different groups to study various materials for high power output as shown in Table 7.1.

In this paper, we used an unbalanced close-field magnetron sputtering ion plating technique to deposit nano-structured N-type and P-type BiTe-based thin films on silicon, glass and Kapton HN polyimide foil. By adjusting the deposition parameters to modify the morphology,

microstructure and phase constituents, we have managed to optimize their thermoelectric properties.

Table 7.1. Thermoelectric films produced by magnetron sputtering techniques.

| TE film | Substrate | MS Parameters | Properties | Ref. |
|---|---|---|---|---|
| $Sb_2Te_3$ | Polyimide | RF | TPF: $1.07\times10^{-4}$ $Wm^{-1}K^{-2}$ | [255] |
| $Sb_2Te_3$ | Polyimide | DC, deposited at 473 °K | TPF: $6.0\times10^{-4}$ $Wm^{-1}K^{-2}$ | [256] |
| $Bi_2Te_3$ | $SiO_2$/Si | RF | TPF: $3\times10^{-4}Wm^{-1}K^{-2}$ at 498°K | [257] |
| $Bi_2Te_3$ | Glass, Alumina, Sapphire, and Polyimide | DC | SC: maximum $-1.63\times10^{-4}$W/K on glass. | [258] |
| $Bi_2Te_3$ | Polyimide | RF/DC | TPF: $3.5\times10^{-3}$ $Wm^{-1}K^{-2}$ at 558°K with DC power | [259] |
| $Sb_2Te_3$ $Bi_2Te_3$ | Glass | RF | TPF: $1.27\times10^{-3}$ $Wm^{-1}K^{-2}$ for $Sb_2Te_3$ at RT, and $1.02\times10^{-3}$ $Wm^{-1}K^{-2}$ for $Bi_2Te_3$ at 573°K | [260] |
| Ag–Sb–Te (AST) | Soda-lime glass and $SiO_2$/Si | DC | $SiO_2$/Si wafer has better results with annealing at 773 °K. | [261] |
| $Ge_2Sb_2Te_5$ | Soda-lime Glass (523°K-723°K) | Pulsed DC | TPF: $0.77\times10^{-3}$ $Wm^{-1}K^{-2}$ at 673°K | [262] |
| $Zn_xSb_y$ | flexible polyimide | RF | TPF: $2.35\times10^{-3}$ $Wm^{-1}K^{-2}$ | [263] |
| ScN | MgO (1123°K) | DC in $Ar/N_2$ | TPF: $3.3\times10^{-3}$ $Wm^{-1}K^{-2}$ at 800°K | [264] |
| $Cu_2Se$ | Copper (Low Temperature) | Pulsed Hybrid Technique | TPF: $1.1\times10^{-3}$ $Wm^{-1}K^{-2}$ $\kappa = 0.8 \pm 0.1$ $Wm^{-1}K^{-1}$ | [265] |
| SnSe | Glass/Fused Silica | RF | TPF: $1.4\times10^{-4}$ $Wm^{-1}K^{-2}$ at 575°K | [266, 267] |
| $Mg_2Sn$ | Glass | RF | TPF: $8.5\times10^{-4}$ $Wm^{-1}K^{-2}$ at 519°K | [268] |
| $Mg_2Si$ | Polyimide | RF | TPF: $3.3\times10^{-5}$ $Wm^{-1}K^{-2}$ at 710°K | [269] |
| Ge–Au | Glass | Power of 320 W | Thermal conductivity: 1.1 $Wm^{-1}K^{-1}$ at 300°K | [270] |
| $Zn_{1-x}Ag_xSb$ | Fused Silica | DC | TPF: $1.49\times10^{-3}$ $Wm^{-1}K^{-2}$ at525 °K | [271] |
| Amorphous Ga–Sn–O | Quartz | RF | TPF: $1.47\times10^{-4}$ $Wm^{-1}K^{-2}$ at 397°K | [272] |
| Al-doped Zinc Oxide (AZO) | Soda-lime Glass | RF | Maximum zT value of 0.019 at 640°K | [273] |
| $Co_xSb_y$ | Polyimide | RF | Maximum TPF: $1.71\times10^{-4}$ $Wm^{-1}K^{-2}$ | [274] |

DC: direct current, RF: radio frequency, TPF: thermoelectric power factor, PF: power factor

We have tested the electrical conductivity, thermal conductivity, as well as Seebeck coefficient of the sputter deposited thin films using a dedicated in-plane test equipment. We have also used a home designed device to examine the output of electrical power (open-circuit voltage and

electric current) of the thin film on Kapton polymer substrate to optimize the deposition parameters and the thickness, width and length of the thin film in order to design a device on flexible substrate. Clearly, nano-structuring materials become indispensable in the studies of thermoelectric function in consumer electronics [275], and this work offers the insights into the fabrication of nanoscale thin-film thermoelectric flexible device.

## 7.3 Materials and methods

### *7.3.1 Thin film fabrication*

In this work, the 99.99% purity of targets with a nominal composition of $Bi_2Te_3Se$ (N-type) and $BiSb_2Te_3$ (P-type) plates in the size of 200 mm x 100mm x 5mm were bonded on the rectangle copper back plate.

Table 7.2. Sample codes and deposition details

| Sample code | Substrate | Target current (A) | Deposition Time (min) | Thickness (μm) |
|---|---|---|---|---|
| N4 | Si/Chip/Glass | 0.4 | 40 | 2.0 |
| N5 | Si/Chip/Glass | 0.5 | 40 | 2.5 |
| N45 | Si/Chip/Glass | 0.45 | 40 | 2.2 |
| P3 | Si/Glass | 0.3 | 65 | 2.0 |
| P3R | Si/Chip/Glass | 0.3 | 50 | 1.5 |
| P4 | Si/Chip/Glass | 0.4 | 50 | 1.8 |
| P45 | Si/Chip/Glass | 0.45 | 45 | 1.8 |
| P5 | Si/Glass | 0.5 | 45 | 1.9 |
| P6 | Si/Glass | 0.6 | 30 | 1.8 |
| P45K | Kapton | 0.45 | 60 | 2.5 |
| P4K-6mm | Kapton | 0.4 | 50 | 2.0 |
| P4K-12mm | Kapton | 0.4 | 50 | 2.0 |
| N4K-50m | Kapton | 0.4 | 50 | 2.4 |

N3-S, N3-G and N3-K indicate N3 thin film on silicon, glass and Kapton substrate separately.

The thin film was deposited on the glass, silicon wafer, special chip and Kapton polymer substrates in a 4-target Teer Coating Ltd Closed Field Unbalanced Magnetron Sputtering Ion Plater in the direct current mode. A set of films were deposited with currents of 0.3A, 0.4A, 0.45A, 0.5A and 0.6 A at various time. Detailed sample codes to corresponding coating

conditions is listed in Table 7.2. The thickness was measured on the thin film deposited on the glass slide.

### *7.3.2 Characterisation and properties measurement*

A Joel 7000 scanning electron microscope (SEM) equipped with an Oxford Inca energy dispersive X-ray spectroscopy (EDX) detector was used to inspect the surface morphology, cross-sectional microstructure, and elemental information of the thin film. An Inel EQUINOX 3000 (2C) X-ray diffraction (XRD) using Cu-Kα radiation (λ = 0.154056 nm) was used to scan the surface from 20.01 and up to 80° with a step size of 0.02° and counting times of 2 s/step to examine the surface phase constituents. 300 square mesh copper TEM grids (Agar scientific) were clipped to a plate, which was put into the PVD chamber to collect the coatings along the edge of the grids. Transition Electron Microscope (TEM) microstructure characterisation was carried out by Jeol 2100 TEM.

An advanced platform for the in-plane zT measurement was used to measure the thermal electric properties of the thin film. The film was deposited on a special zT Al2O3 (ALD) Au contact Chips for Linseis TFA supplied by SemiMetrics Limited (1 in Figure *7.1*) The chip combines two suspended membrane setups, based on the Völklein geometry for in-plane thermal conductivity measurements with a 4-point Van-der-Pauw measurement setup for the determination of the electrical transport properties [33]. The chip was first covered by a metal mask or tape and film was deposited on specified area as shown in Figure 7.1. After deposition, the mask and tape were removed, and the chip (4) was ready for the test. The Seebeck coefficient is measured using a partly passivated resistance thermometer, located on the bigger membrane. Electrical conductivity, Seebeck coefficient and thermal conductivity were measured at the same time within a temperature range between -150 °C and 250°C.

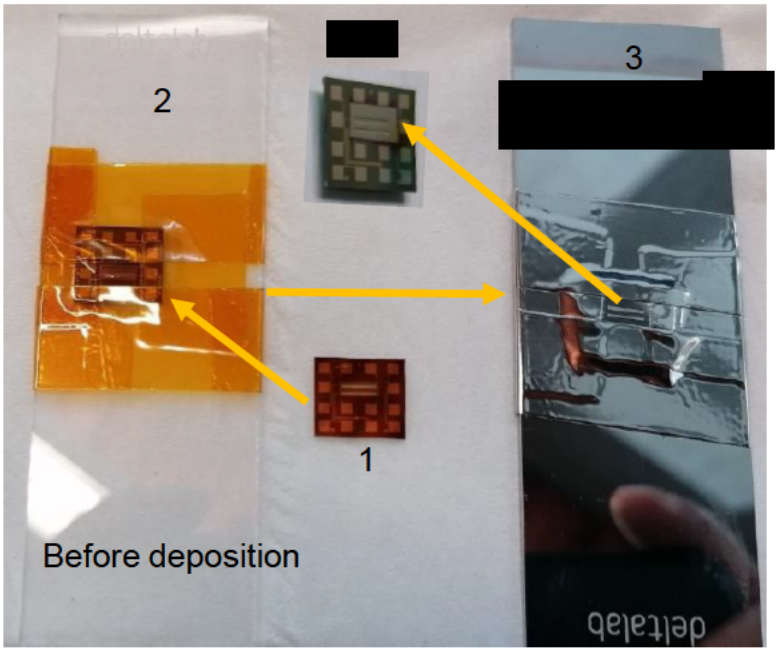


Figure 7.1. The preparation of thin film on chip: 1, the chip; 2, chip with attached shadow masks, 3, chips after deposition; 4, chip with defined thin film ready for test.

### *7.3.3 Output measurement of the active thin layers*

After evaluation, thin film strips with different widths and thicknesses of N-type and P-type layers were deposited on the Kapton substrate to assess their power output as shown in Figure 7.2a. High-temperature conductive copper tape was used to link the strip and create connective points. One side of the strip (i.e. ABCD in Figure 7.2a) was put on a hot plate which act as the heating source. The other side of the strip was left outside of the pan and cooled by naturally flowing air. Two thermocouple tips were buried under the copper tape connecting points at the hot and cold sides separately to monitor the temperature difference. One extra thermocouple tip was put on the hot pan to monitor the temperature of the heating. Two multi-meters were used to monitor the open circuit voltage/ current and electrical resistance of different links like A-1, A-4 or B-2 to assess the output of different configurations of the active layer strips. The temperature of the hot pan can be raised to 200°C and accordingly the tip on the active layer is

about 100°C which can generate a temperature difference up to 80°C. A schematic test apparatus is shown in Figure 7.2b.

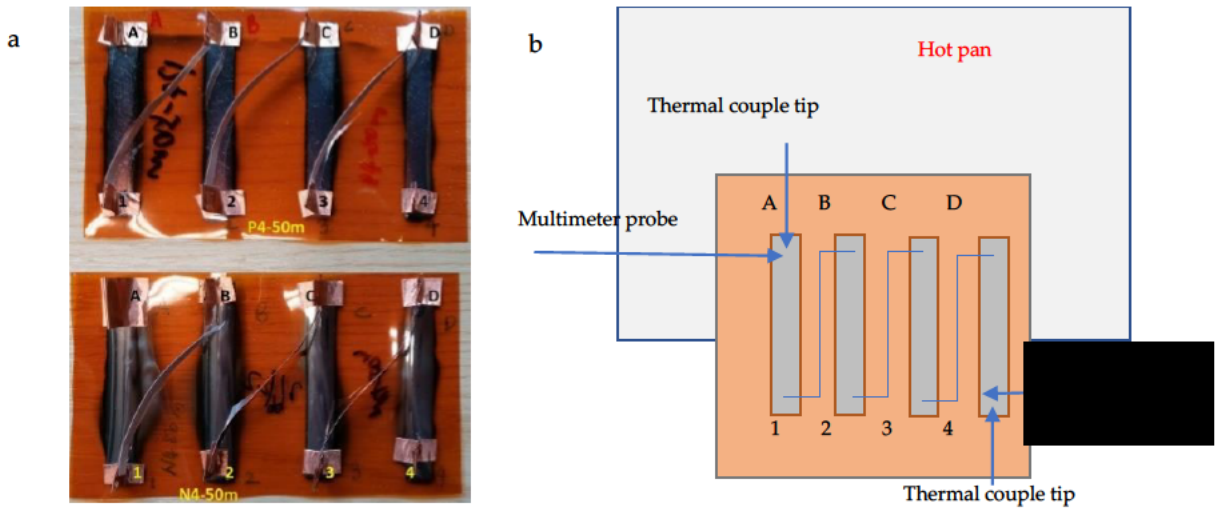


Figure 7.2. Setup for the measurement of the power output of thin film on Kapton substrate (a) the film strips on Kapton substrate, (b) the sketch of the Kapton on a hot pan for test.

## 7.4 Results and discussion

### *7.4.1 Microstructure and phase constituents of the thin films*

The surface morphology and cross-sectional microstructure of the P-type thin film deposited on silicon wafer with different target current have been assessed by SEM (Figure 7.3). Crystallised clusters were formed on the surface after deposition and the size only slightly changed with the increased current from 0.4A to 0.6A (Figure 7.3a/b/c/f). A dense fine columnar structure was formed as seen in the cross-sectional image of P4 and P45 in Figure 7.3d&e. The composition of the coating was identified by EDX and the atomic composition ration of Bi:Sb:Te is about 2:3:4.

As shown in Table 7.2, both the N-type and P-type materials have higher sputter rate, and it took only 40 minutes at 0.4 A to obtain a 2.0 µm thick N-type thin film. The deposition rate for

P-type was slightly slower, as it took 50 minutes at 0.4 A to obtain only 1.8 μm thick film. Increasing the current, the deposition was faster, but higher current than 0.6A led to a spewing of material from the target which adversely impact the film deposition such as resulting in large particles on the surface as evidenced in Figure 7.3f.

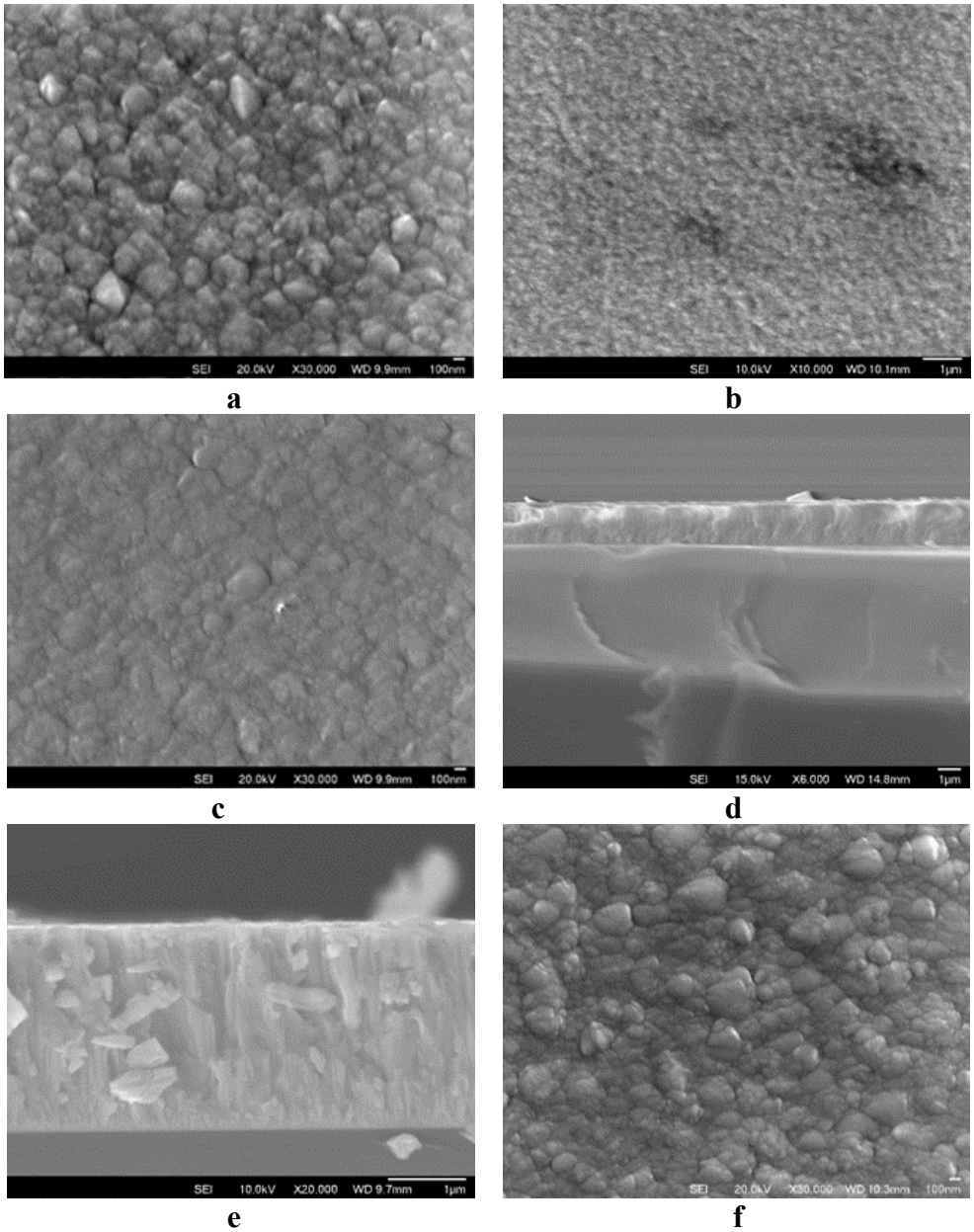


Figure 7.3. P-type $BiSb_2Te_3$ thin film deposited on silicon wafer: (a/d) P4 (b/e) P45, (c)P5, (f) P6.

Typical cross-sectional and surface morphology images of N-type layer on silicon wafer are shown in Figure 7.4a/b. The composition of the thin film was identified by EDX and the atomic composition was calculated as demonstrated in Figure 7.4c/d.

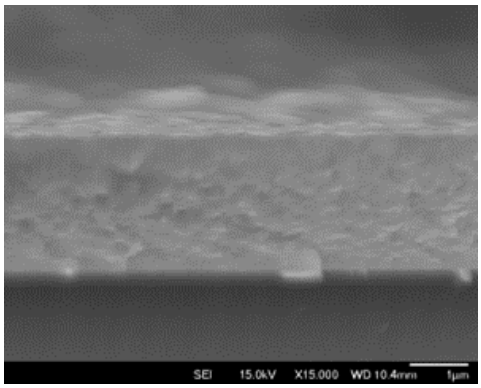


a

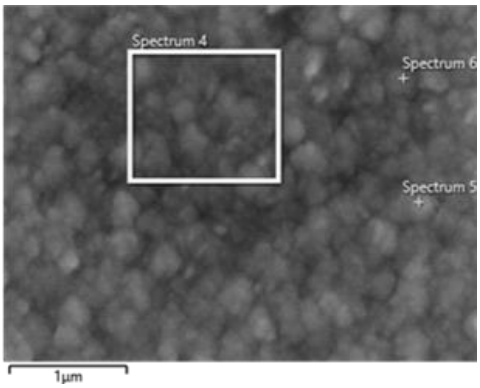


b

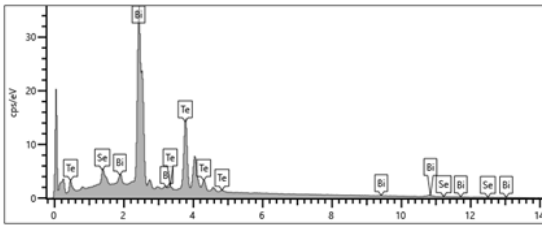


c

| Atomic % | 4 | 5 | 6 | Average |
|---|---|---|---|---|
| Se | 4.15 | 4.28 | 4.09 | 4.17 |
| Te | 50.41 | 49.92 | 50.1 | 50.14 |
| Bi | 45.44 | 45.8 | 45.81 | 45.68 |

d

Figure 7.4. N-type (N4) $Bi_2Te_3Se$ thin film deposited at 0.4A for 40 minutes (a) cross-section; (b) surface; (c ) EDX spectrum of Zone 4 in b and (d) atomic composition of the film.

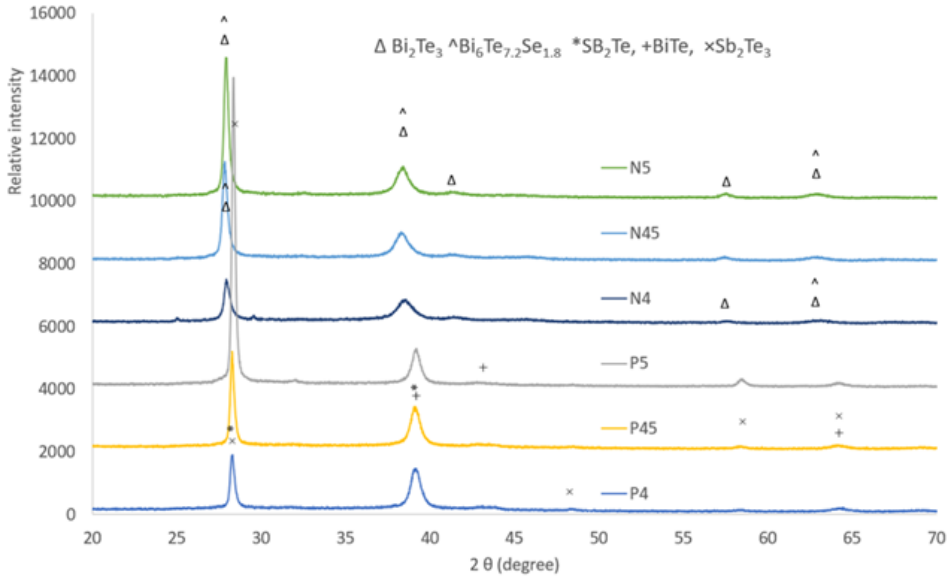


Figure 7.5. XRD comparison of different N-type and P-type layers on silicon substrate

Analysing XRD patterns taken from the N-type and P-type coatings revealed similar phase constituents for each type of the coatings and the representative of the patterns are shown in (Figure 7.5). It can be seen that the N-type coating consists phases of $Bi_2Te$ (PDF:001-085-0439) and $Bi_6Te_{7.2}Se_{1.8}$ (PDF:096-0151-1977). While the P-type coating composed of three phases: $Sb_2Te$ (PDF:0001-0080-1722), BiTe (PDF:0001-0089-4303 and $Sb_2Te_3$ (PDF:0000-0015-0874). For the N-type thin film, the grain size ($B_{i2}Te_3$ at $2\theta=27.89°$) increased with the deposition current, for example, it was about 28 nm for N4 as calculated using Scherrer's equation, while it grew to about 45nm for N5. Similarly, for P-type film, the crystalline size ($Sb_2Te_3$ at $2\theta=28.33°$) increased from about 35 nm (P4) to about 53 nm (P5). TEM observation revealed equiaxed nano-grains with diameters of 40-70nm as shown in Figure 7.6. SAD patterns taken from both P and N-type coatings featured ring patterns, characteristic of nano-structured grains. Indexing of the d-spacing values calculated from the SAD patterns confirmed the phase composition results of XRD analysis, shown in Figure 7.5.

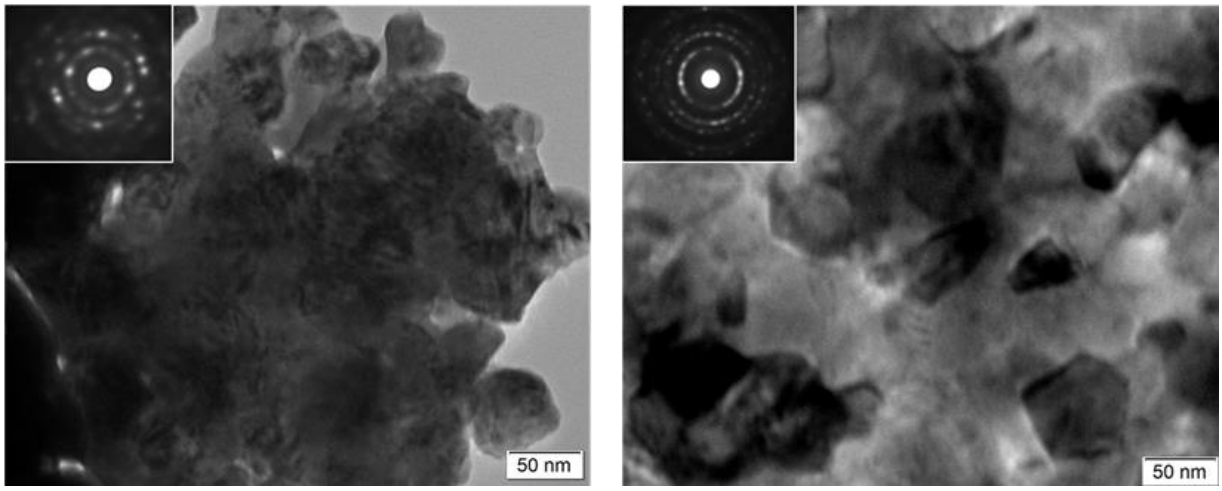


Figure 7.6. TEM microstructure and corresponding SAD patterns of a) N5 and b) P4.

### *7.4.2 Thermoelectrical properties of the thin film*

Thermoelectric properties measurements of the N-type and P-type thin films within the temperature range from -150°C to 230°C were measured simultaneously in an advanced measurement platform.

For all the thin films, the thermal conductivity increased with the temperature as shown in Figure 7.7a. Generally, N-type layer has a higher thermal conductivity value in comparison with the P-type layer at lower temperature range (<150°), this might be due to the grain size effect as the presence of a large number of interfaces (grain boundaries), which may effectively scatter phonons while exerting a minimal effect on the transport of charge carriers[7]. In the meantime, the electrical conductivity of the N-type layers is significantly higher than those of the P-type layer, and it decreased slightly with the temperature increment from -150°C to about 50°C and then increased again till the end of the test (Figure 7.7b).

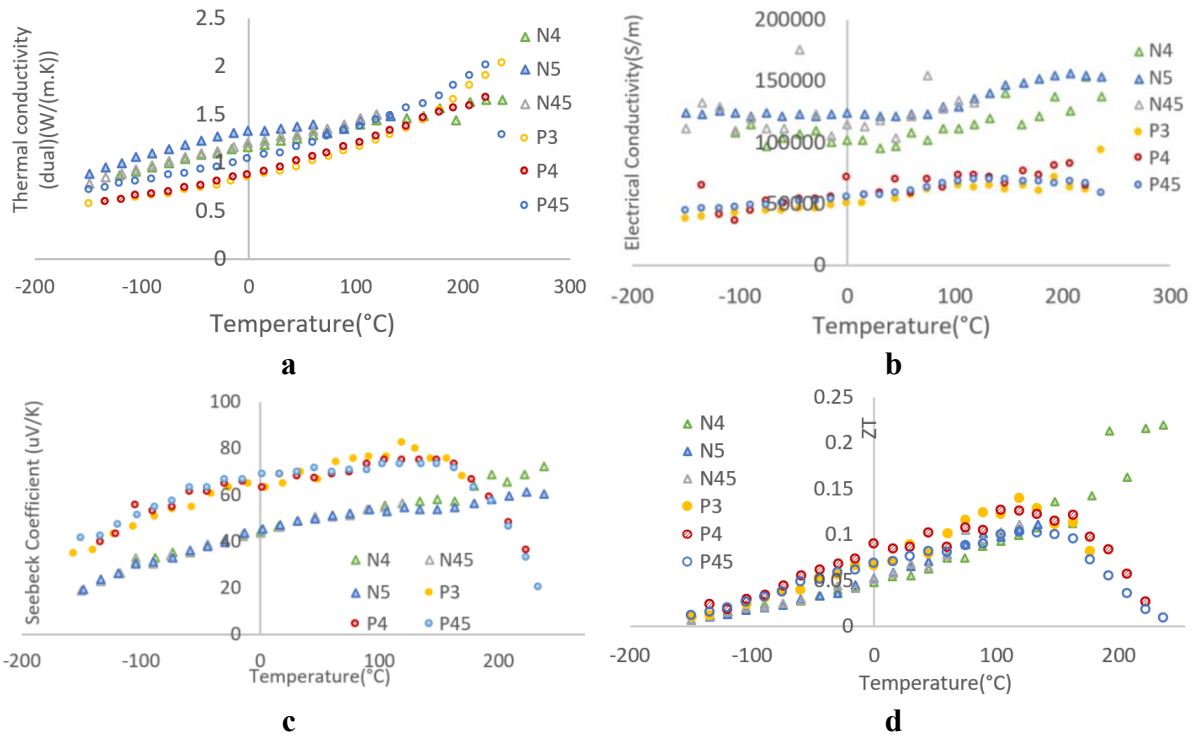


Figure 7.7. Thermal electric properties measurements of the N-type and P-type thin films within the temperature range -150°C–230°C (a) thermal conductivity; (b) electrical conductivity; (c) absolute value change of Seebeck coefficient; and (d) calculated zT value.

For the three P-type thin films, the electrical conductivity kept the trend of climbing with elevated temperature. The Seebeck coefficient of P-type layers improved with temperature till about 140°C and was superior to the N-type layer, however, it drops gradually to a level lower than that of the N-type layer for further rising temperature (Figure 7.7c). Meanwhile, the Seebeck coefficient of N-type layers grew steadily with temperature which performed similarly to the N-type $Bi_2Te_3$ layer prepared at 300C via DC magnetron sputtering [276]. As shown in Figure 7.7d, the calculated zT value has a similar trend to the Seebeck coefficient, especially for the P-type layer. The zT value change is generally higher than an 84 nm $Bi_{87}Sb_{13}$ thin film in Linseis's work [277]. However, sample N4 performed best at higher temperatures (>140°C).

### *7.4.3 Output test of the thin film*

To assess the capability of the thin film in generating power, a thin film of the active layer was deposited on a glass slide of 26 mm x 76mm, and the end of two sides was wrapped with copper tape to extract the energy. Part of the glass slide was put on a heating pan as a hot part, and the other side left outside the pan is cooled by air act as the cool side. When the heater was turned on, the temperature difference between the hot side and cold side produced a voltage and current which was recorded by a multi-meter as detailed in Figure 7.8a. The voltage increased with the growing temperature difference (Figure 7.8b), so as to the electric current (Figure 7.8a). This is in agreement with Francioso's finding on RF magnetron sputtered $Sb_2Te_3$ and $Bi_2Te_3$ thin film: the open circuit voltage and electrical power increase with increasing $\Delta T$ [278]. However, they reported a maximum output at $\Delta T$=40°C, and we found the open circuit voltage increased further with the difference of temperature up to 80°C. The resistance of the thin N-type film increased slightly with the increment in temperature. A similar change was observed on the P-type thin film on glass, and the open circuit voltage and current are higher for the P-type layer than those of the N-type layer. A follow-on test of thin film on the Kapton substrate shows a

similar result that the P-type layer has a high open circuit voltage and current than the N-type layer.

| Hot side (°C) | Cold side (°C) | Temperature difference (°C) | Current (μA) | Resistance (Ω) | voltage (mV) |
|---|---|---|---|---|---|
| 25 | 20 | 5 | 0.03 | | 0.2 |
| 30 | 20 | 10 | 0.04 | 57.6 | 0.4 |
| 35 | 20.15 | 14.85 | 0.06 | 54.6 | 0.6 |
| 40 | 20.77 | 19.23 | 0.07 | 53 | 0.7 |
| 45 | 21.96 | 23.04 | 0.08 | 57 | 0.9 |
| 48 | 20.76 | 27.24 | 0.11 | 67 | 1 |
| 52 | 20.38 | 31.62 | 0.14 | 67 | 1.1 |
| 57 | 20.22 | 36.78 | 0.15 | 68 | 1.2 |
| 60 | 20.28 | 39.72 | 0.16 | 70 | 1.3 |
| 63 | 20.26 | 42.74 | 0.18 | 74 | 1.4 |
| 70 | 20.43 | 49.57 | 0.2 | 78 | 1.6 |
| 72 | 20.47 | 51.53 | 0.22 | 69 | 2 |
| 86 | 20.65 | 65.35 | 0.24 | 68.1 | |
| 90 | 20.75 | 69.25 | 0.25 | 68 | |
| 93 | 20.78 | 72.22 | 0.25 | | 2.3 |
| 101 | 20.82 | 80.18 | 0.32 | 90 | 2.4 |

**a**

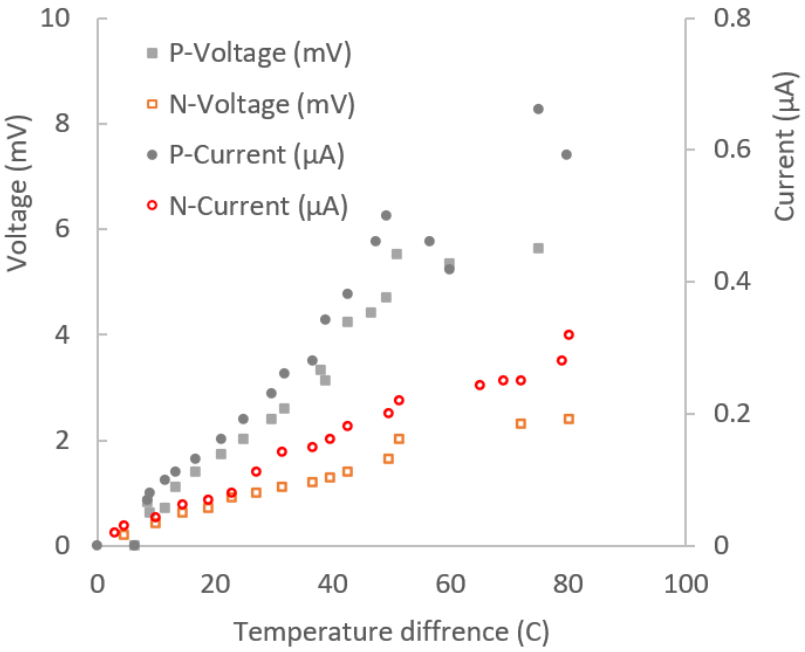


**b**

Figure 7.8. The output of thin film for both P-type (P4-G) and N-type (N4-G) layer on glass slide: (a) detail of the temperature change and related power output and resistance change; (b) the change of open circuit voltage and current against temperature difference.

Different combination of the P-type and N-type layer (12mm x 40 mm) on separated Kapton substrates was tested to investigate the effect of the power generation in different configurations such as P-N, P-P, N-N, PNP, PPN etc. (Figure 7.9a). It was found that the hot-cold-hot-cold…series link generates most of the power, however, links like Hot side (N strip)-cold side (N strip)-Cold side (P strip)-Hot side (P strip) generate less power even less than one single P or N strip as evidenced in Figure 7.9b.

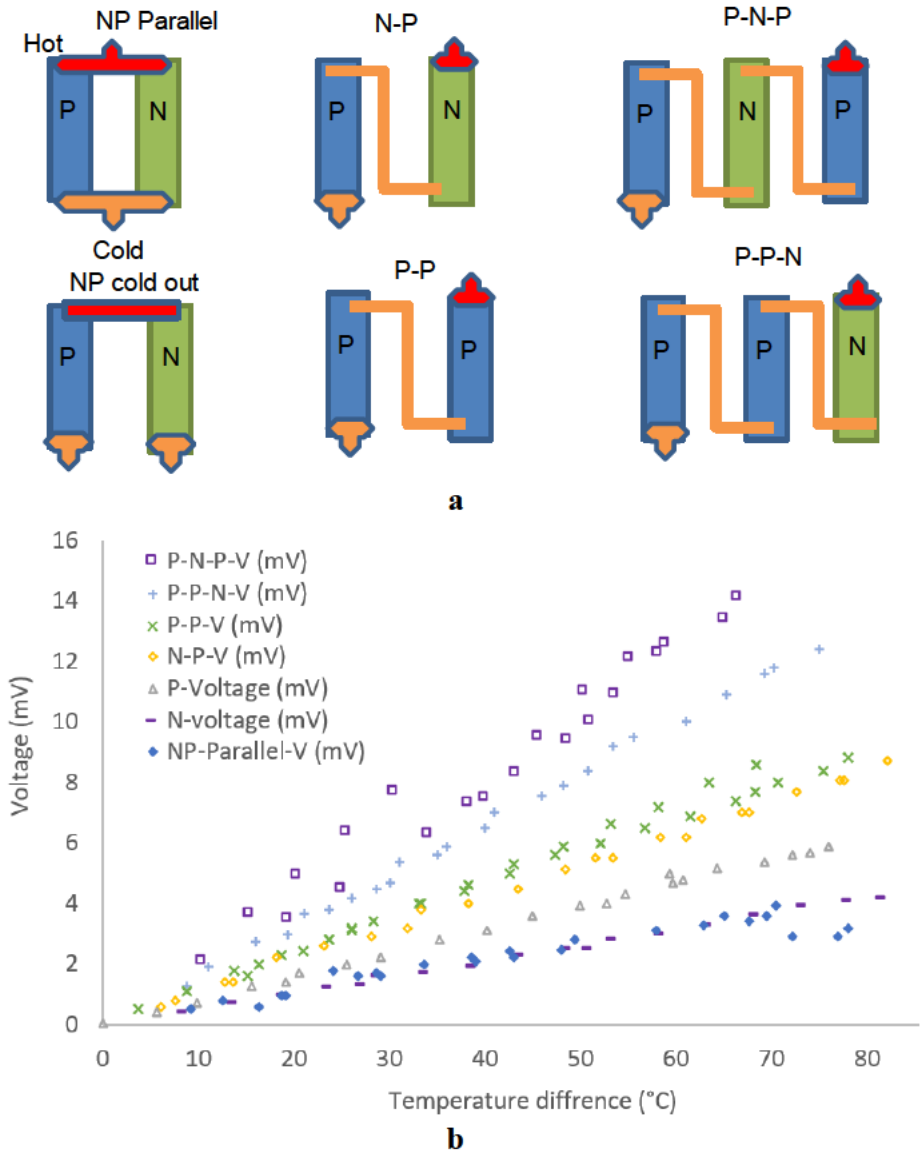


Figure 7.9. (a) Configuration of P-type and N-type layer (12mm x 30mm) on Kapton substrate; (b) open circuit voltage output comparison.

After test different configurations of P-type and/or N-type layers, a series link of 4 P-type layers with different thickness and width were used to assess the impact of thickness and width layer on the output of the power if the active layer (Figure 7.2a). Generally, increase the amount of active layer from one strip to four strips, the open circuit voltage increased proportionally for all the active layers, and the same is for the electric current output. As reported by Kwon, increasing the pair of P-type $Bi_{0.4}Sb_{1.6}Te_3$ and N-type $Bi_2Te_3$ layer grown by metal organic vapor phase deposition can boost the output of power [279]. Interestingly, the 6 mm wide and 40 mm length P-type layer (P4K-6mm) outperform a thicker layer on Kapton for sample P45k-6mm and a wide layer of 12 mm for P4K-12mm in all the strips as shown in Figure 7.10. In the meantime, all the P-type layer has higher output of power than the N-type layer on Kapton substrate, i.e., N4k-6mm.

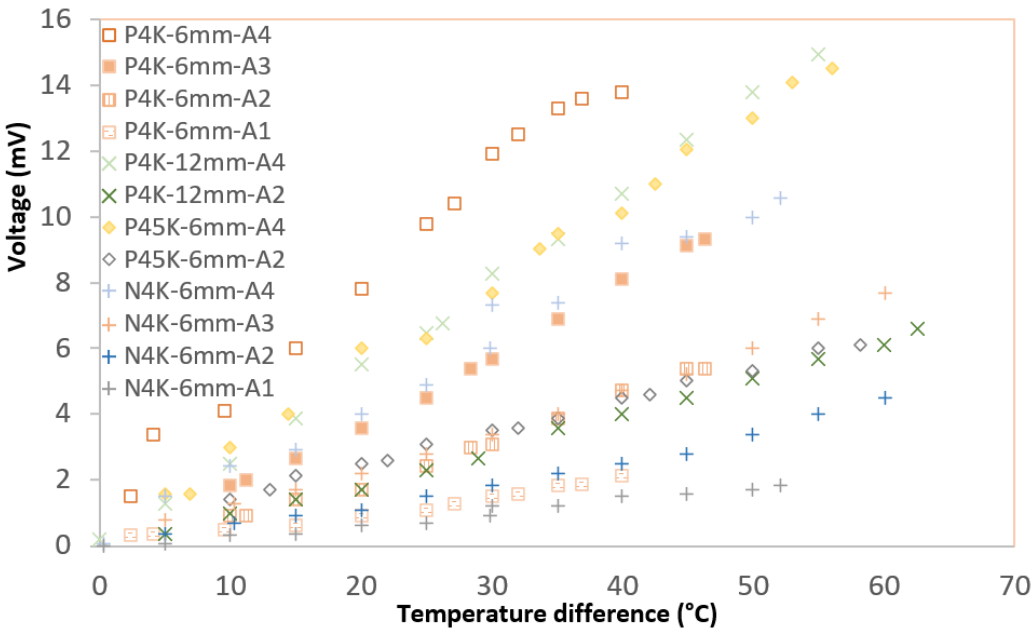


Figure 7.10. Open circuit voltage output of P-type layer with different widths (P4k-6mm and P4k-12mm) and thicknesses (P4k:2µm and P45k:3µm) on Kapton substrate.

## 7.5 Conclusions

The BiTe-based N-type and P-type thin films can be easily sputter deposited with a small target current on silicon, glass and Kapton HN polyimide foil substrate using DC magnetron sputtering mode. Fine columnar nano-sized grains were formed with a mixture phase of $Bi_2Te_3$ and $Bi_6Te_{7.2}Se_{1.8}$ in the N-type thin film and a mixture of BiTe and $Sb_2Te_3$ in the P-type layer.

For all the thin films, the thermal conductivity increased with the temperature. Generally, N-type layers have higher thermal conductivity and electrical conductivity in comparison with those P-type layers, and both of the conductivity values have a trend of increase with elevated temperature, especially at a temperature above 0°C. The Seebeck coefficient of P-type layers peaked at about 140°C and was superior to that of the N-type layer which grew steadily with temperature, while the N-type layer performed better at higher temperatures. The calculated zT value has a similar trend to the Seebeck coefficient.

Power output tests on the different combinations of active layers suggest a series of links of active layers can maximise the output power. A series of 4 active layers suggests that the P-type layer has a higher output of power than the N-type layer on the Kapton substrate and the longer the layer, the higher the output of current and the voltage. However, widening the strip or thickening the active layer didn't improve the output of power. Based on these findings, we will be able to design a device with optimized patterned thin-film strips on a flexible substrate to harvest the heat at lower temperature range such as the photovoltaic solar cell for increasing efficiency.

# Chapter 8 General discussion, key conclusions and future work

## 8.1 General discussion

Notwithstanding the fact that the outcomes from this research project have been reported in detail according to the theme in Chapters 4, 5, 6 and 7 and the results have also been discussed separated in these chapters, it is difficult to interconnect and synergies the outcomes given the nature of the paper-based thesis. Hence, this section is dedicated to synthesising these four themes (four papers) to provide a whole picture of this research work for a full understanding of the thesis.

As has been clearly demonstrated in this PhD project, it is necessary to optimise many materials-related factors, ranging from material design, through interfacial layers and surface coating to module design, to increase the efficiency and lifespan of thermoelectric modules. Specifically, it is essential to improve the oxidation resistance and thermal stability of TE materials at high temperatures. As reported in Chapter 4, when the N-type (Zr,Ti)Ni(Sn,Sb) and P-type (Zr,Ti)Co(Sn,Sb) half-Heusler TE materials are exposed to cyclic oxidation between room temperature and 500℃, a serious of changes occurred in the surface morphology (see Figure 4.4b&c). For both TE materials, a multilayered structure has formed on the surface after oxidation, which has completely different microstructure and chemical composition as compared with that for the original materials produced (see Figure 4.5a&b). The same multilayered structures were observed on the repeatedly tested separate N-type and P-type materials at the same experimental conditions. As seen in the mass gain result (Figure 4.2), the oxidation severity is quite high for both N-type and P-type TE materials during the first ten cycles. forming the oxide products rapidly on the surface, which was confirmed by XRD in Figure 4.3. After 10 cycles, the oxidation severity partially decreased due to the oxides ($SnO_2$, $(Zr,Ti)O_2$ and $Sb_2O_4$) and oxidation products ($Ni_3Sn_4$ for N-type and CoSb for P-type materials) formed on the surface making aggressive oxygen diffusion difficult. However, the oxidation of

materials continued. Such changes in microstructure and composition on the TE material surface would deteriorate its TE performance and power output of thermoelectric generators as reported by Kang and co-researchers [193]. These severe surface oxidation in conjunction with the thermal stress induced by the cyclic heating and cooling led to the formation of cracking and spallation (Figure 4.4) which will cause mechanical degradation when the number of cycles increases and hence significantly reduce the service life of the TE devices in practical applications (Figure 4.5c&d). It should be noted that the samples were carefully prepared without causing mechanical degradation. To avoid that, the samples were first mounted in a conductive bakelite, cut for the cross-sectional SEM/EDX investigation, and gently ground and polished. The same procedure was also followed when preparing the CrSi-coated samples.

It is crucial to accurately investigate the TE material's oxidation behaviour at different temperatures (500℃-600℃), durations (10h-50h) and methods (static-cyclic). To this end, the oxidation tests were repeated at least two times on the separate samples at the same experimental conditions, and the general findings were presented in this study. As shown in Chapter 5, a similar multilayered microstructure was also observed on the cross-sections of N-type and P-type materials after static oxidation at 500℃ for 10 hours (Figure *5.3*a and Figure *5.6*a). The multilayer formed on the N-type and P-type materials were thickened with the same mechanism as described in Figure 4.7 in Chapter 4. Considering that the TE materials should deal with the extreme conditions for converting waste heat released from the automobile exhaust (more than 550℃), the oxidation temperature and duration were increased to 600℃ and 50h, respectively. As can be seen in Figure 5.3d and Figure 5.6d, the surface morphology changed to thick double layers for both P-type and N-type TE materials. As demonstrated in Table *5.3*, the mass gain for both N-type and T-type materials is more from cyclic oxidation than from static oxidation. This is because due to the thermal shock effect, the residual stress intensity at the multilayer structure would reach the critical value over time, leading to

micro/nano cracks formation. Therefore, cyclic oxidation is more severe than static oxidation, as confirmed by the repeated oxidation tests at the same conditions, and the evaluation of oxidation protection coating should be tested under cyclic oxidation conditions, if possible, which are more relevant to the real application environment for most TE devices.

In addition to oxidation, another issue encountered at high temperatures, especially in complex structured and multi-component TE materials, is the sublimation of elements with low melting points, which will deteriorate the performance of TE materials and devices. As reported in Chapters 4 and 5, the N-type and P-type materials used in this study contain such sublimable elements as Sn and Sb (see Table 4.1). Specifically, the formation of a double-layered oxide case on the oxidised N-type and P-type materials at 600℃ was facilitated by the sublimation in addition to oxidation (see Figure *5.3*d and Figure *5.6*d). For instance, the significant changes in surface morphology resulting from static and cyclic oxidation of the N-type material can be associated with the high Sn content. A similar observation of sublimation of Sb was observed in the oxidised P-type material. On the other hand, oxidation-induced cracks and local spallation could also facilitate the sublimation by providing the passes for sublimated gases to escape.

As evidenced in Chapter 5, the advanced CrSi coatings developed from this research can significantly reduce the oxidation kinetics and mass gain (see Figure *5.8*) of the TE materials investigated, implying that the oxidation resistance and thermal stability of the TE materials have been effectively improved. SEM and EDX analyses revealed that no microstructural changes were observed in the CrSi-coated TE material (see Figure *5.3*, Figure *5.4*, Figure *5.6* and Figure *5.7*), neither layered structures nor thick double layers were formed, thus providing effective protection of the TE materials from oxidation. Although it was found by O mapping (Figure *5.4*) that oxygen penetrated into the CrSi coating during the oxidation tests, it is interesting to note that O did not penetrate throughout the whole coating layer and that Si co-existed with O and Cr within the coating layer. It is thus envisaged that the aggressive oxygen

atoms were trapped within the coating due to the strong affinity of O with Cr and Si and thus further diffusion to the TE materials substrate was retarded or even prevented.

Although outward diffusion of Sn in the substrate TE material was identified by Sn mapping, it was fully stopped by the CrSi coating (Figure *5.7*) thus preventing further sublimation of Sn from the substrate. These findings indicate that the CrSi coatings developed not only provide effective protection against oxidation, but also significantly prevent/reduce the sublimation at high temperatures. However, it is noteworthy that different surface morphologies or interface properties observed (see Figure *5.3*e&g and Figure *5.10*e&g) after the oxidation of CrSi-coated TE materials deposited under the same parameters indicate that although CrSi coatings effectively protect N-type and P-type materials against oxidation and sublimation, their responses are also oxidation testing condition dependent. As abovementioned, cyclic oxidation is more severe than static oxidation, leading to the formation of micro/nano-cracks, which are the pathways for further diffusion of oxygen into the material, triggering the sublimation of Sn towards the surface. This is the main reason for accumulating Sn at the interface of the cyclically oxidised PCO5-50 sample, as shown in Figure 5.11 On the other hand, it was observed that the produced CrSi coatings show a slight difference after oxidation, as seen in Figure 5.10e&g, meaning that they have not the same quality, possibly because of where the samples were put on the sample holder in the PVD equipment as the deposition rate at the bottom of the sample holder was a bit better than the upper. Even though the developed CrSi coatings protected the TE substrates quite effectively, the quality of the coatings was not perfectly similar to each other possibly because of the abovementioned dissimilar deposition rate issue in the equipment.

It is believed that the CrSi coatings can protect the HH TE materials studied for more cycles (maybe more than a thousand) at 500°C and 600°C as the operation temperatures are reasonably low. However, it can be said that a further increase in the oxidation temperature would

significantly reduce the coating's protectability against oxidation, as illustrated in our previous study [169].

As discussed in Chapter 2, the performance and service life of TE devices depends not only on the TE materials and components but also on the interfacial contact properties between the TE components/elements and the electrodes. Therefore, one of the themes of the PhD study was focused on improving the interfacial contact properties by coating TE materials with metallising layers with high electrical conductivity and low contact resistance. For this purpose, Ni & NiGO coatings have been developed and deposited on the TE materials. The detailed characterisation of these coatings on stainless steel substrate in the early stage showed that the addition of GO had no noticeable effect on the interfacial contact and sheet resistances (see Figure *6.10* and Figure 6.11). Two possible hypotheses can be proposed as the main reasons for this: the first is the activation of GO particles was not successful, and the second is the incorporated GO addition was not sufficient to change the electrical properties. Further systematic work optimised the electro-brush coating technique, and Ni/GO coatings with low interfacial contact and sheet resistance have been successfully deposited on P-type (Zr,Ti)Co(Sn,Sb) TE material as intended. It is believed that the produced Ni coating with low contact resistance would enhance the TE performance of the recently used TE power generators and modules. It was also crucial to achieve microstructural stability at the contact surfaces at high temperatures, in addition to optimised contact properties. In addition, the results of thermal tests showed that the developed Ni/GO coatings not only improved the connection properties of the material but also significantly protected the material against oxidation (see Figure *6.14*) mainly due to the high oxidation and thermal stability of Ni.

Whilst the PhD research is mainly focused on half-Heusler TE materials for medium temperature applications, the last theme of the PhD research is dealing with improving TE performance of BiTe-based TE materials for harvesting waste heat at low temperatures.

However, as it is known, the temperature difference is quite low for low temperature waste heat so that the electrical potential collected from the TE module is very low because the zT values of bulk TE materials are very small at low temperature. To address this issue, the nanostructured BiTe-based thin films were developed as an alternative to bulk materials. It was observed that the power output of thin films deposited on different substrates (glass, Kapton and silicon) is closely related to how the active layers are connected. Although the proportional increase in thermal conductivity as well as electrical conductivity with increasing temperature limited the further improvement of the zT value, the research has provided some valuable information for the design of a device with optimised patterned thin-film strip on a flexible substrate to harvest the heat at a low temperature.

## 8.2 Key conclusions

Comprehensive conclusions have been presented in Chapters 4-7 and this section summarises the key conclusions for the ease of grasping the major outcomes from the PhD research.

### *8.2.1 Cyclic oxidation behaviour of N-type (Zr,Ti)Ni(Sn,Sb) and P-type (Zr,Ti)Co(Sn,Sb) TE materials*

This study was focused on the investigation of the oxidation behaviour and mechanism of the N-type and P-type half-Heusler TE materials under thermal cycles between room temperature and 500°C to advance scientific understanding and provide essential information for the design of protection coatings. This study revealed that serve oxidation occurred to the surface of half-Heusler TE materials during cyclic oxidation between room and 500°C, resulting in significant damage to their surfaces and possible reduction of serve life. The oxidation of N-type material experienced a considerably faster mass gain compared to the P-type material. Alternated multilayers of $Ni_3Sn_4$+$SnO_2$+$(Zr,Ti)O_2$ and CoSb+$SnO_2$+$Sb_2O_4$+$(Zr,Ti)O_2$ were identified on the cross-sections of the N-type and P-type materials, respectively, after the cyclic testing, which would deteriorate the thermoelectric performance of the materials.

### *8.2.2 Developing advanced CrSi coatings for combatting surface degradation of n-type (Zr,Ti)Ni(Sn,Sb) and p-type (Zr,Ti)Co(Sn,Sb) half-Heusler thermoelectric materials*

In this study, advanced CrSi coatings were developed and deposited on N-type (Zr,Ti)Ni(Sn,Sb) and P-type (Zr,Ti)Co(Sn,Sb) thermoelectric (TE) materials for protection against high-temperature static and cyclic oxidation. The developed CrSi coatings on the N-type and P-type TE materials provided very high thermal stability and oxidation resistance and protected the TE materials against oxidation and sublimation during both static and cyclic oxidation.

### *8.2.3 Development of Ni/NiGO contact layers for p-type (Zr,Ti)Co(Sn,Sb) thermoelectric material by low-cost electro-brush plating technique*

This study investigated the production of highly electrically conductive Ni&NiGO layers to reduce the interfacial contact resistance of TE materials. The development of the coatings was carried out on the stainless steel substrate, and the optimal Ni coatings were deposited on the P-type (Zr,Ti)Co(Sn,Sb) TE material using a low-cost electro-brush plating technique. The experimental findings revealed that the Ni&NiGO coatings with a layer-by-layer structure can easily deposited on TE materials with no pore or spallation. Even though the GO is well incorporated into the Ni coating, there were only marginal differences between the interfacial and sheet resistance, crucial properties of a contact layer, of Ni and NiGO coatings. In addition, the microstructure stability of the P-type material at high temperatures was achieved by the Ni coating by preventing oxidation and sublimation.

### *8.2.4 Characterisation of magnetron sputtered BiTe based thermoelectric thin films*

In this study, N-type and P-type BiTe-based thin films with nano-sized grains were deposited on silicon, glass and Kapton HN polyimide foil substrates using a DC magnetron sputtering system. The general outcome of the study showed that the thermal conductivity of all thin films increased with increasing temperature. The Seebeck coefficient of P-type layers peaked at about 140°C and was superior to that of the N-type layer which grew steadily with temperature, while

the N-type layer performed better at higher temperatures. The calculated zT value has a similar trend to the Seebeck coefficient. The output power can be enhanced by a series of links of active layers. However, widening the strip or thickening the active layer didn't improve the output of power.

## 8.3 Future work

Although all the objectives of this PhD research have been in terms of advancing scientific understanding of the oxidation behaviour and mechanisms of the N-type (Zr,Ti)Ni(Sn,Sb) and P-type (Zr,Ti)Co(Sn,Sb) TE materials (Chapter 4), development of advanced CrSi coatings (Chapter 5) to protect the TE materials from oxidation and sublimation, and design of Ni and NiGO interfacial layers (Chapter 6) and nanostructured thin films (Chapter 7) aiming at improving the performance of TE devices, further investigation and research are recommended as follows:

1- Investigating the effect of oxidation on the TE performance of TE materials used in this PhD project by measuring their thermal conductivity, Seebeck coefficient, module efficiency and figure of merit before and after oxidation testing.
2- Investigating the oxidation behaviour of CrSi coatings at 550℃ (this is based on the maximum temperature of an automobile exhaust heated because of the hot gases) for 250, 500 and 1000, aiming to observe the protection ability of the coatings under the extreme experimental temperature and cycle conditions.
3- Measuring the interfacial contact resistance of Ni coating on TE materials.
4- Designing a TE module with optimised patterned thin-film strips on a flexible substrate to harvest heat at lower temperature ranges, such as those encountered in photovoltaic solar cells, to increase their efficiency.

# REFERENCES


1. Demirbas, A., A. Sahin-Demirbas, and A. Hilal Demirbas, *Global energy sources, energy usage, and future developments.* Energy Sources, 2004. **26**(3): p. 191-204.

2. Kartal, M.T., *The role of consumption of energy, fossil sources, nuclear energy, and renewable energy on environmental degradation in top-five carbon producing countries.* Renewable Energy, 2022. **184**: p. 871-880.

3. Ebhota, W.S. and T.-C. Jen, *Fossil fuels environmental challenges and the role of solar photovoltaic technology advances in fast tracking hybrid renewable energy system.* International Journal of Precision Engineering and Manufacturing-Green Technology, 2020. **7**: p. 97-117.

4. Husin, H. and M. Zaki, *A critical review of the integration of renewable energy sources with various technologies.* Protection and control of modern power systems, 2021. **6**(1): p. 1-18.

5. Ang, T.-Z., et al., *A comprehensive study of renewable energy sources: Classifications, challenges and suggestions.* Energy Strategy Reviews, 2022. **43**: p. 100939.

6. Jurasz, J., et al., *A review on the complementarity of renewable energy sources: Concept, metrics, application and future research directions.* Solar Energy, 2020. **195**: p. 703-724.

7. Mamur, H., et al., *Thermoelectric generators act as renewable energy sources.* Cleaner Materials, 2021. **2**: p. 100030.

8. Zhang, Y., Y. Han, and Q. Meng, *The performance of Mg2Si-based thermoelectric materials prepared from MgH2.* Materials Research Innovations, 2015. **19**(sup1): p. S1-264-S1-268.

9. Zhang, F., et al., *Preparation of Mg2Si based thermoelectric nanomaterials by low-temperature reaction.* Procedia Engineering, 2012. **27**: p. 200-205.

10. Su, C.-H., *Design, growth and characterization of PbTe-based thermoelectric materials.* Progress in Crystal Growth and Characterization of Materials, 2019. **65**(2): p. 47-94.

11. Hao, X., et al., *Performance optimization for PbTe-based thermoelectric materials.* Frontiers in Energy Research, 2021. **9**: p. 754532.

12. Zhu, H., J.-Y. Zhao, and C. Xiao, *Improved thermoelectric performance in n-type BiTe facilitated by defect engineering.* Rare Metals, 2021. **40**(10): p. 2829-2837.

13. Ng, I., et al., *Bismuth telluride based nanowires for thermoelectric power generation.* Materials Today: Proceedings, 2016. **3**(2): p. 533-537.

14. Xia, K., et al., *Half-Heusler thermoelectric materials.* Applied Physics Letters, 2021. **118**(14).

15. Zhu, T., et al., *High efficiency half-Heusler thermoelectric materials for energy harvesting.* Advanced Energy Materials, 2015. **5**(19): p. 1500588.

16. Rogl, G. and P. Rogl, *Skutterudites, a most promising group of thermoelectric materials.* Current opinion in green and sustainable chemistry, 2017. **4**: p. 50-57.

17. Rull-Bravo, M., et al., *Skutterudites as thermoelectric materials: revisited.* Rsc Advances, 2015. **5**(52): p. 41653-41667.

18. Agote, I., et al. *Thermoelectric materials for automotive and marine applications*. in *Euro PM 2014 International Conference and Exhibition*. 2014. European Powder Metallurgy Association (EPMA).

19. Bakhtiaryfard, L. and Y.S. Chen, *Design and analysis of a thermoelectric module to improve the operational life.* Advances in Mechanical Engineering, 2015. **7**(1): p. 152419.

20. Brostow, W., et al., *Bismuth telluride-based thermoelectric materials: Coatings as protection against thermal cycling effects.* Journal of Materials Research, 2012. **27**(22): p. 2930-2936.

21. Park, Y.-S., et al., *Protective enamel coating for n-and p-type skutterudite thermoelectric materials.* Journal of Materials Science, 2015. **50**: p. 1500-1512.

22. Nieroda, P., et al., *New high temperature amorphous protective coatings for Mg2Si thermoelectric material.* Ceramics International, 2019. **45**(8): p. 10230-10235.

23. He, R., G. Schierning, and K. Nielsch, *Thermoelectric devices: a review of devices, architectures, and contact optimization.* Advanced Materials Technologies, 2018. **3**(4): p. 1700256.

24. Zhu, Q., et al., *Bottom-up engineering strategies for high-performance thermoelectric materials.* Nano-Micro Letters, 2021. **13**(1): p. 119.

25. Yang, L., et al., *High performance thermoelectric materials: progress and their applications.* Advanced Energy Materials, 2018. **8**(6): p. 1701797.

26. Data, W.E. *World Fossil Fuel Production & Primary Energy*. 2024 [cited 2024 04.04.2024]; Available from: https://www.worldenergydata.org/world-fossil-fuel-production-and-primary-energy/.

27. Behnia, K., *Fundamentals of thermoelectricity*. 2015: OUP Oxford.

28. Rodriguez, R., et al., *Review and trends of thermoelectric generator heat recovery in automotive applications.* IEEE Transactions on Vehicular Technology, 2019. **68**(6): p. 5366-5378.

29. Yang, J. and T. Caillat, *Thermoelectric materials for space and automotive power generation.* MRS bulletin, 2006. **31**(3): p. 224-229.

30. Srivastava, R.S., et al., *Solar assisted thermoelectric cooling/heating system for vehicle cabin during parking: A numerical study.* Renewable Energy, 2022. **181**: p. 384-403.

31. Silva, M., et al., *Thin films for thermoelectric applications.* Scanning Probe Microscopy in Nanoscience and Nanotechnology 3, 2012: p. 485-528.

32. Leonov, V. and R.J. Vullers, *Wearable electronics self-powered by using human body heat: The state of the art and the perspective.* Journal of Renewable and Sustainable Energy, 2009. **1**(6).

33. Bonin, R., et al., *Design and characterization of small thermoelectric generators for environmental monitoring devices.* Energy Conversion and Management, 2013. **73**: p. 340-349.

34. Zoui, M.A., S. Bentouba, and M. Bourouis, *The Potential of Solar Thermoelectric Generator STEG for Implantation in the Adrar Region.* Alger. J. Renew. Energy Sustain. Dev, 2020. **2**: p. 17-27.

35. Zou, S., et al., *Modeling assisted evaluation of direct electricity generation from waste heat of wastewater via a thermoelectric generator.* Science of The Total Environment, 2018. **635**: p. 1215-1224.

36. Kramer, D.P., et al. *Recent joint studies related to the development of space radioisotope power systems*. in *E3S Web of Conferences*. 2017. EDP Sciences.

37. Chen, G., et al., *Recent developments in thermoelectric materials.* International materials reviews, 2003. **48**(1): p. 45-66.

38. Nielsen, P. and P. Taylor, *Theory of thermoelectric effects in metals and alloys.* Physical Review B, 1974. **10**(10): p. 4061.

39. Chaturvedi, K.M., *Synthesis and investigation of thermo-electric properties of Skutterudites CoSb3/Graphene particles nanocomposite.* Nat. Phys. Lab. New Delhi, 2014.

40. Drebushchak, V., *The peltier effect.* Journal of Thermal Analysis and Calorimetry, 2008. **91**: p. 311-315.

41. Qin, B., et al., *Ultrahigh average ZT realized in p-type SnSe crystalline thermoelectrics through producing extrinsic vacancies.* Journal of the American Chemical Society, 2020. **142**(12): p. 5901-5909.

42. Zhang, M., et al., *Achieving High Carrier Mobility And Thermal Stability in Plainified Rhombohedral GeTe Thermoelectric Materials with zT> 2.* Advanced Functional Materials, 2023: p. 2307864.

43. Wu, G., et al., *High-Efficiency Thermoelectric Module Based on High-Performance Bi0. 42Sb1. 58Te3 Materials.* Advanced Functional Materials, 2023. **33**(47): p. 2305686.

44. Wang, Y., J. Feng, and Z.-H. Ge, *Enhancing power factor and ZT in non-toxic Bi2S3 bulk materials via band engineering and electronic structure modulation.* Ceramics International, 2023. **49**(14): p. 23680-23688.

45. Hu, Z., et al., *Inducing High Power Factor in Cu2GeSe3-Based Bulk Materials via (Bi, Zn)-Co-doping.* ACS Applied Energy Materials, 2023. **6**(5): p. 2962-2972.

46. Luo, P., et al., *TaFeSb-Based Half-Heusler Thermoelectrics with High zT> 1 through the Alloying Effect.* ACS Applied Energy Materials, 2023. **6**(19): p. 10070-10077.

47. Pang, X., et al., *Ultrahigh thermoelectric power factor achieved in Yb filled CoSb3 skutterudites through additional Al doping.* Chemical Engineering Journal, 2024. **481**: p. 148457.

48. Wang, B., et al., *Enhanced thermoelectric performance of Sb-doped Mg2Si0. 4Sn0. 6 via doping, alloying and nanoprecipitation.* Journal of Materiomics, 2023.

49. Ning, X., et al., *Record High Power Factor and Low Thermal Conductivity in Amorphous/PbTe/Amorphous Multiple Quantum Wells.* Advanced Functional Materials, 2023: p. 2303981.

50. Xiao, Y., et al., *Advanced Average Power Factor and ZT Value in PbSe Thermoelectric with Dual Interstitials Doping.* Energy & Environmental Science, 2024.

51. Oh, J., H.S. Lee, and S. Yi, *Enhanced thermoelectric performance of NbCoSb half-Heusler alloys by using an amorphous precursor.* Journal of Non-Crystalline Solids, 2024. **624**: p. 122729.

52. Su, B., et al., *Re-Doped p-Type Thermoelectric SnSe Polycrystals with Enhanced Power Factor and High ZT> 2.* Advanced Functional Materials, 2023: p. 2301971.

53. Kumar, A., et al., *A review on fundamentals, design and optimization to high ZT of thermoelectric materials for application to thermoelectric technology.* Journal of Electronic Materials, 2021. **50**: p. 6037-6059.

54. Jaldurgam, F.F., Z. Ahmad, and F. Touati, *Synthesis and performance of large-scale cost-effective environment-friendly nanostructured thermoelectric materials.* Nanomaterials, 2021. **11**(5): p. 1091.

55. Al-Fartoos, M.M.R., et al., *Advancing Thermoelectric Materials: A Comprehensive Review Exploring the Significance of One-Dimensional Nano Structuring.* Nanomaterials, 2023. **13**(13): p. 2011.

56. Liu, H.-T., et al., *High-performance in n-type PbTe-based thermoelectric materials achieved by synergistically dynamic doping and energy filtering.* Nano Energy, 2022. **91**: p. 106706.

57. Tsubota, T., et al., *Thermoelectric properties of Al-doped ZnO as a promising oxide material for high-temperature thermoelectric conversion.* Journal of Materials Chemistry, 1997. **7**(1): p. 85-90.

58. Pei, Y., H. Wang, and G.J. Snyder, *Band engineering of thermoelectric materials.* Advanced materials, 2012. **24**(46): p. 6125-6135.

59. Fu, C., et al., *Band engineering of high performance p-type FeNbSb based half-Heusler thermoelectric materials for figure of merit zT> 1.* Energy & Environmental Science, 2015. **8**(1): p. 216-220.

60. Saparamadu, U., et al., *Achieving high-performance p-type SmMg 2 Bi 2 thermoelectric materials through band engineering and alloying effects.* Journal of Materials Chemistry A, 2020. **8**(31): p. 15760-15766.

61. Kihoi, S.K., et al., *Optimized Mn and Bi co-doping in SnTe based thermoelectric material: A case of band engineering and density of states tuning.* Journal of Materials Science & Technology, 2021. **85**: p. 76-86.

62. Witting, I.T., et al., *The thermoelectric properties of bismuth telluride.* Advanced Electronic Materials, 2019. **5**(6): p. 1800904.

63. Yeo, Y. and T. Oh, *Thermoelectric properties of p-type (Bi, Sb) 2Te3 nanocomposites dispersed with multiwall carbon nanotubes.* Materials Research Bulletin, 2014. **58**: p. 54-58.

64. Wang, Y., et al., *High porosity in nanostructured n-type Bi2Te3 obtaining ultralow lattice thermal conductivity.* ACS applied materials & interfaces, 2019. **11**(34): p. 31237-31244.

65. Pei, J., et al., *Bi2Te3-based applied thermoelectric materials: research advances and new challenges.* National science review, 2020. **7**(12): p. 1856-1858.

66. Fang, T., X. Zhao, and T. Zhu, *Band structures and transport properties of high-performance half-Heusler thermoelectric materials by first principles.* Materials, 2018. **11**(5): p. 847.

67. Liu, Z., et al., *Design of high-performance disordered half-Heusler thermoelectric materials using 18-electron rule.* Advanced Functional Materials, 2019. **29**(44): p. 1905044.

68. Appel, O., et al., *The initial stage in oxidation of ZrNiSn (half Heusler) alloy by oxygen.* Materials, 2019. **12**(9): p. 1509.

69. Gu, J., et al., *High-temperature oxidation mechanism of ZrCoSb-based half-Heusler thermoelectric compounds.* Journal of Materials Science & Technology, 2023. **148**: p. 242-249.

70. Chauhan, N.S., et al., *Compositional tailoring for realizing high thermoelectric performance in hafnium-free n-type ZrNiSn half-Heusler alloys.* ACS applied materials & interfaces, 2019. **11**(51): p. 47830-47836.

71. Chauhan, N.S., et al., *Vanadium-doping-induced resonant energy levels for the enhancement of thermoelectric performance in Hf-free ZrNiSn half-Heusler alloys.* ACS Applied Energy Materials, 2018. **1**(2): p. 757-764.

72. Rogl, G. and P.F. Rogl, *Development of thermoelectric half-Heusler alloys over the past 25 years.* Crystals, 2023. **13**(7): p. 1152.

73. Kjekshus, A., et al., *Compounds with the skutterudite type crystal structure. III. structural data for arsenides and antimonides.* Acta Chem. Scand. A, 1974. **28**: p. 99-103.

74. Cheng, X., N. Farahi, and H. Kleinke, *Mg 2 Si-based materials for the thermoelectric energy conversion.* Jom, 2016. **68**: p. 2680-2687.

75. Santos, R., S.A. Yamini, and S.X. Dou, *Recent progress in magnesium-based thermoelectric materials.* Journal of Materials Chemistry A, 2018. **6**(8): p. 3328-3341.

76. Vining, C.B., *An inconvenient truth about thermoelectrics.* Nature materials, 2009. **8**(2): p. 83-85.

77. Han, C., Z. Li, and S. Dou, *Recent progress in thermoelectric materials.* Chinese science bulletin, 2014. **59**: p. 2073-2091.

78. Elsheikh, M.H., et al., *A review on thermoelectric renewable energy: Principle parameters that affect their performance.* Renewable and sustainable energy reviews, 2014. **30**: p. 337-355.

79. Ma, Z., et al., *Review of experimental approaches for improving zT of thermoelectric materials.* Materials Science in Semiconductor Processing, 2021. **121**: p. 105303.

80. Jia, N., et al., *Achieving enhanced thermoelectric performance in multiphase materials.* Accounts of Materials Research, 2022. **3**(2): p. 237-246.

81. Wu, T., et al., *Comprehensive review on thermoelectric electrodeposits: Enhancing thermoelectric performance through nanoengineering.* Frontiers in Chemistry, 2021. **9**: p. 762896.

82. Shi, X., L. Chen, and C. Uher, *Recent advances in high-performance bulk thermoelectric materials.* International Materials Reviews, 2016. **61**(6): p. 379-415.

83. Chiu, W.-T., C.-L. Chen, and Y.-Y. Chen, *A strategy to optimize the thermoelectric performance in a spark plasma sintering process.* Scientific reports, 2016. **6**(1): p. 23143.

84. Siebert, J.P., C.M. Hamm, and C.S. Birkel, *Microwave heating and spark plasma sintering as non-conventional synthesis methods to access thermoelectric and magnetic materials.* Applied Physics Reviews, 2019. **6**(4).

85. Mitra, S. and T. Maiti, *Thermoelectric Materials Synthesized by Spark Plasma Sintering (SPS) for Clean Energy Generation.* Spark Plasma Sintering of Materials: Advances in Processing and Applications, 2019: p. 493-514.

86. Shi, X.-L., J. Zou, and Z.-G. Chen, *Advanced thermoelectric design: from materials and structures to devices.* Chemical reviews, 2020. **120**(15): p. 7399-7515.

87. Gorskyi, P., *Typical mechanisms of degradation of thermoelectric materials and ways to reduce their impact on the reliability of thermoelectric modules.* Physics and Chemistry of Solid State, 2022. **23**(3): p. 505-516.

88. Zhao, D., et al., *High temperature oxidation behavior of cobalt triantimonide thermoelectric material.* Journal of alloys and compounds, 2010. **504**(2): p. 552-558.

89. Wang, L., et al., *High temperature oxidation behavior of ZrNiSn-based half-Heusler thermoelectric material.* Corrosion Science, 2023. **225**: p. 111606.

90. Li, Y., et al., *High-temperature oxidation behavior of thermoelectric SnSe.* Journal of Alloys and Compounds, 2016. **669**: p. 224-231.

91. Inoue, H., et al., *Examination of oxidation resistance of Mg2Si thermoelectric modules at practical operating temperature.* Journal of Alloys and Compounds, 2018. **735**: p. 828-832.

92. Shtern, M., et al., *Mechanical properties and thermal stability of nanostructured thermoelectric materials on the basis of PbTe and GeTe.* Journal of Alloys and Compounds, 2023. **946**: p. 169364.

93. Buha, J., et al., *Thermal stability and anisotropic sublimation of two-dimensional colloidal Bi2Te3 and Bi2Se3 nanocrystals.* Nano letters, 2016. **16**(7): p. 4217-4223.

94. Zhao, D., et al., *High temperature sublimation behavior of antimony in CoSb3 thermoelectric material during thermal duration test.* Journal of Alloys and Compounds, 2011. **509**(6): p. 3166-3171.

95. Gelbstein, Y., et al., *Thermoelectric properties of spark plasma sintered composites based on TiNiSn half-Heusler alloys.* Journal of Materials Research, 2011. **26**(15): p. 1919-1924.

96. Gorskyi, P., *Sublimation of a volatile component as a possible mechanism for thermoelectric material degradation.* Physics and Chemistry of Solid State, 2022. **23**(2): p. 204-209.

97. Park, K.-H., et al., *Thermal stability of the thermoelectric skutterudite In 0.25 Co 3 MnSb 12.* Journal of the Korean Physical Society, 2014. **64**: p. 79-83.

98. Nesbitt, J.A., *Rate of sublimation of Yb 14 MnSb 11, a thermoelectric material for space power applications.* Journal of electronic materials, 2014. **43**: p. 3128-3137.

99. Ohsugi, I., et al., *Dissociation and sublimation of tellurium from the thermoelectric tellurides.* Materials Research Innovations, 2015. **19**(sup5): p. S5-301-S5-303.

100. Bao, X., et al., *Mechanical properties of thermoelectric generators.* Journal of Materials Science & Technology, 2023. **148**: p. 64-74.

101. Gahlawat, S., et al., *Mechanical Properties of Thermoelectric Materials*, in *Advanced Thermoelectrics*. 2017, CRC Press. p. 555-602.

102. Isotta, E., et al., *Elastic moduli: a tool for understanding chemical bonding and thermal transport in thermoelectric materials.* Angewandte Chemie, 2023. **135**(12): p. e202213649.

103. Guttmann, G.M. and Y. Gelbstein, *Mechanical properties of thermoelectric materials for practical applications.* Bringing thermoelectricity into reality, 2018: p. 63-80.

104. Li, G., et al., *Fracture toughness of thermoelectric materials.* Materials Science and Engineering: R: Reports, 2021. **144**: p. 100607.

105. Zhang, Y., et al., *Interfacial Crack Growth-Based Fatigue Lifetime Prediction of Thermoelectric Modules under Thermal Cycling.* ACS Applied Materials & Interfaces, 2023. **16**(1): p. 1137-1147.

106. Enescu, D. and E.O. Virjoghe, *A review on thermoelectric cooling parameters and performance.* Renewable and Sustainable Energy Reviews, 2014. **38**: p. 903-916.

107. Crane, N.B. and P. McKnight, *Impact of self-assembly process errors on thermoelectric performance.* Journal of Electronic Packaging, 2012. **134**(3): p. 031001.

108. Araiz, M., et al., *The importance of the assembly in thermoelectric generators.* Bringing Thermoelectricity into Reality, 2018. **7**.

109. Freer, R. and A.V. Powell, *Realising the potential of thermoelectric technology: A Roadmap.* Journal of Materials Chemistry C, 2020. **8**(2): p. 441-463.

110. Wu, W., et al., *Interfacial advances yielding high efficiencies for thermoelectric devices.* Journal of Materials Chemistry A, 2021. **9**(6): p. 3209-3230.

111. Liu, W. and S. Bai, *Thermoelectric interface materials: a perspective to the challenge of thermoelectric power generation module.* Journal of Materiomics, 2019. **5**(3): p. 321-336.

112. Xie, L., et al., *Screening strategy for developing thermoelectric interface materials.* Science, 2023. **382**(6673): p. 921-928.

113. Medlin, D. and G. Snyder, *Interfaces in bulk thermoelectric materials: a review for current opinion in colloid and interface science.* Current Opinion in Colloid & Interface Science, 2009. **14**(4): p. 226-235.

114. Karthick, K., et al., *Impact of thermal interface materials for thermoelectric generator systems.* Journal of Electronic Materials, 2018. **47**: p. 5763-5772.

115. Chu, J., et al., *Electrode interface optimization advances conversion efficiency and stability of thermoelectric devices.* Nature communications, 2020. **11**(1): p. 2723.

116. Le, W., et al., *Research progress of interfacial design between thermoelectric materials and electrode materials.* ACS Applied Materials & Interfaces, 2023. **15**(10): p. 12611-12621.

117. Lim, S.-S., et al., *Enhanced thermal stability of Bi2Te3-based alloys via interface engineering with atomic layer deposition.* Journal of the European Ceramic Society, 2020. **40**(10): p. 3592-3599.

118. Park, S.H., et al., *Oxidation and sublimation suppression of PbTe thermoelectric legs by plasma coated ceramic layers.* Journal of Vacuum Science & Technology A, 2016. **34**(6).

119. Lu, X., et al., *Recent advances in interface engineering of thermoelectric nanomaterials.* Materials Chemistry Frontiers, 2023.

120. Yan, Q. and M.G. Kanatzidis, *High-performance thermoelectrics and challenges for practical devices.* Nature materials, 2022. **21**(5): p. 503-513.

121. Martín-Gómez, C., et al., *Integration development of a Ventilated Active Thermoelectric Envelope (VATE): Constructive optimization and thermal performance.* Energy and Buildings, 2021. **231**: p. 110593.

122. Binggeli, C., *Building systems for interior designers*. 2003: John Wiley & Sons.

123. Narducci, D., *Do we really need high thermoelectric figures of merit? A critical appraisal to the power conversion efficiency of thermoelectric materials.* Applied physics letters, 2011. **99**(10).

124. Wolf, M., R. Hinterding, and A. Feldhoff, *High power factor vs. high zT—A review of thermoelectric materials for high-temperature application.* Entropy, 2019. **21**(11): p. 1058.

125. Zhou, C.-D., et al., *Phonon engineering significantly reducing thermal conductivity of thermoelectric materials: a review.* Rare Metals, 2023. **42**(9): p. 2825-2839.

126. Quan, Y., S. Yue, and B. Liao, *Impact of electron-phonon interaction on thermal transport: A review.* Nanoscale and Microscale Thermophysical Engineering, 2021. **25**(2): p. 73-90.

127. Kim, K., et al., *Band engineering and tuning thermoelectric transport properties of p-type Bi0. 52Sb1. 48Te3 by Pb doping for low-temperature power generation.* Scripta Materialia, 2018. **145**: p. 41-44.

128. Zhu, B., et al., *Point defect engineering: Co-doping synergy realizing superior performance in n-Type Bi2Te3 thermoelectric materials.* Small, 2021. **17**(29): p. 2101328.

129. Rani, K., et al., *Improved thermoelectric performance of Se-doped n-type nanostructured Bi2Te3.* Journal of Materials Science: Materials in Electronics, 2023. **34**(13): p. 1074.

130. Wu, H.-J. and W.-T. Yen, *High thermoelectric performance in Cu-doped Bi2Te3 with carrier-type transition.* Acta Materialia, 2018. **157**: p. 33-41.

131. Singh, N.K., et al., *Charge carriers modulation and thermoelectric performance of intrinsically p-type Bi2Te3 by Ge doping.* Journal of Alloys and Compounds, 2018. **746**: p. 350-355.

132. Parashchuk, T., et al., *Ultralow Lattice Thermal Conductivity and Improved Thermoelectric Performance in Cl-Doped Bi2Te3–x Se x Alloys.* ACS Applied Materials & Interfaces, 2022. **14**(29): p. 33567-33579.

133. Vaney, J.-B., et al., *Magnetism-mediated thermoelectric performance of the Cr-doped bismuth telluride tetradymite.* Materials today physics, 2019. **9**: p. 100090.

134. Shen, J., et al., *Enhancing thermoelectric performance of FeNbSb half-Heusler compound by Hf-Ti dual-doping.* Energy Storage Materials, 2018. **10**: p. 69-74.

135. Qiu, P., et al., *Enhanced thermoelectric performance by the combination of alloying and doping in TiCoSb-based half-Heusler compounds.* Journal of Applied Physics, 2009. **106**(10).

136. Huang, L., et al., *The effect of Sn doping on thermoelectric performance of n-type half-Heusler NbCoSb.* Physical Chemistry Chemical Physics, 2017. **19**(37): p. 25683-25690.

137. Shen, J., et al., *Enhanced thermoelectric performance in the n-type NbFeSb half-Heusler compound with heavy element Ir doping.* Materials Today Physics, 2019. **8**: p. 62-70.

138. Wu, T., et al., *Thermoelectric properties of p-type Fe-doped TiCoSb half-Heusler compounds.* Journal of Applied Physics, 2007. **102**(10).

139. Qin, D., et al., *Efficient Si doping promoting thermoelectric performance of Yb-filled CoSb3-based skutterudites.* ACS Applied Materials & Interfaces, 2022. **14**(27): p. 30901-30906.

140. Liang, T., et al., *Ultra-fast synthesis and thermoelectric properties of Te doped skutterudites.* Journal of Materials Chemistry A, 2014. **2**(42): p. 17914-17918.

141. Qiu, P., et al., *Thermoelectric properties of Ni-doped CeFe4Sb12 skutterudites.* Journal of Applied Physics, 2012. **111**(2).

142. Duan, B., et al., *Enhanced thermoelectric performance in sulfur-doped Co4Sb11. 9− xTexS0. 1 skutterudites.* Materials Letters, 2012. **79**: p. 69-71.

143. Ioannou, M., et al., *Effect of Bi-doping and Mg-excess on the thermoelectric properties of Mg2Si materials.* Journal of Physics and Chemistry of Solids, 2014. **75**(8): p. 984-991.

144. Johnson, D.D. and A. Alam, *Enhanced thermoelectric performance of Mg 2 Si 1− x Sn x codoped with Bi and Cr.* Physical Review B, 2018. **98**(11): p. 115204.

145. Tani, J.-i. and H. Kido, *Thermoelectric properties of Al-doped Mg2Si1− xSnx (x≦0.1).* Journal of Alloys and Compounds, 2008. **466**(1-2): p. 335-340.

146. Safavi, M., et al., *Thermoelectric performance of Ge-doped Mg2Si0. 35Sn0. 65 thin films.* Journal of Materials Engineering and Performance, 2021. **30**(6): p. 4045-4052.

147. Liu, W., et al., *Thermoelectric properties of Sb-doped Mg 2 Si 0.3 Sn 0.7.* Journal of electronic materials, 2011. **40**: p. 1062-1066.

148. Liu, W., Z. Ren, and G. Chen, *Nanostructured thermoelectric materials*, in *Thermoelectric Nanomaterials: Materials Design and Applications*. 2013, Springer. p. 255-285.

149. Li, J.-F., et al., *High-performance nanostructured thermoelectric materials.* NPG Asia Materials, 2010. **2**(4): p. 152-158.

150. Cramer, C.L., H. Wang, and K. Ma, *Performance of functionally graded thermoelectric materials and devices: A review.* Journal of electronic materials, 2018. **47**: p. 5122-5132.

151. Ravi, V., et al., *Thermal expansion studies of selected high-temperature thermoelectric materials.* Journal of electronic materials, 2009. **38**: p. 1433-1442.

152. Petrova, L., et al., *Chromium as an antidiffusion interlayer in higher manganese silicide-nickel contacts.* Technical Physics, 2000. **45**: p. 641-643.

153. Black, D., et al., *Power generation from nanostructured half-Heusler thermoelectrics for efficient and robust energy harvesting.* ACS Applied Energy Materials, 2018. **1**(11): p. 5986-5992.

154. Zhao, J., et al., *Impacts of thermal and electric contact resistance on the material design in segmented thermoelectric generators.* Energy Storage and Saving, 2024. **3**(1): p. 5-15.

155. Ngan, P.H., et al., *On the challenges of reducing contact resistances in thermoelectric generators based on half-Heusler alloys.* Journal of Electronic Materials, 2016. **45**: p. 594-601.

156. Tan, M., et al., *Minimization of the electrical contact resistance in thin-film thermoelectric device.* Applied Physics Reviews, 2023. **10**(2).

157. Chen, L., et al., *Ni barrier in Bi2Te3-based thermoelectric modules for reduced contact resistance and enhanced power generation properties.* Journal of Alloys and Compounds, 2019. **796**: p. 314-320.

158. Camut, J., et al., *Overcoming asymmetric contact resistances in al-contacted Mg2 (Si, sn) thermoelectric legs.* Materials, 2021. **14**(22): p. 6774.

159. Ebling, D., et al., *Module geometry and contact resistance of thermoelectric generators analyzed by multiphysics simulation.* Journal of electronic materials, 2010. **39**: p. 1376-1380.

160. Zhang, A., et al., *Influence of leg geometry configuration and contact resistance on the performance of annular thermoelectric generators.* Energy conversion and management, 2018. **166**: p. 337-342.

161. D'Isanto, F., et al., *Oxidation protective glass coating for magnesium silicide based thermoelectrics.* Ceramics International, 2020. **46**(15): p. 24312-24317.

162. Ning, H., et al., *Oxidation protective glass–ceramic coating for higher manganese silicide thermoelectrics.* Journal of Materials Science, 2016. **51**: p. 9484-9489.

163. Zawadzka, K., et al., *Enhancement of oxidation resistance of CoSb3 thermoelectric material by glass coating.* Materials & Design, 2017. **119**: p. 65-75.

164. Zhao, D., et al., *Protective properties of magnetron-sputtered Ti coating on CoSb3 thermoelectric material.* Applied surface science, 2014. **305**: p. 86-92.

165. Park, S.H., Y. Kim, and C.-Y. Yoo, *Oxidation suppression characteristics of the YSZ coating on Mg2Si thermoelectric legs.* Ceramics International, 2016. **42**(8): p. 10279-10288.

166. Bao, X., et al., *Protective properties of electrochemically deposited Al-based coatings on Yb 0.3 Co 4 Sb 12 skutterudite.* Journal of Electronic Materials, 2019. **48**: p. 5523-5531.

167. Gucci, F., et al., *Oxidation protective hybrid coating for thermoelectric materials.* Materials, 2019. **12**(4): p. 573.

168. Weidinger, H. *Raman Spectroscopy Study of the Tetragonal-to-Monoclinic Transition in Zirconium Oxide Scales and Determination of Overall Oxygen Diffusion by Nuclear Microanalysis of O18*. in *Zirconium in the Nuclear Industry: Proceedings of the... International Conference*. 1991.

169. Gurtaran, M., et al., *High-Temperature Oxidation Behaviour of CrSi Coatings on 316 Austenitic Stainless Steel.* Materials, 2023. **16**(9): p. 3533.

170. Mukherjee, M., A. Srivastava, and A.K. Singh, *Recent advances in designing thermoelectric materials.* Journal of Materials Chemistry C, 2022. **10**(35): p. 12524-12555.

171. Wei, J., et al., *Review of current high-ZT thermoelectric materials.* Journal of Materials Science, 2020. **55**: p. 12642-12704.

172. Jiang, B., et al., *High figure-of-merit and power generation in high-entropy GeTe-based thermoelectrics.* Science, 2022. **377**(6602): p. 208-213.

173. Meroz, O., N. Elkabets, and Y. Gelbstein, *Enhanced thermoelectric properties of n-type Bi2Te3–x Se x alloys following melt-spinning.* ACS Applied Energy Materials, 2019. **3**(3): p. 2090-2095.

174. Komisarchik, G., Y. Gelbstein, and D. Fuks, *Solubility of Ti in thermoelectric PbTe compound.* Intermetallics, 2017. **89**: p. 16-21.

175. Kaller, M., D. Fuks, and Y. Gelbstein, *Sc solubility in p-type half-Heusler (Ti1-cScc) NiSn thermoelectric alloys.* Journal of Alloys and Compounds, 2017. **729**: p. 446-452.

176. Bano, S., et al., *Room temperature Bi2Te3-based thermoelectric materials with high performance.* Journal of Materials Science: Materials in Electronics, 2020. **31**(11): p. 8607-8617.

177. Cao, T., et al., *Advances in bismuth-telluride-based thermoelectric devices: progress and challenges.* eScience, 2023: p. 100122.

178. Shtern, Y., et al., *Challenges and perspective recent trends of enhancing the efficiency of thermoelectric materials on the basis of PbTe.* Materials Today Communications, 2023: p. 107083.

179. Zhou, Y. *Progress and trend of PbTe based Thermoelectric Materials*. in *Journal of Physics: Conference Series*. 2022. IOP Publishing.

180. Chauhan, N.S., et al., *Enhanced thermoelectric performance in Hf-Free p-type (Ti, Zr) CoSb half-heusler alloys.* Journal of Electronic Materials, 2019. **48**: p. 6700-6709.

181. Van Du, N., et al., *Enhanced thermoelectric properties of Hf-free half-Heusler compounds prepared via highly fast process.* Journal of Alloys and Compounds, 2021. **886**: p. 161293.

182. Sun, Q., et al., *Structural Evolution of High-Performance Mn-Alloyed Thermoelectric Materials: A Case Study of SnTe.* Small, 2021. **17**(25): p. 2100525.

183. Tian, B.-Z., et al., *Enhanced thermoelectric performance of SnTe-based materials via interface engineering.* ACS Applied Materials & Interfaces, 2021. **13**(42): p. 50057-50064.

184. Moshwan, R., et al., *Eco-friendly SnTe thermoelectric materials: progress and future challenges.* Advanced Functional Materials, 2017. **27**(43): p. 1703278.

185. Zhou, Z., et al., *High-performance magnesium-based thermoelectric materials: Progress and challenges.* Journal of Magnesium and Alloys, 2022.

186. Nieroda, P., et al., *The structural, microstructural and thermoelectric properties of Mg2Si synthesized by SPS method under excess Mg content conditions.* Journal of Alloys and Compounds, 2019. **775**: p. 138-149.

187. Ioannou, I.A., *P-type half-Heusler and Bismuth-Telluride thermoelectric materials.* 2022.

188. Ioannou, I., et al., *Reduction of Hf via Hf/Zr Substitution in Mechanically Alloyed (Hf, Ti) CoSb Half-Heusler Solid Solutions.* Inorganics, 2022. **10**(4): p. 51.

189. Zhang, X., et al., *Ultralow lattice thermal conductivity and improved thermoelectric performance in a Hf-free half-Heusler compound modulated by entropy engineering.* Journal of Materials Chemistry A, 2023. **11**(15): p. 8150-8161.

190. Zhang, Q., et al., *Enhanced thermoelectric performance of Hafnium free n-type ZrNiSn half-Heusler alloys by isoelectronic Si substitution.* Materials Today Physics, 2022. **24**: p. 100648.

191. Min, R., et al., *Significantly improved thermoelectric properties of Nb-doped ZrNiSn half-Heusler compounds.* Chemical Engineering Journal, 2022. **449**: p. 137898.

192. Barako, M.T., et al., *Thermal Cycling, Mechanical Degradation, and the Effective Figure of Merit of a Thermoelectric Module.* Journal of Electronic Materials, 2013. **42**(3): p. 372-381.

193. Kang, H.B., et al., *Understanding oxidation resistance of half-Heusler alloys for in-air high temperature sustainable thermoelectric generators.* ACS applied materials & interfaces, 2020. **12**(32): p. 36706-36714.

194. Yamini, S.A., et al., *Fabrication of thermoelectric materials–thermal stability and repeatability of achieved efficiencies.* Journal of Materials Chemistry C, 2015. **3**(40): p. 10610-10615.

195. Skomedal, G., et al., *Methods for enhancing the thermal durability of high-temperature thermoelectric materials.* Journal of electronic materials, 2014. **43**: p. 1946-1951.

196. Sootsman, J.R., D.Y. Chung, and M.G. Kanatzidis, *New and old concepts in thermoelectric materials.* Angewandte Chemie International Edition, 2009. **48**(46): p. 8616-8639.

197. Zheng, Y., et al., *Defect engineering in thermoelectric materials: what have we learned?* Chemical Society Reviews, 2021. **50**(16): p. 9022-9054.

198. Kikuchi, D., J. Tadokoro, and T. Eguchi, *The High-Temperature Thermoelectric Properties of Polycrystalline Ba 8 Ga x Al y Si 46− x− y Type-I Clathrates.* Journal of electronic materials, 2014. **43**: p. 2141-2144.

199. Weast, R.C., *Handbook of Chemistry and Physics: 1st Student Edition.* CRC-Press, Boca Raton, Florida, 1988. **69**.

200. Appel, O., et al., *Surface oxidation of TiNiSn (Half-Heusler) alloy by oxygen and water vapor.* Materials, 2018. **11**(11): p. 2296.

201. Berche, A. and P. Jund, *Oxidation of half-Heusler NiTiSn materials: Implications for thermoelectric applications.* Intermetallics, 2018. **92**: p. 62-71.

202. Qiu, P., et al., *"Pesting"-like oxidation phenomenon of p-type filled skutterudite Ce0. 9Fe3CoSb12.* Journal of alloys and compounds, 2014. **612**: p. 365-371.

203. Patil, R. and E. Subbarao, *Axial thermal expansion of ZrO2 and HfO2 in the range room temperature to 1400° C.* Journal of Applied Crystallography, 1969. **2**(6): p. 281-288.

204. Spencer, J.A., et al., *A review of band structure and material properties of transparent conducting and semiconducting oxides: Ga2O3, Al2O3, In2O3, ZnO, SnO2, CdO, NiO, CuO, and Sc2O3.* Applied Physics Reviews, 2022. **9**(1).

205. Ohno, H. and Y. Kanzawa, *Internal oxidation in gold alloys containing small amounts of Fe and Sn.* Journal of Materials Science, 1983. **18**: p. 919-929.

206. Wiberg, E. and N. Wiberg, *Inorganic chemistry*. 2001: Academic press.

207. Alwash, N.A., et al., *Fire retardancy characteristics of polymeric composite materials.* Baghdad Science Journal, 2013. **10**(3عدد خاص بموتمر الكيمياء).

208. Finn, P.A., et al., *Thermoelectric materials: Current status and future challenges*. 2021, Frontiers Media SA. p. 677845.

209. Gayner, C. and K.K. Kar, *Recent advances in thermoelectric materials.* Progress in Materials Science, 2016. **83**: p. 330-382.

210. Wang, H., et al., *Determination of thermoelectric module efficiency: A survey.* Journal of electronic materials, 2014. **43**: p. 2274-2286.

211. Lv, S., et al., *A comprehensive review of strategies and approaches for enhancing the performance of thermoelectric module.* Energies, 2020. **13**(12): p. 3142.

212. Ben-Ayoun, D., Y. Sadia, and Y. Gelbstein, *High temperature thermoelectric properties evolution of Pb1-xSnxTe based alloys.* Journal of Alloys and Compounds, 2017. **722**: p. 33-38.

213. Fu, C., et al., *Realizing high figure of merit in heavy-band p-type half-Heusler thermoelectric materials.* Nature communications, 2015. **6**(1): p. 8144.

214. Poon, S.J., *Half Heusler compounds: promising materials for mid-to-high temperature thermoelectric conversion.* Journal of Physics D: Applied Physics, 2019. **52**(49): p. 493001.

215. Downie, R.A., et al., *Metal distributions, efficient n-type doping, and evidence for in-gap states in TiNiM y Sn (M= Co, Ni, Cu) half-Heusler nanocomposites.* Chemistry of Materials, 2015. **27**(7): p. 2449-2459.

216. Balasubramanian, P., M. Battabyal, and R. Gopalan, *Improving the oxidation resistance of thermoelectric Mg2Si leg with silica coating.* Materials Letters, 2022. **312**: p. 131599.

217. Dong, H., et al., *Improved oxidation resistance of thermoelectric skutterudites coated with composite glass.* Ceramics International, 2013. **39**(4): p. 4551-4557.

218. Zawadzka, K.M., et al., *Processing, Characterization, and Oxidation Resistance of Glass-Ceramic Coating on CoSb3.* Crystals, 2023. **13**(6): p. 880.

219. Brostow, W., I.K. Chen, and J.B. White, *Effects of polymeric coatings on the service life of bismuth telluride-based thermoelectric materials.* Sustainable Energy & Fuels, 2017. **1**(6): p. 1376-1380.

220. Kashkarov, E., et al., *Oxidation kinetics of Cr-coated zirconium alloy: Effect of coating thickness and microstructure.* Corrosion Science, 2020. **175**: p. 108883.

221. Michau, A., et al., *High-temperature oxidation resistance of chromium-based coatings deposited by DLI-MOCVD for enhanced protection of the inner surface of long tubes.* Surface and Coatings Technology, 2018. **349**: p. 1048-1057.

222. Schütze, M., D.R. Holmes, and R.B. Waterhouse, *Protective oxide scales and their breakdown.* (No Title), 1997.

223. Bamba, G., et al., *Thermal oxidation kinetics and oxide scale adhesion of Fe–15Cr alloys as a function of their silicon content.* Acta Materialia, 2006. **54**(15): p. 3917-3922.

224. Soleimani-Dorcheh, A. and M. Galetz, *Oxidation and nitridation behavior of Cr–Si alloys in air at 1473 K.* Oxidation of Metals, 2015. **84**: p. 73-90.

225. He, X., et al., *Effect of Si content of CrSi-based coatings on their oxidation resistance in high temperature air.* Ceramics International, 2020. **46**(8): p. 11357-11363.

226. Godlewska, E., et al., *Protective properties of magnetron-sputtered Cr–Si layers on CoSb3.* Oxidation of metals, 2010. **74**(3): p. 205-213.

227. Gurtaran, M., et al., *Cyclic Oxidation Behaviour of N-type (Zr, Ti) Ni (Sn, Sb) and P-type (Zr, Ti) Co (Sn, Sb) Thermoelectric Materials.* Journal of Materials Research and Technology, 2024.

228. Yang, C., et al., *Effects of thermal expansion coefficient mismatch on structure and electrical properties of TiO 2 film deposited on Si substrate.* Surface Review and Letters, 2008. **15**(04): p. 487-491.

229. Khanna, A.S., *Introduction to high temperature oxidation and corrosion*. 2002: ASM international.

230. Yeom, H., et al., *High temperature oxidation and microstructural evolution of cold spray chromium coatings on Zircaloy-4 in steam environments.* Journal of Nuclear Materials, 2019. **526**: p. 151737.

231. Tada, H., et al., *Thermal expansion coefficient of polycrystalline silicon and silicon dioxide thin films at high temperatures.* Journal of applied physics, 2000. **87**(9): p. 4189-4193.

232. Ganechari, S. and S. Kate, *Alternative energy sources.* Alternative Energy Sources, 2005. **5**.

233. Liu, W., et al., *New trends, strategies and opportunities in thermoelectric materials: a perspective.* Materials Today Physics, 2017. **1**: p. 50-60.

234. Snyder, G.J. and A.H. Snyder, *Figure of merit ZT of a thermoelectric device defined from materials properties.* Energy & Environmental Science, 2017. **10**(11): p. 2280-2283.

235. Yu, J., et al., *Half-Heusler thermoelectric module with high conversion efficiency and high power density.* Advanced Energy Materials, 2020. **10**(25): p. 2000888.

236. Schierning, G., et al., *Concepts for medium-high to high temperature thermoelectric heat-to-electricity conversion: a review of selected materials and basic considerations of module design.* Translational Materials Research, 2015. **2**(2): p. 025001.

237. Sun, W., et al., *Thermoelectric module design to improve lifetime and output power density.* Materials Today Physics, 2021. **18**: p. 100391.

238. Shtern, Y., et al., *Technology and investigation of ohmic contacts to thermoelectric materials.* Acta physica polonica A, 2016. **129**(4): p. 785-787.

239. Korchagin, E., et al., *Contacts to thermoelectric materials obtained by chemical and electrochemical deposition of Ni and Co.* Journal of Electronic Materials, 2022. **51**(10): p. 5744-5758.

240. Korchagin, E., et al., *Formation and Properties of Nickel Contacts to Thermoelectric Materials Based on Bismuth and Antimony Chalcogenides.* Russian Journal of Applied Chemistry, 2022. **95**(4): p. 536-543.

241. Ayachi, S., et al., *Developing Contacting Solutions for Mg2Si1–x Sn x-Based Thermoelectric Generators: Cu and Ni45Cu55 as Potential Contacting Electrodes.* ACS Applied Materials & Interfaces, 2019. **11**(43): p. 40769-40780.

242. Zhang, H., et al., *Improved contact performance and thermal stability of Co–Ni alloy barrier layer for bismuth telluride-based thermoelectric devices.* Journal of Materials Science: Materials in Electronics, 2024. **35**(10): p. 727.

243. Hosseini Khorasani, S.A. and S. Sanjabi, *High corrosion resistance Ni-reduced graphene oxide nanocomposite coating.* Corrosion Reviews, 2016. **34**(5-6): p. 305-312.

244. Jaldurgam, F.F., Z. Ahmad, and F. Touati *Synthesis and Performance of Large-Scale Cost-Effective Environment-Friendly Nanostructured Thermoelectric Materials*. Nanomaterials, 2021. **11**, 1091 DOI: 10.3390/nano11051091.

245. Liu, W., et al., *Current progress and future challenges in thermoelectric power generation: From materials to devices.* Acta Materialia, 2015. **87**: p. 357-376.

246. Ajiboye, T.O. and D.C. Onwudiwe, *Bismuth sulfide based compounds: Properties, synthesis and applications.* Results in Chemistry, 2021. **3**: p. 100151.

247. Yang, Z.-R., et al., *Type controlled thermoelectric properties in tin selenide fabricated using room-temperature synthesis and hot pressing.* Journal of Alloys and Compounds, 2021. **889**: p. 161639.

248. Pham, N.H., et al., *Ni and Ag electrodes for magnesium silicide based thermoelectric generators.* Materials Today Energy, 2019. **11**: p. 97-105.

249. Chen, X., et al., *Thin Film Thermoelectric Materials: Classification, Characterization, and Potential for Wearable Applications.* Coatings, 2018. **8**(7).

250. Hamawandi, B., et al., *A Comparative Study on the Thermoelectric Properties of Bismuth Chalcogenide Alloys Synthesized through Mechanochemical Alloying and Microwave-Assisted Solution Synthesis Routes.* Frontiers in Materials, 2020. **7**.

251. Tan, M., Y. Deng, and Y. Hao, *Improved thermoelectric performance of a film device induced by densely columnar Cu electrode.* Energy, 2014. **70**: p. 143-148.

252. Peranio, N., et al., *Room-temperature MBE deposition, thermoelectric properties, and advanced structural characterization of binary Bi2Te3 and Sb2Te3 thin films.* Journal of Alloys and Compounds, 2012. **521**: p. 163-173.

253. You, H., et al., *Growth and thermoelectric properties of Bi2Te3 films deposited by modified MOCVD.* Journal of Crystal Growth, 2012. **346**(1): p. 17-21.

254. Amiri, L., et al., *Spectroscopic study and thermoelectric properties of copper sulfide thin films prepared by the flash evaporation method.* Journal of Alloys and Compounds, 2022. **924**: p. 166479.

255. Khumtong, T., et al., *Microstructure and electrical properties of antimony telluride thin films deposited by RF magnetron sputtering on flexible substrate using different sputtering pressures.* Journal of Electronic Materials, 2017. **46**(5): p. 3166-3171.

256. Shen, S., et al., *Enhancing thermoelectric properties of Sb2Te3 flexible thin film through microstructure control and crystal preferential orientation engineering.* Applied Surface Science, 2017. **414**: p. 197-204.

257. Kim, D.-H., et al., *Effect of deposition temperature on the structural and thermoelectric properties of bismuth telluride thin films grown by co-sputtering.* Thin Solid Films, 2006. **510**(1-2): p. 148-153.

258. Kurokawa, T., et al., *Influences of substrate types and heat treatment conditions on structural and thermoelectric properties of nanocrystalline Bi2Te3 thin films formed by DC magnetron sputtering.* Vacuum, 2020. **179**: p. 109535.

259. Jitthamapirom, P., et al., *Comparison of thermoelectric properties of flexible bismuth telluride thin films deposited via DC and RF magnetron sputtering.* Ferroelectrics, 2019. **552**(1): p. 64-72.

260. Takayama, K. and M. Takashiri, *Multi-layered-stack thermoelectric generators using p-type Sb2Te3 and n-type Bi2Te3 thin films by radio-frequency magnetron sputtering.* Vacuum, 2017. **144**: p. 164-171.

261. Prainetr, N., et al., *Effect of substrates on thermoelectric properties of Ag–Sb–Te thin films within the temperature annealing.* Physica B: Condensed Matter, 2020. **582**: p. 411977.

262. Vora-ud, A., et al., *Microstructural control by substrate heating in Pulse-DC sputtering induced thermoelectric Ge2Sb2Te5 thin films.* Journal of Alloys and Compounds, 2018. **763**: p. 430-435.

263. Fan, P., et al., *Thermoelectric properties of zinc antimonide thin film deposited on flexible polyimide substrate by RF magnetron sputtering.* Journal of Materials Science: Materials in Electronics, 2014. **25**(11): p. 5060-5065.

264. Burmistrova, P.V., et al., *Thermoelectric properties of epitaxial ScN films deposited by reactive magnetron sputtering onto MgO (001) substrates.* Journal of Applied Physics, 2013. **113**(15): p. 153704.

265. Perez-Taborda, J.A., et al., *Pulsed hybrid reactive magnetron sputtering for high zT Cu2Se thermoelectric films.* Advanced Materials Technologies, 2017. **2**(7): p. 1700012.

266. Song, L., J. Zhang, and B.B. Iversen, *Enhanced thermoelectric properties of SnSe thin films grown by single-target magnetron sputtering.* Journal of Materials Chemistry A, 2019. **7**(30): p. 17981-17986.

267. Chen, Z., et al., *Effect of substrate temperature on structural and thermoelectric properties of RF magnetron sputtered SnSe thin film.* Functional Materials Letters, 2019. **12**(03): p. 1950040.

268. Tani, J.-i. and H. Ishikawa, *Thermoelectric properties of Mg2Sn thin films fabricated using radio frequency magnetron sputtering.* Thin Solid Films, 2019. **692**: p. 137601.

269. Tani, J.-i. and H. Kido, *Electrical properties of Mg2Si thin films on flexible polyimide substrates fabricated by radio-frequency magnetron sputtering.* Journal of the Ceramic Society of Japan, 2015. **123**(1436): p. 298-301.

270. Nowak, D., M. Turkiewicz, and N. Solnica, *Thermoelectric Properties of Thin Films of Germanium-Gold Alloy Obtained by Magnetron Sputtering.* Coatings, 2019. **9**(2): p. 120.

271. Song, L., J. Zhang, and B.B. Iversen, *Microstructure and Thermoelectric Properties of Zn1–x Ag x Sb Thin Films Grown by Single-Target Magnetron Sputtering.* ACS Applied Energy Materials, 2020. **3**(3): p. 2055-2062.

272. Matsuda, T., M. Uenuma, and M. Kimura, *Thermoelectric effects of amorphous Ga–Sn–O thin film.* Japanese Journal of Applied Physics, 2017. **56**(7): p. 070309.

273. Schaeuble, N., et al., *Aluminium-Substituted Zinc Oxide Thin Films: Thermoelectric Properties and Structural Characterisation.*

274. Fan, P., et al., *Thermoelectric properties of cobalt antimony thin films deposited on flexible substrates by radio frequency magnetron sputtering.* Journal of Electronic Materials, 2015. **44**(2): p. 630-635.

275. Chen, R., et al., *Thermoelectrics of Nanowires.* Chem Rev, 2019. **119**(15): p. 9260-9302.

276. He, Z., et al., *Enhancement of thermoelectric performance of N-type Bi2Te3 based thin films via in situ annealing during magnetron sputtering.* Ceramics International, 2020. **46**(9): p. 13365-13371.

277. Linseis, V., et al., *Advanced platform for the in-plane ZT measurement of thin films.* Review of Scientific Instruments 89, (2018); https://doi.org/10.1063/1.5005807, 2018. **89**(015110 ): p. 015110.

278. Francioso, L., et al., *Flexible thermoelectric generator for ambient assisted living wearable biometric sensors.* Journal of Power Sources, 2011. **196**(6): p. 3239-3243.

279. Kwon, S.-D., et al., *Fabrication of Bismuth Telluride-Based Alloy Thin Film Thermoelectric Devices Grown by Metal Organic Chemical Vapor Deposition.* Journal of Electronic Materials, 2009. **38**(7): p. 920-924.